

Kaj Jansson

Measurements of Neutron-induced Nuclear
Reactions for More Precise Standard Cross
Sections and Correlated Fission Properties



UPPSALA
UNIVERSITET

Dissertation presented at Uppsala University to be publicly examined in Polhemsalen, Ångströmlaboratoriet, Lägerhyddsvägen 1, Uppsala, Friday, 10 November 2017 at 09:15 for the degree of Doctor of Philosophy. The examination will be conducted in English. Faculty examiner: Fanny Farget (CNRS/IN2P3).

Abstract

Jansson, K. 2017. Measurements of Neutron-induced Nuclear Reactions for More Precise Standard Cross Sections and Correlated Fission Properties. *Uppsala Dissertations from the Faculty of Science and Technology* 131. 142 pp. Uppsala: Acta Universitatis Upsaliensis. ISBN 978-91-513-0085-6.

It is difficult to underestimate the importance of neutron cross section standards in the nuclear data field. Accurate and precise standards are prerequisites for measuring neutron cross sections. Two different projects are presented here with the aim of improving on neutron standards.

A simulation study was performed for an experiment intended to measure the cross sections of $H(n,n)$, $^{235}U(n,f)$, and $^{238}U(n,f)$ relative to each other. It gave the first estimates of the performance of the experimental setup. Its results have aided the development of the experimental setup by setting limits on the target and detector design.

A second neutron-standard project resulted in three measurements of $^6Li(n,\alpha)t$ relative to $^{235}U(n,f)$. Each subsequent measurement improved upon the previous one and changed the experimental setup accordingly. Although, preliminary cross sections were agreeing well with evaluated data files in some energy intervals, the main goal to measure the cross section up to 3 MeV was not reached.

Mass yields and energy spectra are important outcomes of many fission experiments, but in low yield regions the uncertainties are still high even for recurrently studied nuclei. In order to understand the fission dynamics, one also needs correlated fission data. One particular important property is the distribution of excitation energy between the two nascent fission fragments. It is closely connected to the prompt emission of neutrons and γ 's and reveals information about how nucleons and energy are transferred within the fissioning nucleus.

By measuring both the pre and post neutron-emission fragment masses, the cumbrance of detecting neutrons directly is overcome. This is done using the fission spectrometer VERDI and the 2E-2v method. In this work I describe how both the spectrometer, the analysis method, and the calibration procedures have been further developed. Preliminary experimental data show the great potential of VERDI, but also areas that call for more attention. A previously overlooked consequence of a central assumption was found and a correction method is proposed that can correct previously obtained data as well.

The last part of this thesis concerns the efficiencies of the fission product extraction at the IGISOL facility. The methodology of the fission yield measurements at IGISOL are reliant on assumptions that have not been systematically investigated. The presented work is a first step of such an investigation that can also be used as a tool for optimising the setup for measurements of exotic nuclei. A simulation framework connecting three different simulation codes was developed to investigate the produced yield of fission products in a buffer gas. Several different variants of the setup were simulated and the findings were generally accordant with previous estimates. A reasonable agreement between experimental data and the simulation results is demonstrated.

Keywords: Cross Section, Fission, Neutron-induced reactions, Simulation, VERDI

Kaj Jansson, Department of Physics and Astronomy, Applied Nuclear Physics, Box 516, Uppsala University, SE-751 20 Uppsala, Sweden.

© Kaj Jansson 2017

ISSN 1104-2516

ISBN 978-91-513-0085-6

urn:nbn:se:uu:diva-329953 (<http://urn.kb.se/resolve?urn=urn:nbn:se:uu:diva-329953>)

Contents

1	Introduction	1
1.1	Thesis outline	2
1.2	Reuse of previous work	2
2	Neutron-induced nuclear reactions	3
2.1	Neutron standard cross sections	3
2.1.1	Relative measurements	5
2.2	Nuclear structure	5
2.3	Compound reactions	6
2.4	Fission	8
3	Particle detectors	15
3.1	Frisch-gridded ionisation chambers	16
3.1.1	Obtaining angular information	16
3.1.2	Loss of charge and choice of gas	20
3.2	Parallel plate avalanche counters	21
3.3	Multi-channel plates	22
3.4	Silicon detectors	23
3.4.1	Radiation damage	24
3.4.2	Detecting heavy ions in silicon detectors	25
4	Neutron facilities	27
4.1	NFS	27
4.2	GELINA	28
4.3	IGISOL	28
5	Neutron standards at NFS	30
5.1	Motivation	30
5.2	Experimental setup	32
5.2.1	Detector telescopes	34
5.2.2	Stacked target	35
5.2.3	Neutron energy	35
5.2.4	Particle identification	36
5.2.5	Observables	36
5.3	Simulations	37
5.3.1	Simulation setup	38
5.3.2	Simulation results	38
5.4	Current status	42

6	Alpha-particle and triton production at GELINA	43
6.1	Motivation	43
6.2	First experiment	45
6.2.1	Experimental setup	45
6.2.2	Analysis procedure	46
6.2.3	Results	54
6.3	Second experiment	58
6.3.1	Changes compared to the original experiment	58
6.3.2	Results	59
6.4	Third experiment	60
6.4.1	Changes compared to the second experiment	60
6.4.2	Results	63
6.5	Improvements for a next experiment	66
6.5.1	DAQ	66
6.5.2	γ -flash	66
6.5.3	The lithium chamber	67
7	Correlated fission observables with VERDI	68
7.1	Motivation	68
7.2	Notation	69
7.3	The 2E method	69
7.4	The 2E-2v method	70
7.4.1	Isotropic neutron emission	70
7.4.2	Pre- and post-neutron masses and energies	72
7.5	Experimental setup	74
7.6	Simulation study	76
7.7	VERDI data analysis	79
7.7.1	Time-of-flight calibration	80
7.7.2	Energy calibration and PHD corrections	80
7.7.3	PDT corrections	82
7.7.4	Comparison of calibration methods	88
7.7.5	Intrinsic deficiency in the 2E-2v method	90
7.7.6	Detection efficiency	94
7.7.7	Ternary fission	98
7.8	The future and unresolved issues	98
8	Simulated ion stopping at IGISOL	101
8.1	Ion guide for proton-induced fission	102
8.1.1	Experimental setup	102
8.1.2	Simulation setup	102
8.1.3	Main results	104
8.2	Ion guide for neutron-induced fission	106
8.2.1	The neutron source	108
8.2.2	The ion guide	109

8.2.3	Ion stopping simulation	111
8.2.4	Results	112
8.2.5	Conclusions	119
9	Svensk sammanfattning (Summary in Swedish)	121
10	Acknowledgements	124
Appendix A: Code developed		126
A.1	Modifications to Geant4	126
A.1.1	Extended and corrected cross sections	126
A.1.2	Biasing of discrete events in simulations	127
A.1.3	New effective charge model	129
A.2	ROOT file I/O made simple	130
A.3	Acquisition software for a SPdevices digitiser	131
Appendix B: Selected publications		133
	References	136

List of Figures

2.1	Prompt radiation.	9
2.2	FF excitation energy as a function of mass.	10
2.3	Schematic fission barrier.	12
2.4	TKE as a function of mass.	14
3.1	GIC electrodes.	17
3.2	GIC signals.	17
3.3	Prototype PPACs developed in our lab.	22
3.4	Detector telescope.	24
5.1	Fission cross section discrepancies.	31
5.2	The Medley setup.	33
5.3	Medley target area.	33
5.4	Simulated ΔE - ΔE plot.	37
5.5	Contributions to the neutron energy resolution.	39
5.6	Expected uncertainty in the incoming neutron energy.	40
5.7	Fraction of FPs below a certain energy threshold.	41
6.1	Resonance structure of the ${}^6\text{Li}(n,\alpha)t$ reaction.	44
6.2	Schematic of the original ionisation chamber.	46
6.3	Anode and grid signals from an α -event.	47
6.4	Correction of time walk.	49
6.5	Grid-anode plot of fission events.	50
6.6	Energy loss correction for fission events.	51
6.7	Grid-anode plot of α -particle events.	53
6.8	Cosine distributions of fission events.	55
6.9	Energy spectra for fission events.	55
6.10	α -particle events transformed into the CoM frame.	57
6.11	Deduced cross section from the first experimental run.	57
6.12	Test of 95% Ar+5% CO_2 gas mixture.	58
6.13	Schematic of the split ionisation chamber.	61
6.14	Fitted signals.	63
6.15	Improvements in the cosine distributions.	64
6.16	Grid-anode plot for α -particle and triton events.	64
6.17	Deduced cross section from the third experimental run.	65
7.1	Effects of mass and relativism.	73
7.2	The VERDI setup.	74
7.3	Photo of one of the MCPs.	75
7.4	Electronic scheme of the VERDI setup.	77
7.5	Coincidence rate estimation due to broken collinearity.	79

7.6	Different choices of energy calibrations.	82
7.7	One dimensional distributions when the Velkovska method was used.	84
7.8	The Velkovska method fails.	84
7.9	New method to parametrise the PDT.	85
7.10	One dimensional distributions when the new PDT correction was used.	86
7.11	Testing the new PDT correction method on synthetic data. . . .	87
7.12	The experimental neutron multiplicity for different analysis choices.	89
7.13	Total neutron multiplicity as a function of TKE.	89
7.14	Experimentally derived PDTs.	90
7.15	Neutron multiplicity derived from synthetic data.	91
7.16	Masswise correlation between M^{pre} and $\bar{\nu}$	92
7.17	Standard deviations of the mass broadening.	94
7.18	The corrected $\bar{\nu}(M^{\text{pre}})$ from $^{252}\text{Cf}(sf)$	95
7.19	The corrected $\bar{\nu}(M^{\text{pre}})$ from $^{235}\text{U}(n_{\text{th}},f)$	95
7.20	TKE dependent detection efficiency.	96
7.21	The effect of detection efficiency.	97
7.22	Neutron multiplicity dependence on detection efficiency. . . .	98
7.23	Ternary particles detected by VERDI.	99
8.1	Neutron- and proton-induced fission yields.	102
8.2	Setup used for the proton-induced experiment.	103
8.3	Chosen FP energies.	104
8.4	Ion stopping efficiency as a function of mass.	105
8.5	Ion stopping efficiency as a function of kinetic energy.	105
8.6	Map of where the simulated ions stops.	106
8.7	Dependence on target thickness.	107
8.8	Dependence on nickel foil thickness.	107
8.9	The neutron flux on top of a schematic of the ion guide. . . .	108
8.10	3D rendering of the simulated geometry.	110
8.11	Cross sectional schematics of the target placements.	110
8.12	The average neutron flux, the fission cross section, and the average fission rate.	112
8.13	Mass yields of stopped ions from simulation Sim I	114
8.14	Charge yields of stopped ions from simulation Sim I	114
8.15	Effects of effective charge model and increased pressure. . . .	115
8.16	Yield of the ions stopped in the gas from Sim I	117
8.17	Yield of the ions stopped in the gas from Sim VI	117
8.18	Positions of the ions stopped in the gas from Sim VII	118
8.19	Cumulative distribution of the how far the stopped ions travelled.	119
A.1	Correction of the elastic neutron scattering cross section. . . .	127

List of Tables

2.1	The IAEA neutron standards.	4
2.2	The first six magic numbers.	7
3.1	GIC notation.	18
6.1	Measured ratios compared to values derived from the target characterisation.	54
7.1	Particle data for fitting the schmitt function.	80
8.1	Yields of the produced and stopped ions for the different simu- lations.	113

List of Abbreviations

ADC	Analogue to Digital Converter
CoM	Centre-of-Momentum (frame of reference)
CFD	Constant Fraction Discriminator
DAQ	Data AcQuisition
GIC	Gridded Ionisation Chamber
FF	Fission Fragment (before prompt neutron emission)
FFAD	Fission Fragment Angular Distribution
FP	Fission Product (after prompt neutron emission)
FR	Fission rate
FWHM	Full Width at Half Maximum
ISOL	Isotope Separator On Line
LCP	Light Charged Particle
LDM	Liquid Drop Model
MCP	Multi-Channel Plate (detector)
PDT	Plasma Delay Time
PH	Pulse Height
PHD	Pulse Height Deficiency
PIPS	Passivated Implanted Planar Silicon (detector)
PL	Particle Leaking (see section 6.1)
PPAC	Parallel Plate Avalanche Counter
PM	Photo-Multiplier (tube)
QMN	Quasi-Mono-energetic Neutron
SSB	Silicon Surface Barrier (detector)
TAC	Time to Analogue Converter
TKE	Total Kinetic Energy
ToF	Time-of-Flight
TWC	Tag Word Coder
TXE	Total Excitation Energy

1. Introduction

*Nu ska vi ge oss av, sa lilla björnen
till sin vän.
Nu ska vi ut i världen för att söka
sanningen!*

— Charta 77

The phenomena of nuclear fission has been known since 1939 when the experimental results from the year before [1] was theoretically explained by Lise Meitner and Otto Frisch [2]. Quickly, it was realised that this was a tremendous source of power and soon it was utilised for devastating new weapons. But, more importantly, fission used in a controlled and stable fashion made nuclear power plants possible.

Nuclear power plants have been in use since the fifties, but are more relevant than ever today. In order to reduce the impact of global warming the United Nation instituted *Intergovernmental Panel on Climate Change* (IPCC), calls for energy production methods emitting less carbon dioxide. Nuclear power is an obvious choice since its low carbon dioxide footprint is in the same order of magnitude as wind and solar power [3]. An expansion of nuclear power therefore encouraged by the IPCC [4].

Despite the long history of nuclear power, there are many things still not known about fission and the underlying interactions. The main reason is the complexity of the strong force that governs all nuclear reactions. The strong force keeps the quarks together to form nucleons, but the residual strong force also keeps the nucleons together to form nuclei. It dominates the inter-nucleon interactions, since it is much stronger than the well known electromagnetic force at this range. The residual force is short ranged, in the order of fm, but affects all nucleons, whether they are neutrons or protons almost identically. Thus, modelling a large nucleus is a many-body problem, and as such, it is difficult to handle in great detail. Of that reason, a mean-field theory is commonly used as an approximation, thereby treating the nucleon-nucleon interactions as perturbations.

Since accurate models for arbitrary nuclei are non-existent, there are lots of nuclei and properties that must be measured. Masses, half-lives, nuclear structure, etc. are all important parameters to understand not only nuclei themselves, but also how they were created on a grand scale. Without a detailed model of fission, decays, and many other nuclear phenomena, the nucleosynthesis occurring in stars and big cosmological events cannot be understood.

Nuclear physics and nuclear data are therefore not only important for applications like nuclear power and carbon dating. It is also highly relevant for understanding the strong force, cosmological events, as well as the abundance and origin of every element in the universe. The work presented in this thesis is a modest attempt to add to our knowledge about nuclear reactions, by improving on previous data as well as working towards measuring new observables and systems.

1.1 Thesis outline

This thesis consists of four main projects described in chapters 5 to 8. The theoretical background, as well as the detector and nuclear facility requirements for each of the projects are overlapping, and therefore presented in the preceding chapters 2 to 4. Some more technical implementation details have been put in appendix A, while appendix B lists some of the scientific publications I have (co)authored.

1.2 Reuse of previous work

The sections related to the simulations of the NFS experiments are reworked and extended content from my licentiate thesis [5]. Regarding the ${}^6\text{Li}(n,\alpha)t$ measurement parts (mainly sections 3.1, 4.2, 6.1 and 6.2) are based on the licentiate thesis, but also in this case the previous content has been reworked and extended.

2. Neutron-induced nuclear reactions

***Protip:** You can safely ignore any sentence that includes the phrase “According to quantum mechanics”.*

— Randall Munroe

This chapter provides a short theoretical background of the nuclear reactions relevant for my projects. Some general terminology and concepts, that will be used in later chapters, are also introduced.

2.1 Neutron standard cross sections

In both experiments presented in chapters 5 and 6, respectively, the main ingredients are neutron standards. The importance of these standards in the field of experimental nuclear physics is great. Therefore, they deserve their own section in this thesis, in order for me to introduce them and to explain their significance to many neutron-based experiments.

Absolute cross section measurements of neutron-induced reactions are cumbersome due to the neutron’s reluctance to interact. Therefore, it is difficult to, e.g., count all of the neutrons in a neutron beam. It is also difficult to create a neutron beam with specific properties since neutrons are difficult to direct and control. Direct measurements of the neutron cross sections are possible, e.g. by utilising neutron tagging [6], but more commonly indirect measurements relative a neutron standard are made.

The neutron standards allow us to obtain cross sections for neutron-induced reactions on an absolute scale by measuring relative to another reaction with an assumed known cross section. However, if a standard is adjusted due to, e.g. better measurements, every single cross section measured relative to that particular standard must change accordingly.

Many different standards have been in use and there is not a single standard that is superior in all circumstances. So, one could ask what properties make a standard, a standard? A number of good properties for a neutron standard is listed by Carlson [7] and a summary of those is provided below.

- The nuclide should be available in elemental form, be chemically inert and not be radioactive.
- It should be easy to fabricate into different forms.

Table 2.1. *The neutron standards according to IAEA and the energy ranges in which they are considered standards [8].*

Reaction	Neutron energy range
H(n,n)	1 keV - 20 MeV
$^3\text{He}(n,p)$	thermal - 50 keV
$^6\text{Li}(n,t)$	thermal - 1 MeV
$^{10}\text{B}(n,\alpha)$	thermal - 1 MeV
$^{10}\text{B}(n,\alpha_1\gamma)$	thermal - 1 MeV
$^{\text{nat}}\text{C}(n,n)$	below 1.8 MeV
$^{197}\text{Au}(n,\gamma)$	thermal, 0.2 MeV - 2.5 MeV
$^{235}\text{U}(n,f)$	thermal, 0.15 MeV - 200 MeV
$^{238}\text{U}(n,f)$	2 MeV - 200 MeV

- It should not be expensive.
- It should have no interfering reaction channels.
- Its compound should be isotopically pure.
- The cross section should be large, with no structure over the region in which it is used.

In addition to this list there are more requirements depending on what kind of reaction the neutron standard is based on and what kind of setup is used to measure it.

However, no neutron standard is likely to have all the properties in the above list. Which property is the most important will depend on the specific situation. The requirements regarding other reaction channels as well as the size and structure of the cross section is highly energy dependent. To reduce systematic uncertainties it is preferable to use the same, or at least the same kind of, detector setup to measure the standard and the wanted cross section. Depending on the reaction at hand, it will be easier to measure it with some setups rather than others. Listed in table 2.1 are the currently accepted standards by IAEA [8].

The neutron standards discussed in this thesis, $\text{H}(n,n)$, $^6\text{Li}(n,\alpha)t$, $^{235}\text{U}(n,f)$ and $^{238}\text{U}(n,f)$, all have different properties that distinguish them. The elastic neutron scattering of a proton, $\text{H}(n,n)$, is quite well understood theoretically [9] and is regarded as the most accurately known cross section [7]. Pure solid state hydrogen targets are not available, so one has to turn to other options. One could use a gas target with lower density than a solid target, a liquid hydrogen target (which is more cumbersome to maintain) or a solid target, like polyethylene, where other chemical elements are present. The recoil proton will have an energy similar to the incoming neutron's and, as a charged particle, it can be detected in various ways, e.g., with semiconductor detectors. Due to the two-body kinematics the energy and angle of the proton are correlated, which helps to identify wanted events and reduce the background.

Although a recommended partial wave solution, for energies up to 350 MeV, exist for the H(n,n) reaction [10], only the fission cross sections of ^{235}U and ^{238}U are currently listed as standards above 20 MeV. This means that a non-radioactive standard target does not currently exist above 20 MeV.

At the low-energy side, due to its small cross section below the fission threshold, ^{238}U is not sensitive to thermal and epi-thermal neutrons. If these neutron energies are of no interest or a disturbing thermal neutron background is present, one might prefer $^{238}\text{U}(n,f)$ to $^{235}\text{U}(n,f)$ as cross section standard. The $^{238}\text{U}(n,f)$ standard is commonly used for beam monitoring purposes. The α -activity can constitute a disturbing background but is also used to characterise the target [11] and can, in some setups, be used to calibrate the detectors.

2.1.1 Relative measurements

The concept of relative measurements is important for the measurements of neutron standards. Not only because they aspire to improve the neutron standards, to which experimentalists compare other cross sections, but also because the measurements of the standards are usually relative themselves due to the difficulties of detecting neutrons directly.

The cross section σ can be expressed as

$$\sigma = \frac{N}{\varepsilon \phi n}, \quad (2.1)$$

where N is the number of experimentally detected events, ε the total detection efficiency, ϕ the neutron fluence and n the number of target nuclei. By comparing the number of measured events to another cross section measured using the same fluence, we instead get

$$\sigma = \frac{N}{N'} \frac{\varepsilon'}{\varepsilon} \frac{n'}{n} \sigma', \quad (2.2)$$

where the primed variables denote the properties of the reference measurement. The cross section can be derived without knowing the neutron fluence, ϕ , but instead one needs to measure two different reactions, as well as having access to a well known cross section σ' . This, unfortunately, brings additional random and systematic uncertainties to the measured cross section.

2.2 Nuclear structure

Both the neutron and the proton are fermions, so they cannot have the same set of quantum numbers as any other of their species, i.e., they have to abide by the Pauli principle [12]. Nucleons, bound in a nucleus, occupies the most energetically favourable states, while states of higher energies are left vacant

unless excitation energy is available. Solving the Schrödinger equation yields solutions, i.e. states, which are highly dependent on the orbital angular momentum ℓ , which interacts strongly with the particle spin s , to form the angular momentum j , in the so called spin-orbit interaction.

Analogously to atomic physics, where the orbital angular momentum plays an important role in the *aufbau principle*, the nuclear shell structure will not solely depend on the principal quantum number n , but also strongly on j . How a nuclear state couples to other quantum states will mainly depend on the angular momentum as well as the parity π of the wavefunction describing the state.

Each shell is identified by a number of states of similar energies, separated from other shells by an energy interval void of states. If a shell is completely filled, i.e. closed, it will require much more energy to add an extra particle to the next unoccupied level since it will have to reside in the next shell. Together with the fact that the energy drops as the total angular momentum sum to zero when all the degenerate states of a nuclear level are filled, this makes shell closure favourable.

The total number of protons or neutrons present as the last nuclear level of a shell is filled up, is called a magic number. The six first magic numbers are listed in table 2.2. As the nuclei becomes large or heavily deformed the magic numbers might change. The increasing number of inter-nucleon interactions and possible non-spherical shapes can push levels both up or down. Discovering new magic numbers is one reason many nuclear scientists look into super-heavy nuclei and nuclei far from stability.

An interesting example is fission fragments close to the neutron drip line where interactions with the unbound continuum states may shift levels and quench the high numbered shell gaps [13]. Experimental evidence exists that support a shift of the proton levels of tin isotopes with increasing neutron number [14]. New magic numbers are possible if any of these shifts changes the existing gap structure in the nuclear level scheme. Other experimental data [15] show a preference for the creation of fragments with $Z = 54$, possibly indicating a new proton magic number, but the theoretical explanations for this are lacking.

2.3 Compound reactions

As a particle impinge on a nucleus there are two extremes of how a reaction can occur. It either interacts with one or a few nucleons separately in a direct reaction, or with the nucleus as a whole in a compound reaction. Which is more probable depends on the wavelength. The diameter of an atomic nucleus is around a few fm and generally speaking the incoming particle needs a smaller wavelength than that to single out any specific part to interact with. Particles of larger wavelengths will not be able to ‘see’ or interact with the constituents.

Table 2.2. *The first six magic numbers with their associated nuclear levels and occupancy numbers. The numbers are valid for both protons and neutrons separately for nuclei not far from stability.*

Single particle states	Number of states	Magic number
$1s_{1/2}$	2	2
$1p_{3/2}, 1p_{1/2}$	6	8
$1d_{5/2}, 2s_{1/2}, 1d_{3/2}$	12	20
$1f_{7/2}$	8	28
$2p_{3/2}, 1f_{5/2}, 2p_{1/2}, 1g_{9/2}$	22	50
$2d_{5/2}, 1g_{7/2}, 3s_{1/2}, 2d_{3/2}, 1h_{11/2}$	32	82

A neutron has a wavelength of about 30 fm at 1 MeV while it decreases to 5 fm as the kinetic energy reaches 30 MeV. This means that low energy neutrons of a few MeV are unlikely to induce direct reactions while neutrons of a few tens of MeV can be said to be of intermediate energies, capable of utilising both mechanics.

The compound reactions will be the predominate reaction mode in the projects presented in this thesis, and thus deserves a bit more attention. As the neutron is absorbed by the target nucleus, and an intermediate compound nucleus will be formed. The intermediate state will typically survive for attoseconds or more, i.e., much longer than it would take the incoming neutron to traverse the nucleus. That time is enough for the incoming energy to be thermalised by multiple intra-nuclear collisions, so that the compound nucleus will, in the extreme case, completely ‘forget’ how it was formed. Consequently, the compound nucleus decay channel will be independent of how the compound nucleus was formed.

While a direct reaction would usually be an interaction with a single particle state, a compound reaction involves the state of the whole nucleus. The likelihood of a reaction occurring (reaction cross section) will depend on how well the incoming particle wave overlaps with the intermediate state, as the particle is captured within the compound nucleus. If the particle energy would be such that the intermediate state is close to a nuclear level in the compound nucleus, the cross section is greatly enhanced and it is said to be a resonance reaction. Contrary to the levels in the continuum, these resonances are long-lived with well defined widths.

The cross section close to a single resonance can be described by a Breit-Wigner distribution where the proportionally constant depend on the properties of the resonance level as well as of the incoming particle. It can be written

$$\sigma = \frac{\lambda^2}{\pi} g \frac{\Gamma^2/4}{(E - E_R)^2 + \Gamma^2/4}, \quad (2.3)$$

where λ is the particle wavelength, Γ the resonance width, E the particle energy, and E_R the resonance energy. The statistical factor g describe how the incoming particle spin s_p , and the target nucleus spin s_n , can couple with the orbital angular momentum ℓ , to match the total angular momenta I of the resonance:

$$g = \frac{2I + 1}{(2s_p + 1)(2s_n + 1)}. \quad (2.4)$$

In addition to affecting the cross section, the resonance state will also affect angular distributions of emitted particles. Resonance reactions are of particular importance in the measurement described in chapter 6.

2.4 Fission

Many heavy nuclei can undergo spontaneous fission, but the naturally abundant ones will do so only at low rates. Fission of a nucleus can also be induced, if an incoming particle is absorbed. For charged particles this means that the Coulomb repulsion must be overcome in order to reach the nucleus, while γ - and neutron-induced fission are not affected by this. The discussion will mostly be restricted to neutron-induced fission, which is the most relevant for this thesis.

Regardless of how the fission process was initiated, it will typically lead to a heavy nucleus being split into two highly excited *Fission Fragments* (FFs) of about half the mass of the fissioning nucleus and an energy release of about 200 MeV. The energy comes from the fact that the mass of the final state is less than the original nucleus, since the daughter nuclei are more tightly bound.

Occasionally, other light particles can be emitted in the moment of scission. These are predominately α -particles and are referred to as ternary particles coming from a ternary fission. In binary fission, the two heavy FFs repel each other and leave the fission site collinearly. If a ternary particle is present the collinearity is broken, but due to the mass differences the ternary particle leave in almost a straight angle to the FFs' trajectories, repulsed by the Coulomb force. Since ternary fission is much less likely than binary, the discussion is restricted to the binary case although many things are applicable to ternary fission as well.

The energy that was not transformed into kinetic energy is stored as excitation energy in the newly formed nuclei. Both FFs will have, on average, a similar ratio of neutrons to protons as the mother nucleus. However, since a FF is much lighter than the mother nucleus, it has a neutron excess, i.e., more neutrons than any stable isotopes of the specific element. Neutrons are therefore easily emitted if enough excitation energy is available to pay for the neutron separation energy. In general, as many neutrons as possible are emitted by the excited nucleus, until the excitation energy is so low that deexcitation is

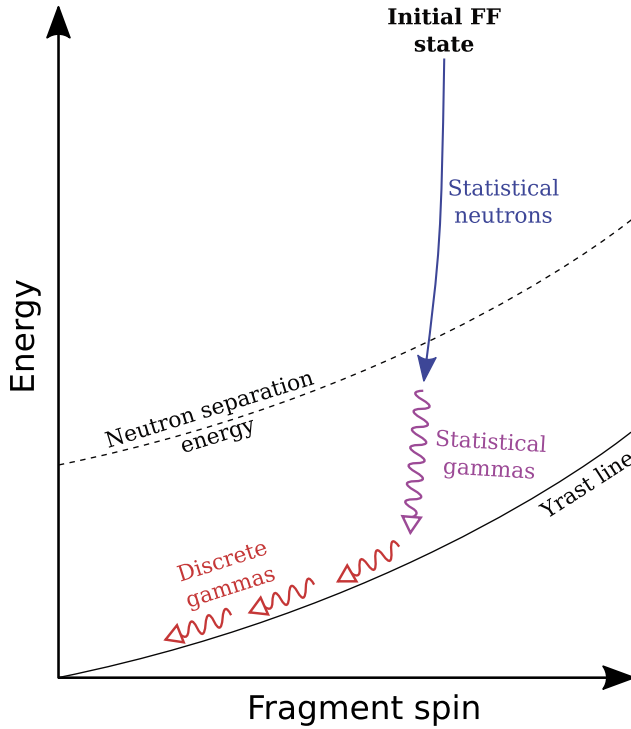


Figure 2.1. A schematic view of the prompt radiation from a FF. As the neutron emission takes the system close to the yrast line, prompt γ -decay takes over, followed by discrete γ -decays down to the ground state.

only possible through γ -decay. Both the neutron and γ emission happen very quickly (within 1×10^{-14} s) and are referred to as prompt emissions.

The FFs are generally formed with some angular momentum, but the statistically emitted neutrons and γ 's do not carry away much of this. The neutron emission will therefore be limited by the yrast¹ line, defining the lowest possible energy state as a function of fragment spin. When the excitation energy becomes so low that the difference between it and the yrast energy is less than the neutron separation energy, no more neutrons are emitted. Instead statistical γ -decays will take the excitation energy down to the yrast line, followed by discrete γ -decays along the yrast line down to the ground state. As illustrated in fig. 2.1, most of the angular momentum is carried away by the discrete γ 's. This means that the energy below the yrast line for the prescribed spin is inaccessible for the neutron emission.

Neutron emission is usually assumed to occur after the fragments are fully accelerated. However, there is a slight chance for a FF to emit a neutron during the acceleration phase [16]. When that happens the laboratory energy of the

¹Yrast is a Swedish word meaning dizziest.

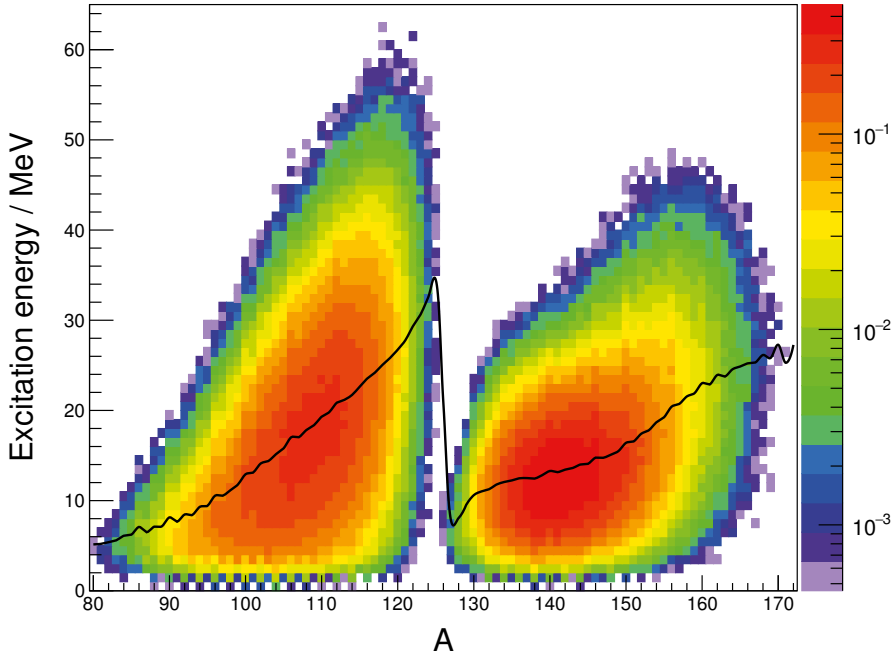


Figure 2.2. The excitation energy as a function of mass calculated using the GEF code [16] for $^{252}\text{Cf}(sf)$. The two-dimensional histogram has been normalised to 200 % and the solid line represents the average.

neutron will be less on average, seeing that the Lorentz boost will not be at full power. The probability for neutrons being emitted during the acceleration phase increase with excitation energy.

The share of the *Total Kinetic Energy* (TKE) each FF receive is inversely proportional to the FF mass, due to momentum conservation. The distribution of *Total Excitation Energy* (TXE) between the two fragments is more complex. Figure 2.2 shows an example of how the excitation energy varies with fragment mass. Since prompt neutron emission carries away most of the excitation energy, a prompt neutron multiplicity measurement is a probe of the initial excitation energy of the FFs and how energy is divided between the pre-fragments during fission. Measuring the prompt γ spectrum as well exposes information about the FF spin.

After the prompt neutron emission, the FFs are instead called *Fission Products* (FPs). They will often still have a neutron excess which makes them β -unstable. Later emissions, usually promptly following a β or other decay, are possible. A small fraction of the total number of neutrons come from such a mechanism and are called (β -)delayed neutrons, which are very important for safe operation of nuclear reactors.

In contemporary commercial reactors the main fuel is the nucleus ^{235}U because it is the only naturally abundant fissile nucleus. A fissile nucleus will

gain enough energy, by absorbing even a thermal neutron, to overcome the fission barrier. The fission barrier is a term used to describe how the system must first go up in potential energy as the short-ranged strong force weakens when the nucleus starts separating into two parts. While quantum mechanical systems can tunnel through barriers, it is much more likely for a system to pass a barrier if a large excitation energy is present. When a nucleus absorbs a neutron, it gains the neutron separation energy as excitation energy in addition to the kinetic energy contribution, as the neutron becomes bound.

How much energy is gained will vary. ^{235}U is a nucleus with an even number of protons, but odd number of neutrons. Pairing the absorbed neutron with the last valence neutron is favoured, since the spins can be opposed and thereby minimises the angular momentum. In effect, the new nucleon is more tightly bound, leaving more energy as excitation energy.

In the ^{235}U case, 6.5 MeV is gained, which is enough to overcome the fission barrier of ^{236}U . Contrary, for the non-fissile nucleus ^{238}U , the absorbed neutron cannot pair up and consequently the resulting binding energy is lower. In turn, that leads to a lower excitation energy of 4.8 MeV in the compound system ^{239}U which is below the barrier height. Not until the incoming neutron carries about 2 MeV can the ^{239}U nucleus pass the fission barrier with ease. Such nuclei, that need the incoming neutron to carry enough energy to be able to get above the fission barrier are called fissionable. In the case with ^{239}U it can form the fissile nucleus ^{239}Pu through two subsequent β -decays, which is why ^{238}U is also called fertile.

The presence of a fission barrier can be explained by the *Liquid Drop Model*, but many of the detailed properties of fission requires a more advanced model. The LDM in its simplest form only account for the nucleus' volume, surface, and Coulomb repulsion (but usually also includes the asymmetry and pairing terms). Therefore, it can predict many average properties and general trends, but misses out on specific interactions between the single-particle states. On the other hand, just summing all single-particle energies, which obviously takes shell effects into account, have not had much success reproducing all macroscopic quantities. Strutinsky realised how the two approaches could be combined by taking the energy calculated using the LDM and adding a correction term based on the average shell effects [17]. This can be performed for different nuclear shapes and deformations, thus creating an energy potential landscape describing the fission barrier.

Already the separation distance of the two mass centres can explain several features of the fission barrier. As the nucleus elongates, shell structure plays an important role in determining the shape of the barrier. The energetically favoured states will shift as the distance increases. When an occupied state crosses another state with the same spin and parity, the most energetically favoured state will become the occupied one. This phenomena creates a local well on top of the fission barrier and appears as soon as the shell effects are taken into account, even in the average form devised by Strutinsky [17].

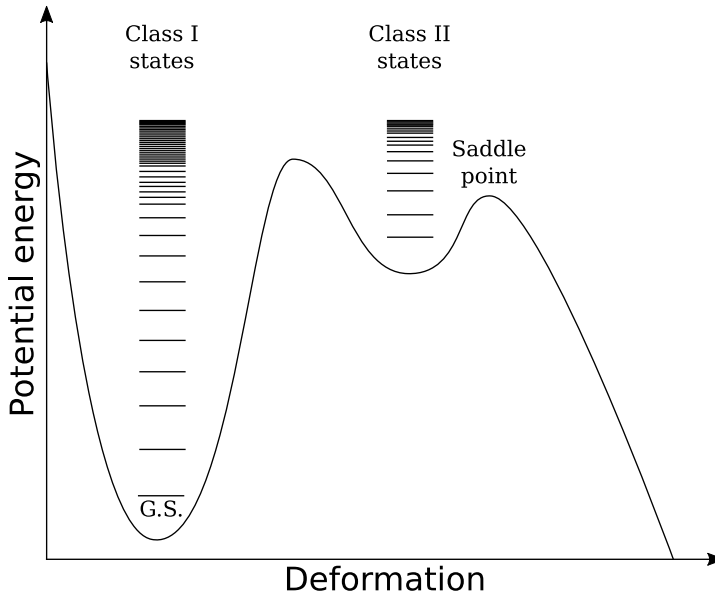


Figure 2.3. Schematic illustration of a typical fission barrier. The deformation axis describes how the deviation from a spherical configuration evolves from a deformed ground state (G.S.) to a shape dominated by two mass centres connected by a thin neck, as the fission process progresses.

In fig. 2.3 a typical fission barrier in the actinide region is illustrated. Which deformation parameters that are used depend on the model, but the x -axis in fig. 2.3 should be interpreted to start at a spherical configuration and to end in a more dumbbell shape ready to fission. Different incoming particles couple differently to the less deformed class I states and thereby have different probabilities of triggering resonance conditions. As with all nuclear reactions, resonances can greatly enhance the reaction rate. The interplay between the class I states, the meta-stable class II states, as well as the transition states, especially at the saddle point, influences how the system reach scission. The final shape and properties before scission determines the yield and angular distribution.

The separation distance between the two mass centres of the two forming FFs might be an intuitive parameter, but it is not enough. The fission barrier must be described in a multidimensional potential landscape. Möller et al. used five parameters in order to reproduce many of the features of fission: elongation, mass asymmetry, deformations of each forming fragment, and neck thickness [18].

As one deviates from the simple one-dimensional fission barrier it can sometimes be difficult to assign one particular barrier for each nucleus. The fissioning nucleus may take any possible path through the potential landscape. When it reaches a saddle point where fission is inevitable, the neck holding the

nucleus together will get thinner and longer until it raptures and two separate FFs are formed. Every path is possible, but not equally probable due to its unique way of traversing the multi-dimensional fission barrier. Fission of a nucleus like ^{236}U is dominated by asymmetric modes [19] while symmetric pre-fission shapes are much less likely. A simple explanation for this is that the heavier of the forming FFs can lower the system's energy by adapting a near spherical shape close to the doubly magic $^{132}_{50}\text{Sn}$ configuration. The asymmetric pre-fission shape then naturally leads to the an asymmetric mass distribution as the FFs are formed.

It is observed experimentally, that while the light mass peak move with the compound nucleus mass, the heavy mass peak stays more or less the same over a large range of fissioning systems in the actinide region. This is in good agreement with the closure of the $Z = 50$ and the $N = 82$ shells. The light fragment in this mass region does not have any shell closures in range and is therefore less restricted to any certain mass numbers. As the energy of the incoming neutron is increased, the higher potential barrier of symmetric fission becomes less important, thus making the symmetric mode more competitive.

The TKE as a function of mass increase as the the two fragments get similar masses, since the Coulomb repulsion is proportional to the product $Z_1 \cdot Z_2$. In the case of $^{252}\text{Cf}(sf)$ the Q -value also peaks close to symmetry leaving a maximum amount of energy available. However, close to symmetry the TKE exhibits a local minimum (fig. 2.4). This is a sign of a different fission mode in this mass region: a *Super Long* (SL) mode in the terminology of Brosa et al. [19], where the two mass centres are formed at a greater distance which decreased Coulomb potential energy as a consequence.

In an attempt to find out how fission proceeds Randrup and Möller allowed the system to take random walks [20] on their calculated five-dimensional potential landscapes [18]. The walk was not entirely random since the probability of each step was weighted by the potential difference in a similar fashion as in the famous work of Metropolis et al. [21]. That is, the system is allowed, but discouraged, to step up in potential energy. Observing where in the potential landscape the walks end up, i.e., how scission is reached, gives a picture of the evolution of the fission process.

The angular distribution of the FFs, with respect to the incoming neutron, is an important experimental observable since it contains information about the states and modes [19] during the fission process. As new transition states become energetically available the *Fission Fragment Angular Distribution* (FFAD) is influenced by the quantum numbers of those states making it a highly energy dependant observable. Especially when new chances of fission open up with increased neutron energies [22], the deviation from isotropic emission (anisotropy) of FFs can suddenly change due to the completely new states that become available.

Fission is a complicated many-body system that we still lack detailed understanding of. It is therefore still interesting to measure FP yields to greater

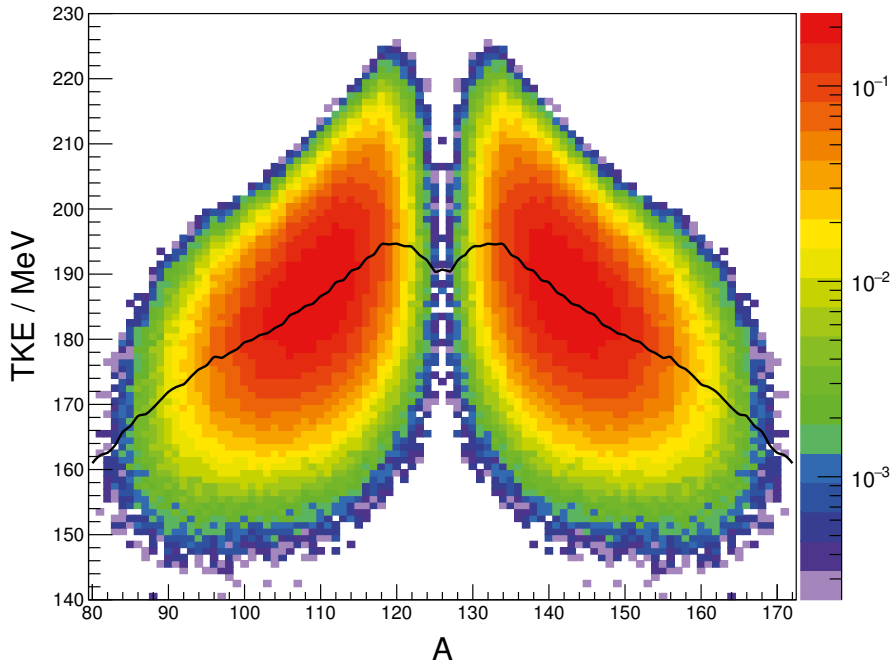


Figure 2.4. TKE as a function of mass calculated using the GEF code [16] for $^{252}\text{Cf}(sf)$. The two-dimensional histogram has been normalised to 200 % and the solid line represents the average.

precision and accuracy, as well as measuring several observables at once to see how they correlate. The two projects described in chapter 8 and chapter 7 are both related to the quest of understanding fission better, by attempting to provide better data for both theorists as well as applications in industry.

3. Particle detectors

Your "discovered boson" which was detected in the LHC, is simply one Xenon atom of the 1 trillion 167 billion 20 million Xenon atoms which there are in the LHC!

— Gabor Fekete

The choice of detector depends on the situation and will be affected by, e.g., particle species, solid angle coverage, background situation, and of course what information the experimentalist is after. In all of the experiments covered by this thesis, the detected particles are either heavy nuclei, i.e. FPs, or light charged particles (p, d, t, ^3He , or α -particles). In none of them are neutrons ever directly detected. In particular, the different stopping ranges of these particles, give rise to different preferences and challenges when one tries to decide on a suitable detector system.

The most straight forward way of detecting a fission event is by detecting the FPs. As they are heavy ions, they give rise to high amplitude signals in many gas detectors and near 100 % detection efficiency. However, for the same reason they also suffer from short stopping ranges even in low density materials. In solid state detectors the charge density due to the stopping of the ions give rise to plasma effects that must be compensated for. In thick targets many FPs will not be able to reach the outside of the target. Thin targets can be made through different kinds of deposition techniques [23, 24]. The kinematics can also be of help, especially if both fragments are detected, since they will typically travel in almost opposite directions in both the *Centre-of-Momentum* (CoM) and the laboratory frame of reference. However, due to the incoming momentum of the neutron and the prompt neutron emission, the fragments will generally have an angle different from 180° between them. This leads to a requirement for a larger solid angle coverage, which often is easier using gaseous detectors.

Contrary to the FPs, light particles like protons can be detected in solid state detector, e.g. silicon detectors, with high resolution. The high penetration of these particles can make them more difficult to detect in gas detectors, but already α -particles have a significantly shorter stopping range than protons.

In the following sections I will describe the different detectors used in this thesis, and try to outline how they work as well as their most basic properties.

3.1 Frisch-gridded ionisation chambers

A non-gridded gas detector can be used to measure the energy a particle deposits in the detection gas. It is simply a volume of gas with an applied electric field across it. When an ionising particle is stopped in the chamber gas, the energy it deposits in the stopping material enables the atomic or molecular electrons to break free from their orbits, effectively creating pairs of positive ions and free electrons. The number of pairs are proportional to the amount of energy lost by the particle. As we will see later on, the positive ions are of less interest since their contribution to the obtained electronic signals can be completely neglected.

However, in such a setup, the signals induced on the electrodes will not be straight forward to analyse. The distance to the electrode, at which the electrons are created, influences the amount of charge that is induced on the electrode. There is a remedy for this though. By introducing a conducting grid between the cathode and anode at an intermediate bias it is possible to get an anode signal proportional the energy and also deduce the angle of the particle, given that it originates from the cathode, i.e. the target or sample should be placed on or be part of the cathode. This kind of setup goes under the name *Frisch-Gridded Ionisation Chamber* or just *Gridded Ionisation Chamber* (GIC). How it works will be described in the following section.

3.1.1 Obtaining angular information

In order to later follow the discussion of the signal analysis more easily, it is well worth spending some time seeing how these signals are generated in some detail. Some handy notation, that will be used subsequently, is collected in table 3.1. Most of the notation is also depicted in fig. 3.1 or fig. 3.2. To begin with, we will assume that the conducting grid completely shields the anode from the cathode and vice versa. We will also assume that it is 100% transparent to electrons. None of these assumptions are completely true, but corrections for deviations from this ideal model can be made later. The electrode voltages should be chosen with the transparency in mind. For mesh grids, a study has been made by Bevilacqua et al. in Ref. [25].

When an electric charge q , drifts towards an electrode it will induce a current on the electrode. The integrated charge Q can be expressed as

$$Q = q (\varphi(\mathbf{x}_f) - \varphi(\mathbf{x}_i)), \quad (3.1)$$

where Q is a function of the weighting potential $\varphi(\mathbf{x})$, according to the Shockley-Ramo theorem [26]. The weighting potential is evaluated at the final, respectively initial, position of the moving charge q . The weighting potential is similar to the electric potential in absence of the moving charge, but it is a unitless quantity, with unit value on the electrode of interest and zero on all other conductors. That is, it is independent of the actual values

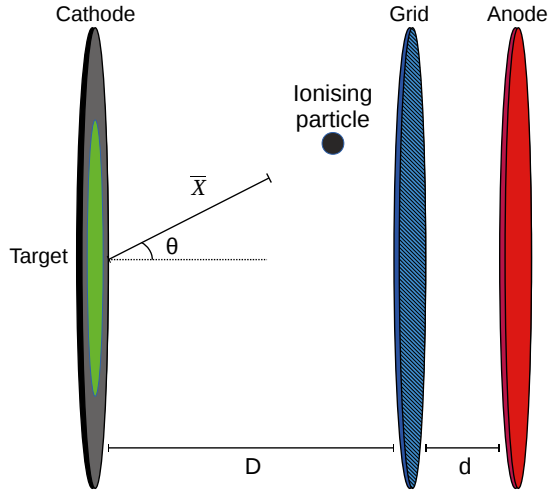


Figure 3.1. Schematic of the chamber electrodes. The emitted particle will leave a track of liberated electrons. The mean distance from the particle origin of these electrons is denoted \bar{X} .

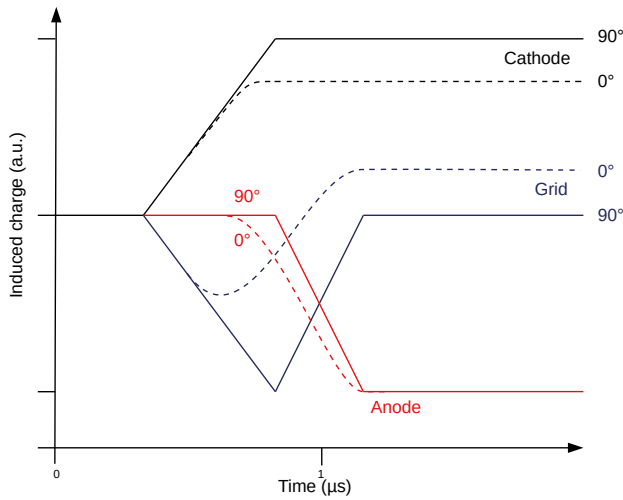


Figure 3.2. Schematic of the signals induced on the electrodes upon incoming ionising radiation. The solid lines correspond to particles emitted along the target surface. The dashed lines corresponds to particles emitted from the target along the chamber axis (perpendicular to the target surface). The time scale is approximate.

Table 3.1. *Useful notations for discussing how the different signals in a Frisch-gridded ionisation chamber are generated.*

Symbol	Description
D	The distance between the cathode and the grid.
d	The distance between the grid and the anode.
Q_C	The charge induced on the cathode.
Q_G	The charge induced on the grid.
Q_A	The charge induced on the anode.
PH	Pulse Height, in this section defined as the difference of the voltage level immediately after and before the induced signal.
$\varphi(\mathbf{x})$	The weighting potential at \mathbf{x} .
\mathbf{X}	The position of the electron cloud's centre-of-gravity.
\overline{X}	The distance between \mathbf{X} and the cathode, along the particle track.
θ	The polar angle of the particle track with respect to the beam axis (and chamber) axis.
N	The number of created electron-ion pairs.

of the electrode voltages, which will only take part by determining in which direction the charge is moving. Its value can still be determined using the Laplace equation,

$$\nabla^2 \varphi = 0, \quad (3.2)$$

much similar to Poisson's equation in electrostatics with a zero charge density.

Due to the grid, moving charges in the space between the cathode and the grid, will only affect the cathode and the grid, not the anode. Once they drift past the grid they will no longer affect the cathode but instead induce a charge on the anode. In addition, since they now travel away from the grid, the sign of the charge they induce on the grid must be opposite compared to what is was before. Consequently, all electrons, no matter where in the space between the cathode and the grid they were created, will drift the same distance between the grid and the anode. Therefore, they will all induce the same amount of charge on the anode. From eq. 3.1 we get

$$Q_A = -Ne (\varphi(\mathbf{x}_{\text{anode}}) - \varphi(\mathbf{x}_{\text{grid}})) = -Ne, \quad (3.3)$$

where the electric charge q has been put equal to the total electric charge of all the electrons, $-Ne$. We conclude that the anode signal will be proportional to the deposited energy in the gas.

In addition to removing the angular dependence of the anode response, the signal from the grid itself also provides direct angular information. If a single free electron was to be created at the surface of the cathode, it would drift through the grid until it reached the anode. On its way towards the grid it

would induce a negative charge and after passing the grid it would induce exactly the same charge but with opposite sign. The final *Pulse Height* (PH) of the grid signal would be zero. If the electron instead was created further away from the cathode, the charge induced on the grid while travelling towards it, would be less since the distance travelled would be less. The final PH of the grid signal would in this case be positive. This effect can be exploited in order to determine the angle of the incoming particle. We will see how this can be done, by deriving an expression for the PH of the induced charge on the grid, Q_G .

The weighting potential at a position x between the two electrodes can be approximated to a linear function by assuming that the electrodes are infinite parallel plates and integrating eq. 3.2 twice. That is, if x is the distance from the cathode and D , the cathode-grid distance, φ can be written

$$\varphi = 1 - \frac{x}{D}. \quad (3.4)$$

Since the detector response is due to many moving charges rather than a single electron, they are treated as if they were a single charge $-Ne$, created at the centre-of-gravity X of the electron cloud. To find the induced charge on the cathode, the Shockley-Ramo theorem (eq. 3.1) is applied using the potential from Eq. 3.4,

$$Q_C = -Ne (\varphi_{\text{grid}} - \varphi(X)) = Ne \left(1 - \frac{\bar{X}}{D} \cos \theta \right) \quad (3.5)$$

where X has been projected onto the chamber axis. The induced charge on the grid is found by noting that the total induced charge on the electrodes should be zero, i.e. $Q_C + Q_G + Q_A = 0$. The charge induced on the grid is therefore

$$Q_G = -Q_C - Q_A = Ne \frac{\bar{X}}{D} \cos \theta. \quad (3.6)$$

We have now derived an expression that shows how the grid signal will be proportional to the cosine of the particle angle with respect to the chamber axis. It is not necessary to actually measure the bi-polar grid signal, since one could just use the difference of the anode and cathode. However, the cathode and anode signals would go through different electronic amplification chains, and the difference would be more sensitive to fluctuations in the electronics. Also, in setups with a thin fission target both FPs will affect the cathode, making it difficult to disentangle the two contributions. With modern equipment including digitisers, it is straight forward to measure the grid signal and deduce the PH directly [27].

Until now, the slow positive ions have been neglected. The positive ions travel towards the cathode and therefore the induced charge, $Q_{C,G,A}^{\text{ion}}$, due to

the heavy ions becomes:

$$Q_C^{\text{ion}} = -Ne \left(1 - \frac{\bar{X}}{D} \cos \theta \right), \quad Q_G^{\text{ion}} = -Q_C^{\text{ion}} \quad \text{and} \quad Q_A^{\text{ion}} = 0. \quad (3.7)$$

The ions are about four orders of magnitude more massive than the electrons, so they have barely moved during the time the electrons were collected. Therefore, the charge induced by the positive ions during the time it takes to collect the electrons, on either the grid or the cathode, is negligible. The induction due to the heavy ions is usually not observed at all, due to the much longer time scale it happens on.

The above derivation was based on a perfect grid. In reality the grid will allow part of the electric field to leak through and therefore the anode is affected by the electrons even before they pass the grid. The effect is in the order of a few percent and can be corrected for. A parametrisation of the so called grid inefficiency has been made by Göök et al., derived for different types of grids [28].

3.1.2 Loss of charge and choice of gas

Since the last region the electrons will pass through is the one between the grid and the anode (the region where the induced charge will increase the grid PH), any loss of electrons will manifest itself as a more negative grid signal. In order for the electrons to pass through the grid without losses the field strength between the grid and the anode must be several times higher than the field strength between the cathode and the grid. This has been investigated by Bevilacqua et al. [25] for mesh grids, which behave differently to parallel-wire grids.

The detection gas is of importance because it will, among other things, determine the stopping power of the incoming radiation and the migration speed of the electrons. A high migration speed will reduce timing uncertainties as well as the chance of absorption of the electron. It is also important to have a constant migration speed in case the electrode voltages or the gas pressure would fluctuate a little bit. This is achieved by observing where the migration speed as a function of the reduced voltage hits a plateau (often the drift velocity saturates at high field strengths). At which voltages the plateau is found depends on the choice of detection gas or gas mixture.

The choice of gas will also affect the rate of negative ion formation as electrons are absorbed by the gas atoms or molecules. Especially the highly electron negative oxygen can play a big role since a small oxygen contamination can completely ruin the detector performance. An additive to the main gas, e.g. methane added to argon, can be advantageous since the added minority gas can de-excite meta-stable gas particles of the majority gas by collisions. This improves the energy resolution. As ionisation chambers typically are operated

below the proportional region no Townsend avalanches occurs and quenching is not needed. Suitable gas, pressure and electrode voltages are imperative for stable operation.

3.2 Parallel plate avalanche counters

The *Parallel Plate Avalanche Counters* (PPACs) are gas-filled detectors which consist of two parallel foils (often aluminised Mylar, polyethylene terephthalate, $[\text{C}_{10}\text{O}_4\text{H}_8]_n$). They are commonly used to detect heavy ions [29–31]. They are typically operated at a gas pressure of a few mbar. A thin layer (much thinner than the foil thickness) of aluminium deposited on a Mylar foil, allows for a high voltage to be applied over the gap between the foils. Upon an ionising event, this voltage will affect the electrons that are released. As they drift towards the anode, their movement will induce a voltage which will be the signal one measures. The signal is amplified by the gas multiplication process due to the high field strength. Although the PPACs are operated in proportional mode, where the induced charge on the anode is proportional to the initial number of ionisations, the energy resolution is typically not better than 20 % ($\frac{\Delta E}{E}$) [29].

PPACs for the NFS-project (described in chapter 5), are currently under development in our lab. In fig. 3.3 a setup consisting of a PPAC prototype together with a silicon detector is depicted. The detector supports were designed and 3D-printed by me for the detector tests.

PPACs are known to have good timing resolution, low stopping power and almost 100 % detection efficiency for heavy ions. The detection efficiency of these detectors improve with increasing ion mass, already oxygen ions show nearly 100 % efficiency [30].

One drawback of PPACs is that the thin Mylar foils cannot handle large pressure differences between the inside and the outside of the PPAC. A solution to this is to leave the PPACs open to the rest of the experimental chamber, filling the whole of it with the same gas under the same pressure. The alternative would be, in order to keep the electrodes unperturbed, to put extra Mylar foils separating the pressurised volume from the evacuated one. These extra foils would lead to a much higher energy loss for the fragments, than traversing a thin gas. The pressure cannot be too high if the particles traversing a PPAC need to be detected afterwards in another detector, i.e., one must make sure to limit the energy loss.

Another consideration is the additional background the Mylar might cause due to their hydrogen content. In experiments, PPACs are often placed inside the neutron beam, close to the target. Even though there are quite thin ($\sim 1 \mu\text{m}$) Mylar foils commercially available, they still often introduce a significant extra number of scattering centres for the neutrons. Elastic scattering events

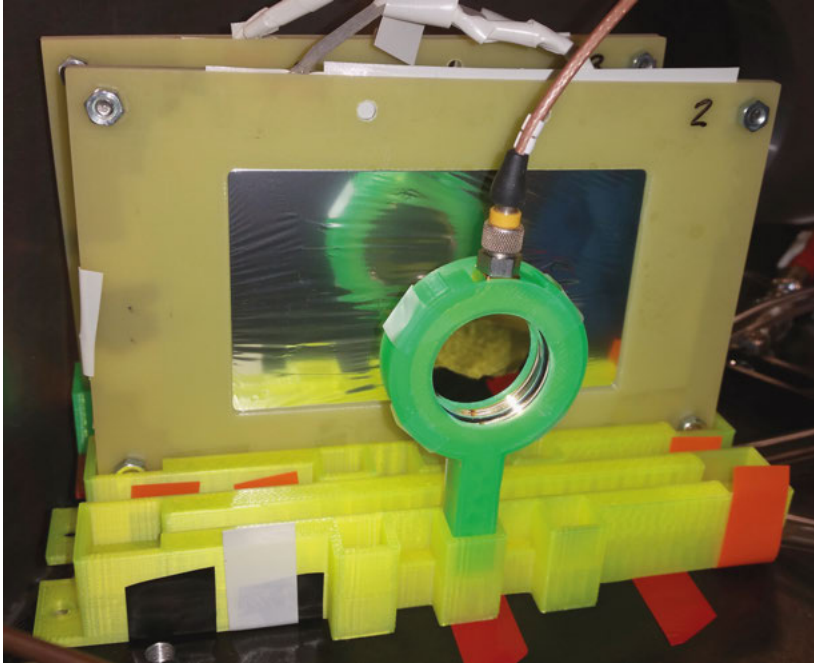


Figure 3.3. Prototype PPACs developed in our lab. The round detector in the green holder is a silicon detector while the frames behind it hold the conductive foils of the PPACs. The 3D-printed detector supports allows for several different setups of multiple PPACs and silicon detectors, and were designed for the PPAC detector development.

on, especially the hydrogen atoms, will give an increased (mostly proton) background.

3.3 Multi-channel plates

The amount of charge generated by an event one would like to detect in a experimental setup, is not always enough for standard electronics to handle. The problem can be solved if the detector itself amplifies the signal. This is what a *Multi-Channel Plate* (MCP) does. Similar to a *Photo-Multiplier Tube* (PM-tube) it makes use of accelerated electrons that kicks out additional electrons as they strike a surface. While the PM-tube uses a discrete number of dynodes at higher and higher electric potential, the MCP have continuous channels where the walls take the same role as dynodes. The channels are several micrometers wide and densely packed.

The high multiplication factor a MCP is capable of, typically more than 1×10^6 , makes it possible to detect single electrons impacting on the detector surface. But the high gains can cause production of gas ions at the channel output, which in turn might cause secondary signal pulses and decrease the

detector life time [32]. This problem is reduced by angling the channels, and further reduced by combining two plates in a so called *chevron*, i.e. v-shaped, configuration. Three plates are sometimes combined, in a similar fashion, into a so called *Z-stack*. Every incoming particle on the MCP will decrease its life time, why it is important to shield it from unnecessary exposure.

As the amplification is usually limited by space charges, it is not a suitable detector for energy measurements since the output signal will not be proportional to the incoming energy. After a saturation voltage over the MCP plate(s) has been reached further increasing the voltage will worsen the resolution [33]. It is however suitable for measuring time, since it is capable of a timing resolution in the order of hundreds to tens of ps [32, 33].

3.4 Silicon detectors

Semiconductor detectors, and especially silicon detectors, are very common detectors for a number of applications. For both experiments discussed in chapters 5 and 7 the silicon detectors are a main ingredient to the experimental setup. In both cases the detectors are used to detect both light and heavy charged particles. The detectors discussed here are of the type *Silicon Surface Barrier* (SSB) detectors, where either the n-type material at the diode junction interface is replaced by a metal, e.g., aluminium evaporated onto the silicon p-type crystal surface, or where a combination of etching and metal deposition is performed on an n-type crystal [34]. These detectors exhibit thin dead layers, essential for measuring particles with short stopping ranges.

One can divide the design of silicon detectors into two types: transmission type detectors, where particles with sufficient energy are supposed to penetrate the complete thickness of the silicon, and non-transmission type detectors, where the particle is supposed to be stopped within the thickness of the detector. The first type is always operated fully depleted, but that is not necessary for the latter mentioned type since the sensitive region do not need to extend over the penetration depth of the measured radiation.

A typical silicon detector will give about one electron per 3.6 eV deposited energy. Although the band gap is 1.1 eV not all deposited energy produces new free charges. The resolution for medium heavy particles is typically about 100 keV. Detecting light particles in well controlled environments using small detectors can decrease this value down to about 10 keV [34, p. 403].

For reasonably light particles, the stopping power and therefore also the rate of energy depositing in the detector material decreases with energy. It is also highly dependent on the charge of the particle. Both these dependencies can be utilised to determine the particle species in a, so called, telescope setup (see fig. 3.4). This method is commonly referred to as the ΔE - E method, and as the name suggests it is based on letting the particle first go through a (or several) thin transmission type detector(s) where it only deposits part of its

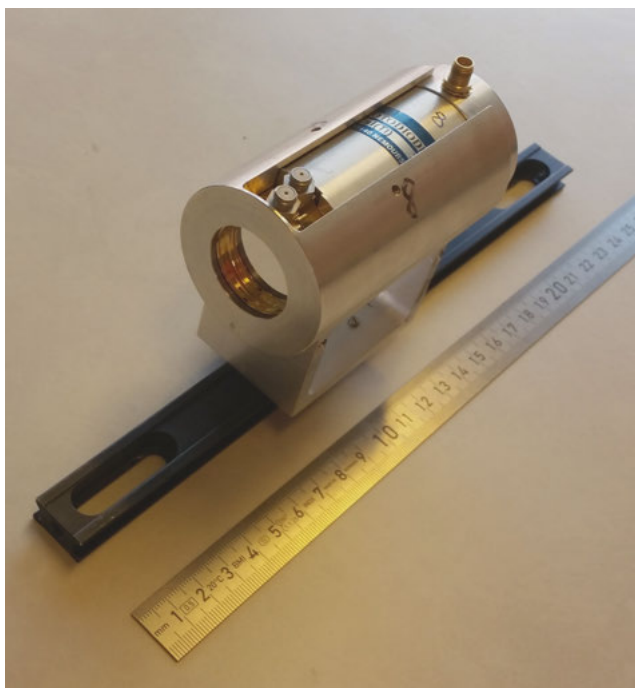


Figure 3.4. One of the detector telescopes intended to be used in the NFS-project described in chapter 5. Two silicon detectors of transmission type are placed in front of a CsI detector thick enough to fully stop the any anticipated incoming particle.

energy (ΔE). Later, at the end of the telescope, the particle is fully stopped in an adequately thick detector. One can distinguish different particles from each other by comparing the ΔE energy to the total deposited energy. Since the stopping power is also dependent on the particle mass, isotopes for lighter particles can also be readily separated in these silicon telescopes. Later, in chapter 5, a simulated plot of this kind is presented in fig. 5.4.

3.4.1 Radiation damage

As the silicon crystals are radiated, more and more lattice defects will appear. The defects can be, e.g., missing atoms, extra atoms (both silicon or other elements) in between the regular lattice positions, or larger local non-crystal structures. The defects can appear due to a number of effects. The incoming radiation can knock the lattice atoms out of position or induce nuclear reactions. They can also implant themselves in the case of thick detectors fully stopping the impinging particle. Heating up the detector (baking) and letting it cool again can ‘heal’ the detector to some degree since some smaller defects might recombine or migrate to the surface. [35]

A defect will often act as a recombination centre, thereby decreasing the output pulse. It might also act as a trapping centre where charges can be sufficiently delayed in order for them not to register together with the main pulse, effectively lowering the detected pulse height. The radiation damage in silicon detectors can be monitored by observing the leakage current. During long radiations the leakage current steadily increases as the crystal lattice in the detector gets more distorted. Especially defects that contribute energy states inside the band gap can increase the leakage current significantly. [35]

3.4.2 Detecting heavy ions in silicon detectors

Complications arise as the detected particles get heavier. For a given energy, heavier particles are slower, which give them more opportunities to pick up stray electrons from their surroundings. When a heavy ion travels through a material an equilibrium will be found where the ion continuously picks up and loses electrons at the same rate. The mean equilibrium charge (effective charge) can be parametrised to be a function mainly dependent on the atomic charge of both the ion and the surrounding atoms, as well as on the velocity of the ion [36, p. 216, 37]. Consequently, the stopping power of different FPs are comparable, the effective charge smoothing out the charge dependence, and contrary to light ions the stopping power is often the highest at the beginning of the particle trace. The short stopping range of low energetic (no more than ~ 100 MeV) heavy ions would anyway inhibit the use of a telescope setup for isotope identification, unless the ΔE detector is extremely thin.

The next complication for detecting heavy ions in silicon detectors arises from the high stopping power and the accompanying short stopping range. The cloud of free charges, i.e. a plasma, released due to the stopping process, will be concentrated in a fairly small volume. The more plasma, the bigger the effects of shielding. The electrons will feel much less of the detector bias when surrounded by a dense plasma, i.e., all the other electrons and positive holes. For the experimentalist the plasma will affect both time and energy measurements.

The charge collection time will be longer because of the reduced electric field visible to the charges. The *Plasma Delay Time* (PDT) is in the order of 2 ns for FPs. For a flight time measurement this translates into a relative error of several percents if the flight path is in the order of a meter.

The extra delay gives all the freed charges extra time to recombine before they are separated by the detector bias. For every electron-hole pair that recombines a smaller output signal will be seen. Also, a small fraction of the heavy ions stopping will be due to collisions with the silicon nuclei, and energy loss not due to collisions with electrons will not create electron-hole pairs to begin with. In addition, even thin dead layers can cause sizeable energy losses.

All these three phenomena contribute to what is called *Pulse Height Defect* (PHD).

All together these effects can cause a PHD well exceeding 10 MeV. A high detector bias can suppress the PHD to a minimum but it will still be sizeable. A common way of addressing this is to make a mass dependent energy calibration [38], with the obvious downside that one must know the mass of the ion before one can get an accurate energy reading of it. This kind of energy calibration and its implementation in the analysis of the VERDI data is further discussed in section 7.7.2.

4. Neutron facilities

Given enough startup capital and an adequate research facility, I could be Batman.

— Sheldon Cooper

All the experiments discussed in this thesis require a neutron source at some point in their project lifetimes. Creating strong neutron sources is not trivial since the primary beam will have to be charged particles that in turn creates a secondary neutron beam. What facility is suitable for an experiment will depend on the desired neutron energies, the cross section of the studied reaction which might require high neutron fluxes, *time-of-flight* (ToF) possibilities, background conditions, additional available research infrastructure etc.

The experiments related to the projects presented in chapters 5, 6 and 8 reside at three different facilities (NFS, GELINA and IGISOL, respectively) briefly introduced below. The VERDI spectrometer presented in chapter 7 is still in a development phase, but might be used at several different neutron facilities upon completion, depending on what beams are available and desirable.

4.1 NFS

The *Neutron For Science* (NFS) facility [39, 40] at GANIL in Caen, France, is part of the first phase of the SPIRAL2 project [41]. The facility is not yet operational, but the accelerator is installed and under commissioning. The plan is to have two main options for neutron production available. A continuous neutron spectrum, through the deuteron break-up reaction in a thick (8 mm) beryllium target, and a *Quasi Mono-energetic Neutron* (QMN) spectra through the ${}^7\text{Li}(p,n)$ reaction on a thin target. A high flux beam up to about the maximum deuteron energy of 40 MeV is expected from the continuous option. Using the QMN beam the peak energy can be chosen up to the maximum proton energy of 33 MeV.

The primary beam frequency of 88 MHz will be reduced by a factor of 100 to 10 000 by using a chopper. The maximum current on the converter is designed to be 50 μA , capable of generating an average neutron flux of about $2 \times 10^6 / (\text{MeV cm}^2 \text{ s})$ at a five metre distance when the beryllium converter is used.

The high flux enables measurements that otherwise would take very long time and the continuous neutron energy spectrum allows experiments to cover

the whole energy range provided that a suitable ToF technique is used. The ToF hall offers distances from the converter target from 5 to 28 m. Longer distances enable better neutron energy resolutions but at the price of lower neutron flux. At the moment, commissioning of the neutron beams is expected no sooner than late 2018. The QMN option will be the first to be tested and the full specifications will not be reached until a later date.

4.2 GELINA

The *Geel Linear Accelerator* (GELINA) [42, 43] is a neutron source that resides at the *European Commission's Joint Research Centre* in Geel, Belgium (JRC-Geel, formerly known as the *Institute for Reference Materials and Measurements*, IRMM). Just like the NFS facility will, the GELINA facility provides a pulsed continuous neutron energy spectrum. The primary beam is a linear electron accelerator capable of delivering electrons in short pulses (1 ns FWHM), with a peak current of 120 A. The electron energy can be up to 150 MeV. The neutron converter is a depleted uranium target in which the electrons are stopped emitting bremsstrahlung, which in turn causes γ -induced fission and (γ, n) reactions. The resulting neutron spectrum is peaked around 1 to 2 MeV but extends up to 20 MeV. The repetition rate is usually 800 Hz, but the accelerator can be run at lower frequencies.

The very short primary pulses together with up to 400 m long flight paths allow high neutron energy resolutions. To increase the neutron flux in the low energy range a moderator is available. The unavoidable γ -radiation escaping the neutron production target is peaked in the primary beam direction. The neutron flight paths are at angles up to 108° relative to the primary beam's direction. The flight paths at the highest angles are the least affected by the γ 's.

Access to the GELINA facility for nuclear reaction or decay data measurements, can be granted through the EUFRAT transnational access program. The access program is operated by the JRC-Geel and also includes access to other available infrastructure.

4.3 IGISOL

IGISOL stands for *Ion Guide and Isotope Separator On Line* and is a nuclear research facility at the University of Jyväskylä in Finland. Many independent proton-induced fission yields of natural uranium have been measured at IGISOL over the years [44, 45], but for the work presented in this thesis we will also take a look at a setup for neutron-induced yield measurements, that is currently developed [46, 47].

The primary beam is generated by a cyclotron and has usually consisted of 25 MeV or 50 MeV protons, for the studies of proton-induced fission. Previously the current was limited to $\sim 10 \mu\text{A}$ but a new cyclotron with a high maximum current of $\sim 200 \mu\text{A}$ has been installed. The new cyclotron has a maximum proton energy of 30 MeV which is also the energy intended for creating the secondary neutron beam for the neutron-induced case.

Regardless of how the fission is induced, the idea is that it will happen in a helium filled gas vessel. The helium is constantly flowing through the chamber in order to vent anything stopped in the gas. FPs that stop in the gas will follow the gas flow out of the vessel, where they are electrostatically accelerated into a vacuum tube. A dipole magnet acts as the first separator, which selects an isobaric chain, i.e. ions of similar mass (mass resolving power $\frac{M}{\Delta M} \sim 500$). The extracted ions will now all have the same charge, +1. The charge state choice is up to the experimentalist and the optimal choice could be ion specific, although all the experiments have used +1 as of today. To facilitate separation of the isobars after the mass selecting magnet, the ions can then be transported to JYFLTRAP [48]: a Penning trap with a mass resolving power of about 1×10^5 . In the trap, the ions with mass m , and charge q , matching the cyclotron frequency

$$\nu_C = \frac{1}{2\pi} \frac{q}{m} B, \quad (4.1)$$

will be selected while the others are discarded. This is realised through a magnet producing a magnetic field B of 7 T and the application of radio frequency fields. [44]

In the end, the ions that manage to go through the whole trap are collected on a MCP detector and thereby counted. The whole process takes less than a second and the mass resolution is enough to separate many meta-stable states from their ground state counterparts.

There are several effects in this scheme that are not fully quantified. The stopping power as well as the energy distributions are different for different isotopes so it is unclear how many of them stop in the helium gas. Which charge state they end up in is a chemical effect, i.e. element dependent, which is difficult to model. Only the ions ending up with the correct charge state for the measurement will have any chance of being detected. The spatial distribution of stopped ions in the gas, might affect the extraction efficiency from the gas-filled ion guide to the vacuum system, depending on how the gas flow looks like. To not be affected by all this, the yield measurements are usually made relative to a nearby isotope of the same element hopefully having the same net detection efficiency. The simulation work presented in chapter 8 is an attempt to start quantifying the effects of stopping efficiency in the gas better.

5. Neutron standards at NFS

*Prediction is very difficult, especially
if it's about the future.*

— Niels Bohr

A measurement of three different standard cross sections (see section 2.1) relative to each other is proposed and planned for the upcoming NFS facility (see section 4.1). Two of the reactions measured are neutron-induced fission of ^{235}U and ^{238}U , respectively. The third reaction is $\text{H}(\text{n},\text{n})$. Even though the cross section often is written $\text{H}(\text{n},\text{n})$ it is usually the recoil proton that is detected. The energy intervals in which these reactions are standards can be found in table 2.1.

At the same time, measurements of neutron-induced *Light Charged Particle* (LCP) production on a number of target materials are planned using the same setup. Both the group and the experimental setup has a history of measuring light ion production, mostly at the The Svedberg Laboratory (TSL) [49–51]. Since the experimental setup already have been used and is prepared for these kind of measurements, the focus of this chapter is mainly on the new challenges regarding the fission measurements.

This chapter will motivate why the measurements are relevant, describe the experimental setup as well as the simulations of it, and also report on the current status of the project. Many of the results of the presented simulations have previously been presented at the Nuclear Data conference 2013 [52] and as a full-sized article in Nucl. Instrum. Meth. A [53]. The text is partly adapted from my licentiate thesis [5].

5.1 Motivation

Cross section measurements of LCP are lacking in the energy region above 14 MeV. Taking the setup previously operated at TSL to the new NFS facility would allow cross section measurements up to 40 MeV, supplementing existing studies [54–57]. The cross sections will be double-differential, with respect to energy and the emission angle of the secondary particle.

Many industrial applications exist for such cross sections. In electronics, neutron-induced single-event effects in silicon are of interest [58]. Cross sections for LCP from carbon and oxygen nuclei have applications within the field of neutron therapy [59]. The development of new reactors, both fission

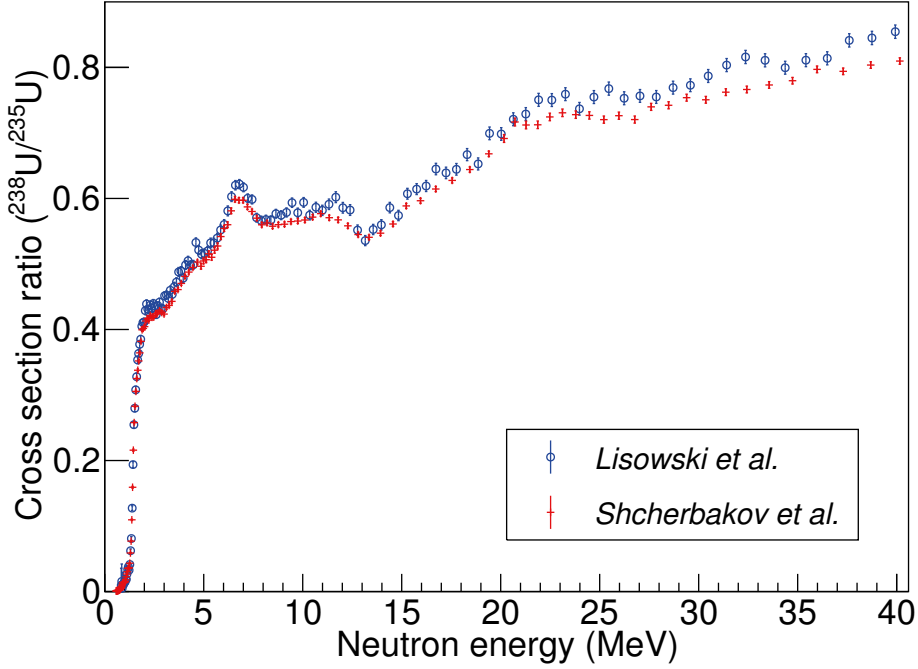


Figure 5.1. Both Lisowski et al. [64] and Shcherbakov et al. [65] measured the fission cross section of ^{238}U relative to the ^{235}U fission cross section. For energies above 20 MeV the Lisowski et al. data clearly lies systematically higher than the data from Shcherbakov et al. Only the neutron energy range relevant for the measurement discussed in this thesis is shown, the systematic differences become even larger for higher energies (up to 200 MeV, where the Shcherbakov et al.'s data ends).

and fusion ones, requires knowledge of proton and α -particle production in construction materials since the gas can cause swelling and embrittlement after heavy radiation [60]. This makes measurements on, e.g., iron relevant. The nearby field of *Accelerator Driven Systems* (ADS) as well as aviation [61] and spaceflight [62], all need cross sections on several nuclei in this energy region for accurate dosimetry [63].

The fission cross sections are relevant for nuclear power but also for neutron monitoring and of course as neutron standards. The fission cross section of $^{238}\text{U}(n,f)$ was not accepted as a standard by the American ENDF/B evaluation until version ENDF/B-VII. From the fission threshold, at about 2 MeV up to 20 MeV the standard is well known, but for the higher neutron energies some disagreements between different datasets exist. Two of the somewhat recent measurements, made by Lisowski et al. [64] and Shcherbakov et al. [65], are in disagreement. Especially for the higher neutron energies towards 200 MeV, the cross section ratio measured by Lisowski et al. is systematically higher, which is seen at lower energies, above 20 MeV, too (Fig. 5.1). Both Lisowski et al. and Shcherbakov et al. measured against the $^{235}\text{U}(n,f)$ reaction (Lisowski

et al. however, also employed two proton-recoil telescopes as beam monitors). Several newer measurements have been made, but without fully resolving the discrepancies.

Two other measurements both relative to the $^{235}\text{U}(\text{n},\text{f})$ cross section were conducted, using different setups, at the CERN n_TOF facility [66]. Their measurements support the Lisowski et al. data rather than the Shcherbakov et al. data.

Contrary to the previously mentioned measurements, Nolte et al. [67] measured $^{238}\text{U}(\text{n},\text{f})$ relative to $\text{H}(\text{n},\text{n})$. Nolte et al. utilised a QMN beam, covering a number of different energies ranging from 33 to 200 MeV. The Nolte et al. data slightly favours Lisowski et al.'s but the uncertainties, in the order of 4 to 5 %, are too large to make a clear judgement.

There seems to be strong support for the Lisowski et al. data. Nonetheless, a measurement relative to the $\text{H}(\text{n},\text{n})$ standard, with smaller uncertainties than achieved by Nolte et al., would still be valuable, considering the importance of the all three involved standards. By measuring $^{238}\text{U}(\text{n},\text{f})$ against both $^{235}\text{U}(\text{n},\text{f})$ and $\text{H}(\text{n},\text{n})$, one can evaluate and investigate possible discrepancies both in the $^{238}\text{U}(\text{n},\text{f})/^{235}\text{U}(\text{n},\text{f})$ ratio as well as when comparing against the $\text{H}(\text{n},\text{n})$ cross section.

5.2 Experimental setup

The previous Medley setup [51] is now being upgraded in order to cope with a new experimental situation. Previously it was used at (TSL) with a QMN beam, mostly at 96 and 175 MeV. The continuous energy range at the NFS facility, when a beryllium neutron production target is used, requires us to measure the ToF to determine the neutron energy. We have developed our own PPACs [68] to be placed close to the target (fig. 5.3), in order to detect the FPs and obtain a precise ToF measurement.

A schematic of the experimental setup is found in fig. 5.2. The Medley vacuum chamber has a cylindrical shape (about 35 cm high with a 90 cm diameter). The total chamber volume is about a quarter of a cubic metre. Since we will now use PPACs, the vacuum chamber will be filled with a low pressure gas. In the centre of the chamber a cylindrical target is placed at a 45° angle to the beam axis. Surrounding the target are eight detector telescopes at a distance of about 15 cm from the target centre. At each side of the target, a PPAC is positioned as close to the target as possible, in order to provide the best possible time resolution. The target area is depicted in fig. 5.3 where also the stacked target is depicted (see section 5.2.2).

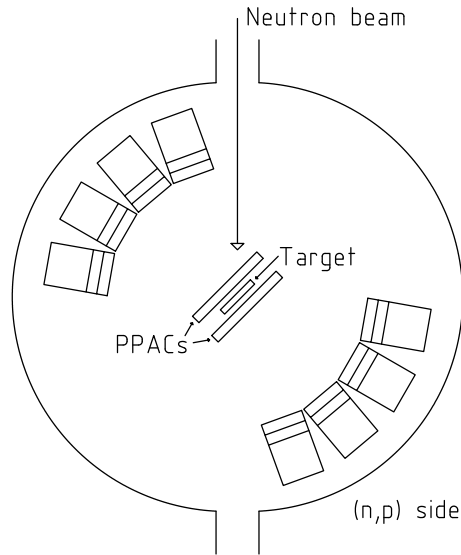


Figure 5.2. Schematic of the Medley setup. It consists of eight detector telescopes directed towards the middle of the chamber where the target is put. Two PPACs will be installed close to each side of the target. The recoil protons from the elastic neutron scattering on hydrogen nuclei can, of kinematical reasons, only be detected in the forward direction.

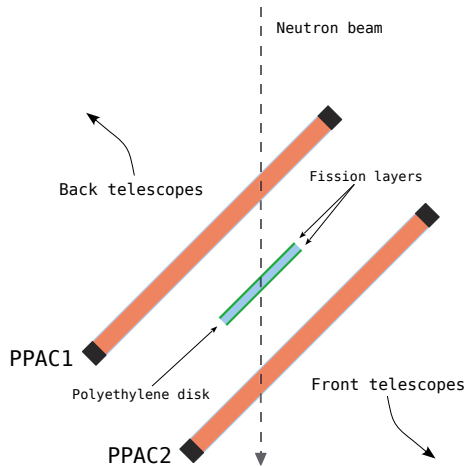


Figure 5.3. Sketch of the area close to the target. We employ a stacked target to measure FPs from the fissionable outer layers as well as recoil protons from the polyethylene core. The PPACs are placed close to the target in order to minimize the flight path of the emitted FP.

5.2.1 Detector telescopes

Each telescope consists of three independent detectors, chosen in order to be able to detect light ions with the ΔE - ΔE - E technique. In the front of each telescope, facing the target, is a thin (50 μm), fully depleted, silicon detector. It is followed by another fully depleted silicon detector of similar or larger thickness. The third detector is a CsI(Tl) crystal optically coupled to a photodiode. It has to be thick enough to fully stop any particle that the telescope measures. The aperture areas of the silicon detectors are 450 mm^2 each, which corresponds to about 20 msr per telescope at a 15 cm distance. Because of the width of each telescope, all eight telescopes cannot be fitted into the chamber if a smaller distance than 15 cm is used. A larger distance, up to about 30 cm, is possible but with a smaller solid angle as a result. A photo of one of the telescopes was shown previously in fig. 3.4.

The telescope angles are, under normal circumstances, fixed with respect to each other. However, the whole setup of eight telescopes can be collectively rotated in order to cover other angles or to estimate systematic uncertainties by rotating it 180°. Our ‘standard’ setup has the telescopes positioned at 20° intervals and the smallest angle covered by it is 20°.

We will also use the telescope detectors to detect FPs, but in that case the front detectors will not be penetrated, but instead fully stop the FPs. Similarly to how the recombination causes PHD due to the plasma effects in the silicon detectors (section 3.4.2), nuclear reactions in the CsI detectors can cause the incoming light ions to seemingly deposit less than their full energy in the detector. This effect has been studied before and was shown to be less than 2 % for 40 MeV protons [69]. It was also found, in the same study, that the effect can be precisely reproduced by simulations and therefore corrections for this can be made.

The detection efficiency ε in Eq. 2.2 can be expressed as

$$\varepsilon = \frac{\Omega}{4\pi} \times \varepsilon_{\text{Si}} \times \varepsilon_{\text{PPAC}}, \quad (5.1)$$

where the first factor is the efficiency due to the covered solid angle, Ω , and ε_x is the detector efficiency for detecting the impinging particle in the specified detector (PPACs are only applicable in the case of detecting FPs). For charged particles, energetic enough to leave a clear signal above the noise level, $\varepsilon_{\text{Si}} \approx 1$. To first order, the solid angle for detecting FPs and for detecting the recoil protons from elastic scattering is the same. It is only dependent on the silicon detector aperture and the distance to the target. However, since FPs have a very high linear energy loss in solid materials, there is a possibility of an energy dependent decrease of the active detector area due to, e.g., the presence of glueing near the edges of the silicon surfaces. The extent, if any, of this effect will be investigated using a californium source.

5.2.2 Stacked target

In order for Eq. 2.2 to be valid, the flux ϕ of the cross section measurement must be the same as the one of the reference measurement. The best way of assuring this is to measure both cross sections simultaneously using the same flux. Since this experiment will employ the same silicon detectors for all particle detection we also need to place suitable targets for both the fission and the elastic scattering in the chamber centre. We intend to construct a stacked target consisting of three separate targets. A polyethylene target in the middle and $^{235}\text{U}/^{238}\text{U}$ on each side of the polyethylene (see Fig. 5.3). Each target will have a diameter of 2.5 cm. The idea is that the deep penetrating protons produced in the mid-segment will escape the target assembly with only minor energy losses.

If all layers of the target are made modular, one could put together any mix of two outer fission layers and different thicknesses of the centre polyethylene layers (or none at all). The fission target will have thin backings so that both fragments can be detected if no polyethylene is in use. Considering the expected neutron flux, target diameter and the solid angle covered by the silicon detectors, a fission count rate of at least 1 kHz per μm of fissionable target thickness is anticipated.

5.2.3 Neutron energy

The energy of an incoming neutron will be determined using the time elapsed between the arrival of the primary beam bunch at the production target and the detection of the first reaction product. This detected time t_{det} is a sum of the neutron ToF t_n and the ToF of the charged secondary particle between the target and the detection point t_p . That is,

$$t_{\text{det}} = t_n + t_p. \quad (5.2)$$

From the information we get when detecting the secondary particle we must be able to deduce the neutron ToF with low uncertainty, in order to allow for accurate measurements. As long as the secondary particle species is known, as in the recoil proton case, determining the neutron energy from the ToF is straight forward. However, when a FP is measured in one of the silicon detectors, only time and energy information is available. To deduce a ToF for the detected FP one would need more information, e.g. like the fragment mass or a second time signal, in order to deduce the FP velocity. This is the reason we are upgrading our setup with PPACs.

PPACs are thin enough to allow FP to be transmitted through them (although with some energy losses) and later be detected in the silicon detectors as well. The heavy ions are moving so slowly that even though the PPACs are placed within a centimetre of the target, a correction for the flight time between target and PPAC needs to be performed. Since the FP speed between the PPAC and

the silicon detector is obtained, an approximate correction can be made by estimating the energy losses before detection in the silicon detector. Ideally, the PPAC is placed very close to the target.

5.2.4 Particle identification

Since an α -particle background from the uranium target is expected (both neutron-induced and due to natural decay), one needs to clearly separate these events from fission events. Even though the FPs are much heavier than α -particles, some overlap between the FP and α -particle distributions was expected in the energy spectrum from the PPACs [70] (but in section 5.4 we will see that this was not the case). If needed, the separation was supposed to be assisted by information from the silicon detectors in the overlap region.

A 50 μm silicon detector will fully stop α -particles of up to about 8 MeV (the α -particle punch-through energy). Any transmitted α -particles will deposit less than 8 MeV in the detector due to the decrease in stopping power with energy. The FPs, on the other hand, will always be fully stopped in the silicon detector and deposit their full energy. An α -particle discrimination is thus possible by interpreting all particles depositing more than 8 MeV as FPs. For such a scheme to work, it would be imperative that the FPs do not lose too much energy before they reach, and are fully stopped in, the detector telescopes.

All particles, penetrating at least the front silicon detector, can be identified by the ΔE - ΔE - E technique (see section 3.4). The recoil protons from elastic scattering will not only be identified by the kinematical relationship between energy and angle, but also through a distinct proton fingerprint in form of the energy depositions in the different telescope detectors.

In addition to simulating the $^{235}\text{U}(\text{n},\text{f})$ versus $^{238}\text{U}(\text{n},\text{f})$ versus $\text{H}(\text{n},\text{n})$ measurement, the same simulation software was used to simulate LCP on various targets, e.g. Si. As an example of the ΔE - ΔE - E technique, the plot in Fig. 5.4 shows simulated ΔE - ΔE events. In this plot, the proton, deuteron and triton distributions bend backwards as the particle energies exceed the particle-specific punch-through energy of the second detector (in this case, 500 μm thick). By having three detectors in the telescope, these higher energy events can still be separated using the information from the last detector.

5.2.5 Observables

While the angular integrated fission cross sections of ^{238}U and ^{235}U measured relative to the $\text{H}(\text{n},\text{n})$ cross section, as well as against each other, are the main expected outcomes of this experiment, additional observables can be extracted. Each fission cross section is in fact measured at several different angles. In order to integrate these data points into the angular integrated cross section, one must interpolate and extrapolate into the angular region not

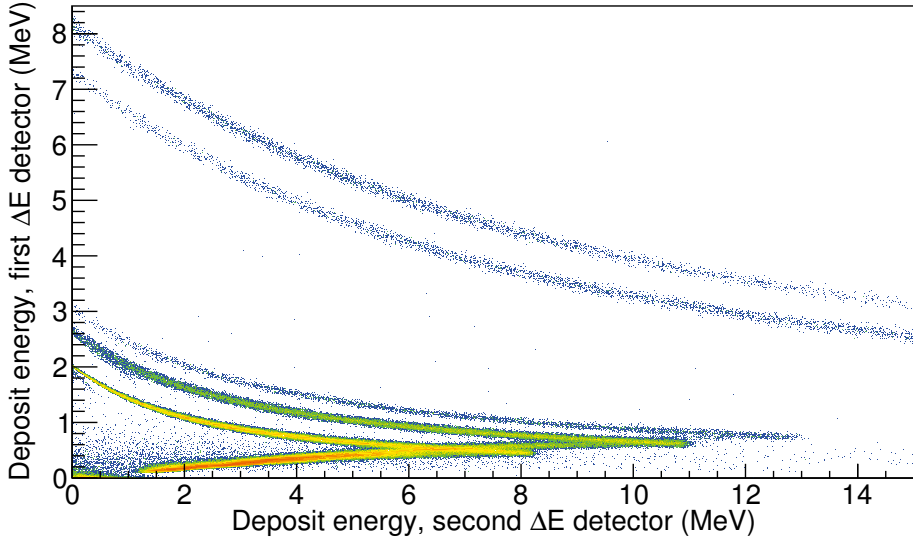


Figure 5.4. Simulated ΔE - ΔE data showing neutron induced light-ion production from a silicon target. From top to bottom the distributions of α -particles, ^3He , tritons, deuterons and protons are clearly distinguishable. The proton, deuteron and triton distributions bend backward at the punch-through energy (see text for further details).

covered by measurements. Previous studies concluded that the FFAD can be well described by a Legendre polynomial of degree four or higher [31].

The deduced FFAD becomes a by-product that in itself is interesting. During the analysis stage of our measurement we will need the FFAD for each neutron energy. Therefore, we will provide FFADs for the whole energy range, 1 to 40 MeV. The Medley setup might be able to distinguish light from heavy fragments, on a coarse grained scale, thus the different FFADs for symmetric and asymmetric fission, might also be obtained. The errors associated with the estimating the Legendre polynomials with a limited number of data points have been estimated using pseudo-data [68]. Utilising the Medley setup's ability to rotate all the detectors, e.g. 10° , and thereby double the number of data points proved beneficial even though the statistics for each point would be halved.

5.3 Simulations

As it was clear that the new experimental conditions at the NFS facility would require an upgrade of our setup, I simulated the setup in order to try to identify possible problems and limitations, before the setup was adapted for the new conditions. It was of great concern to investigate how the inclusion of PPACs in the setup would affect the experiment in terms of detector efficiency and neutron-energy resolution. The PPACs not only interact with the particles going through them, but they also force us to fill the whole chamber with

gas so that we would not have a pressure difference between the inside and outside of the PPAC. Light particles lose little energy in the low pressure gas but heavy ions like FPs lose a substantial part of their energy. The simulations gave us estimates on what resolutions to expect and to aim for when it comes to the development of the PPACs. The simulations have also put some limits on the target thickness and the performance of the silicon detectors as well as providing estimated uncertainties for, e.g. the neutron energy.

5.3.1 Simulation setup

The simulations were conducted using a program written based on the simulation toolkit library Geant4 [71] version 9.6.2. The geometry of the chamber and detectors were implemented, but to a certain degree simplified. The neutron source was also simplified mainly because little information of its characteristics was available. The standard physics list 'QGSP_BIC_HP' [72] was used but with some modifications. The modifications of default Geant4 behaviour are described in more detail in appendix A.1.

The primary particles in the simulations are neutrons, created randomly on a circular surface (representing the neutron production target) of radius 1.5 cm and directed towards the Medley chamber entrance window 5 m away. The neutron energies could be fixed to a constant value, sampled from a uniform distribution from 0 to 40 MeV, or sampled from the anticipated flux from the d+Be neutron production option at NFS [39, 40].

5.3.2 Simulation results

One of the main results of the simulation study was the estimated neutron energy resolution. Several factors come into play determining the neutron energy resolution. The most important factors are the time resolution of the detectors and how corrections to the neutron ToF are made. Factors like beam characteristics are not under our control and thus set a non-mutable limit on the possible achievable resolution.

Since the rise time of a silicon detector signal is typically about 10 ns [34] and we intend to use digital sampling of the signal, we argue that it is reasonable to assume that we can get a time resolution of 1 ns or better for the silicon detectors. PPACs have in previous studies proven their excellent timing properties [73] and for us to achieve at least a resolution of 0.5 ns seems plausible. The time structure of the primary accelerated deuteron beam is expected to have a FWHM of about 0.8 ns when using a buncher.

I tested the individual contributions to the neutron energy resolution coming from the beam temporal structure, PPAC timing resolution, and the silicon detector timing resolution, respectively. From fig. 5.5 one clearly sees that the PPAC time resolution gives the most important contribution, and the second

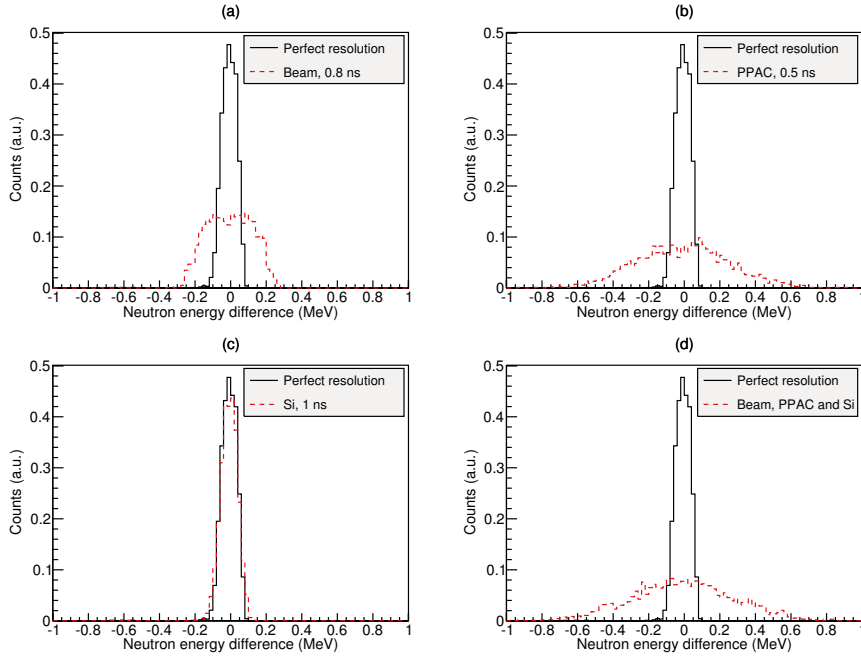


Figure 5.5. Contributions to the neutron energy resolution. In all panels, ‘perfect’ resolution means that neither detector resolutions nor the temporal structure of the beam were simulated, but resolution due to geometry or scattering still apply. In panel (a) one observes the effect of the beam structure, in (b) the effect of a PPAC timing resolution of 0.5 ns, and in (c) the effect of a 1 ns timing resolution in the silicon detector. In (d) all the effect are applied together.

most important contribution is due to the beam time structure. This means that we have good reasons to put much effort into improving the PPAC time resolution as much as possible during our detector development.

The total resolution of the neutron energy is energy dependent but even for the worst case scenario, i.e. high neutron energy, we expect a resolution better than 2 % for FPs and better than 4 % for the recoil protons. In fig. 5.6 the expected uncertainty in neutron energy is depicted as a function of incoming energy. The slightly worse resolution for the recoil protons is due to the fact that the PPACs cannot reliably detect deeply penetrating particles as protons, so we must rely on the timing properties of the silicon detectors. How these energy resolutions translate into equivalent cross-section uncertainties depend on the shape of the cross sections at the energy in question.

Another pressing issue was how the target and Mylar foil thickness as well as the gas pressure affect the performance of the experimental setup. Even though the pressure will be in the order of a few mbar, it will be enough to make FPs lose several MeVs of kinetic energy as they pass the gas-filled chamber space. It is imperative, that one out of the two FPs for each fission is detectable if it is

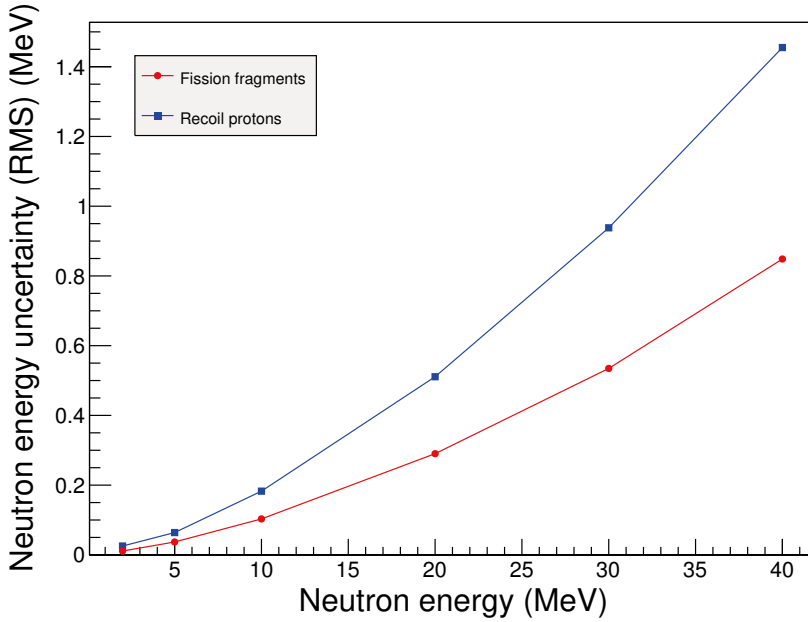


Figure 5.6. Expected uncertainty in the incoming neutron energy as a function of the incoming energy. A generally higher uncertainty is expected from proton events, since the PPACs will not detect these highly penetrative particles.

emitted in an angle covered by one of our detectors. Our setup must allow for the low energetic heavy FPs to escape the target, penetrate both PPAC windows and travel through the chamber gas, before being detected in a silicon detector. This must happen while making sure that the FPs deposits enough energy in one of the silicon detectors, that they can clearly be distinguished from eventual α -particles, i.e., exceeding 8 MeV.

It will be beneficial if we produce aluminised Mylar foils (or find a commercial product) with a thickness of less than 1 μm . It was soon clear that unless the Mylar foils are kept as thin as possible we would lose FPs in them and thus not be able to reach a detection efficiency close to 100 % (it is also preferred due to the lesser amount of additional scattering centres in the beam). With the Mylar foil thickness fixed at 1 μm , two accessible variables for controlling the energy loss of the FPs remained; the fissionable target layer thickness and the gas pressure. The optimal gas pressure for the PPAC operation was not known at the time the simulations were performed. Based on discussions with and the work of other groups using similar PPACs, e.g., Ref. [74], we assumed a suitable pressure to be about 3 mbar.

Not surprisingly I found that, while keeping the chamber pressure at 3 mbar, a 1 μm thick target allowed detection of FPs with higher deposited energy in the silicon detector than for a 2 μm thick one. However, a thinner target means

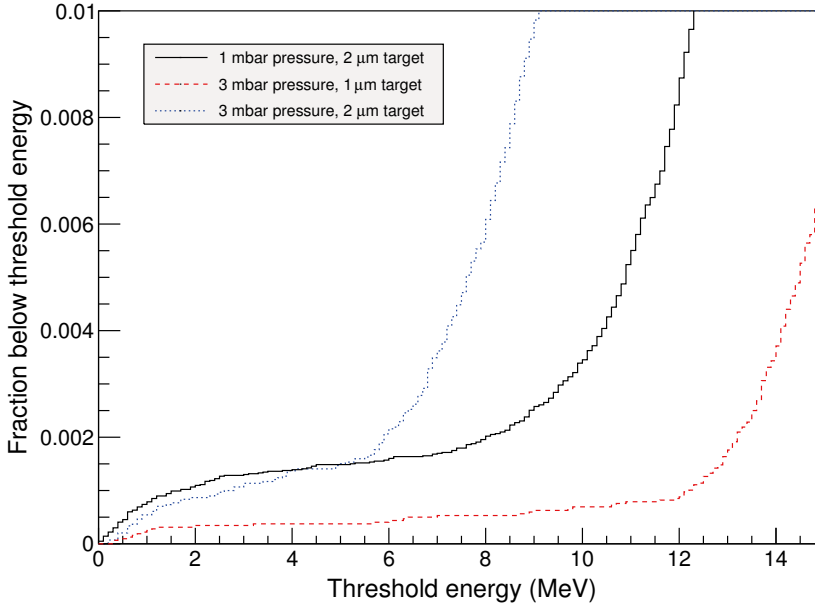


Figure 5.7. The fraction of FPs that reach the front silicon detector with energy lower than the threshold is indicated on the x -axis. Most of the fragment's kinetic energy is lost while escaping the target and penetrating the PPAC foils as well as traversing the gas towards the detector telescopes. The PPAC foil thickness is kept at $1\text{ }\mu\text{m}$. If the gas pressure is kept at 1 mbar and the target is $2\text{ }\mu\text{m}$ thick, about 99.8 % of the FPs are detected with energies higher than 8 MeV. To detect more FPs above the α -punch-through energy, the target thickness can be decreased to $1\text{ }\mu\text{m}$ allowing almost every FP to reach the silicon detector with a kinetic energy above 8 MeV.

lower count rate. If a lower gas pressure of 1 mbar is used the $2\text{ }\mu\text{m}$ thick target might still be an option, letting us detect FPs with at least 8 MeV in the silicon detector. The option of 3 mbar gas pressure and a $2\text{ }\mu\text{m}$ thick target would theoretically deny us the possibility to distinguish FP from α -particles by the pulse height in the silicon detector alone. The fraction of FP detected in the silicon detector, above a certain threshold energy, is depicted in Fig. 5.7.

Considering PPAC windows of $1\text{ }\mu\text{m}$ one can estimate the additional scattering centres for elastic scattering. Since we will measure the elastic scattering from the polyethylene target, any extra hydrogen atoms in the beam must be corrected for. Depending on the final design of the PPACs and the relative thicknesses of the Mylar foils as well as of the polyethylene target, this correction will be in the order of a few percent. It will be based on simulations together with empty target runs.

5.4 Current status

The simulations and the analysis of them were performed mainly during 2013. Since then, PPACs have been built and tested in our laboratory in Uppsala using a californium source. It turns out that with a 3 mbar gas pressure the PPACs are essentially blind to α -particles but could still achieve a 100 % efficiency for FP detection (within experimental uncertainties) [68]. However, using the latest prototype PPAC a near 100 % α -particle-efficiency was achieved at 7 mbar. The final gas pressure and PPAC design will determine whether distinguishing FPs from α -particles will be problematic or not.

The specifications of the uranium targets are better known. In the simulations the uranium targets were modelled as uranium oxide but the real targets will most likely be uranium tetra fluoride. They will also be thinner, in the order of 0.5 μm , than the ones modelled in the simulations. All of these things play in our favour, increasing the margins for a working setup. The Mylar thickness is now slightly less critical, but the energy losses must still be kept low. PPACs with window thicknesses of 2.5 μm were tested first, but now PPACs with 0.9 μm windows have been produced and are currently being evaluated.

The simulations have helped the discussion and development of the experiment, but the situation is now changed. We have learned more and have a better picture of the experiment we are planning. New simulations are planned which calls for the simulation software to be updated and improved in order to take into account the current situation and the new information available. The measurements made using a ^{252}Cf source with prototype PPACs (see fig. 3.3) [68] can now be compared to simulations. The work of updating the simulations is in the writing moment in progress. Due to the many delays of the NFS facility, no experiments have yet been performed. Measurements of light-ion production is planned as soon as the neutron facility becomes operational and commissioning will start.

6. Alpha-particle and triton production at GELINA

*Light my candles in a daze,
'cause I've found god.*

— Kurt Cobain

The measurement of ${}^6\text{Li}(n,\alpha)t$ at GELINA is one out of three related experiments conducted at the JRC-Geel. Detector setups similar to the one presented in this thesis have been used to measure ${}^{10}\text{B}(n,\alpha){}^7\text{Li}$, also at the GELINA facility, and a measurement of the ${}^6\text{Li}(n,\alpha)t$ cross section has been conducted at the VdG facility [75]. The ${}^6\text{Li}(n,\alpha)t$ measurement at the VdG used a ${}^6\text{Li}$ target with a thin aluminium backing and a pressure of 3.5 bar enabling both reaction products to be detected. This is contrary to what is being used to measure the ${}^6\text{Li}(n,\alpha)t$ cross section at the GELINA facility where thick (0.5 mm) backings are used and two ${}^6\text{Li}$ targets are employed in a back-to-back position.

Three different measurement runs for ${}^6\text{Li}(n,\alpha)t$ have been conducted at the GELINA facility, each improving on the previous one. After presenting how come we measure ${}^6\text{Li}(n,\alpha)t$ and the setup of the original experiment, each of the iterations will be subsequently discussed in order to explain how the experimental setup has evolved. The concluding section 6.5 will discuss further improvements that can be made if another iteration of the experiment is realised.

The results from this first part of the ${}^6\text{Li}(n,\alpha)t$ measurement has previously been reported in my licentiate thesis [5] as well as presented at the CNR*15 conference [76]. The section about the general description of the experiment and the section about the first measurement consists to a large degree of reworked text from my licentiate thesis [5]. Preliminary results for the third measurement has partly been presented at the ND2016 conference [77] but the analysis has since then been revamped and the final results are presented here in section 6.4.

6.1 Motivation

As discussed in section 2.1 there are many properties sought for in a good neutron standard cross section. The ${}^6\text{Li}(n,\alpha)t$ reaction is a suitable standard in many situations due to its high cross section and high Q -value of almost

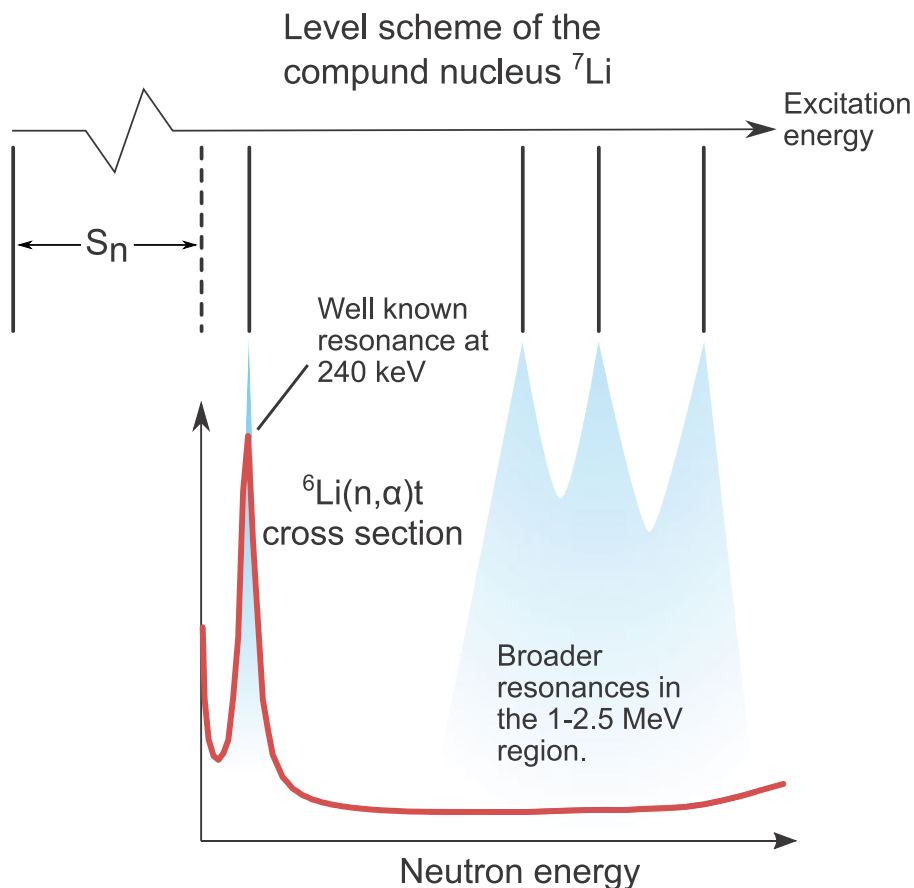


Figure 6.1. The levels of the compound nucleus ${}^7\text{Li}$ dominates the structure of the ${}^6\text{Li}(n,\alpha)t$ cross section. But to what degree it is affected by the three broad levels above 1 MeV is disputed.

5 MeV. The high energies of the reaction products give large clear signals in many detector systems. Either the triton, the α -particle or both particles can be detected, but usually it is easier to detect the less penetrating α -particles.

The first resonance of ${}^6\text{Li}(n,\alpha)t$ occurs at a neutron energy of 0.240 MeV in the laboratory frame of reference. It corresponds to the $\frac{5}{2}^-$ excited state at 7.454 MeV in the compound nucleus [78].

Up to 1 MeV the cross section from different experiments agree fairly well, but above 1 MeV to about 2.5 MeV discrepancies exist. In this region three other levels in the compound nucleus contribute to resonances in the ${}^6\text{Li}(n,\alpha)t$ reaction. However, their widths are much larger (4.71, 2.75 and 4.37 MeV, respectively, compared to 0.080 MeV for the 7.454 MeV level) [78] and, therefore, the resonance structure is more smeared out. The situation is illustrated in fig. 6.1.

In the 1 to 2.5 MeV region at least two independent experiments have reported discrepancies. One experiment was performed using an ionisation chamber similar to the one used at JRC-Geel (see section 3.1) [79], while the second one employed solid state detectors [80]. Both experiments see a several percent higher cross section than, e.g., the ENDF/B-VII evaluation [81] in this energy region.

It is speculated [82] that one of the reasons the evaluation based on previous measurements shows a smaller cross section is the *particle leaking* effect. Due to the incoming neutron momentum there is a possibility of both products (t and α) being emitted in the forward direction (in the laboratory frame of reference), but with large polar angles ($0^\circ < \theta < 90^\circ$) for moderate neutron energies. In this case the detector response will look like as if only one particle, with the combined energy of both the triton and the α -particle, has entered the chamber. If this effect is overlooked it can lead to an underestimation of the cross section since the pulse height is much higher than for a normal α -particle event and might be discarded because of that. This is why the effect is called *particle leaking*.

The aim of the study is to allow for an extension of the standard energy range from 1 MeV to a few MeV. Therefore, any discrepancies in this region must be resolved before the cross section can be trusted as a standard. An attempt to do this has been carried out by measuring the α -particles (and later also the tritons) from the ${}^6\text{Li}(n,\alpha)t$ reaction as well as the fission products from the ${}^{235}\text{U}(n,f)$ reference reaction.

6.2 First experiment

Data collection for the first iteration of this experiment started in spring 2015.

6.2.1 Experimental setup

The original experimental setup was situated at GELINA viewing the neutron production target unmoderated from a distance of 60 m.

A schematic view of our GIC is depicted in fig. 6.2. This kind of detector was described in more detail in section 3.1. Contrary to most setups this chamber contained two cathodes, one for the lithium target and one for the uranium target. The cylindrical chamber has one shared gas volume kept at a pressure slightly above 1 bar (the gas used was P-10), but the uranium measurement is confined to the front compartment of the chamber and the lithium measurement to the back. Each compartment has a cathode in its centre and the uranium and lithium targets, respectively, are placed on each side of the cathode so that each pair of targets share the same cathode. In the case of the two uranium targets, a small 1.5 mm spacer was inserted between the targets, but electrical contact was still maintained.

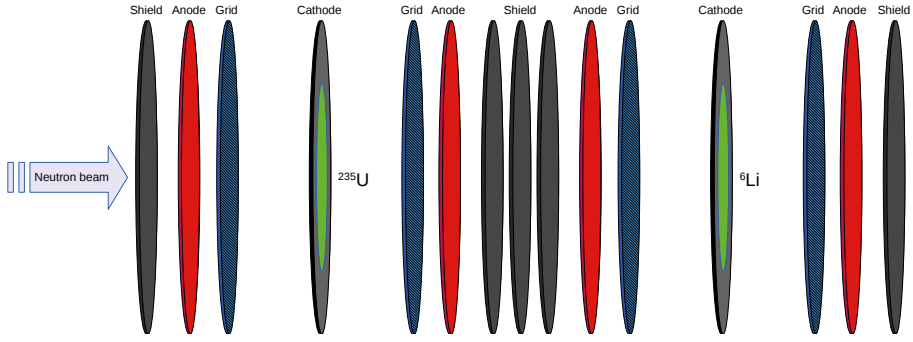


Figure 6.2. Schematic of the ionisation chamber used for the first and second experimental runs. The chamber axis coincides with the neutron beam axis. Each cathode consists of two targets facing forwards respectively backwards. In total the chamber has 10 independent electrodes, five in each compartment separated by shields. The shields are interconnected and kept at the same potential.

Both lithium targets consisted of LiF, which was vacuum deposited on a aluminium backing and the deposited layers had similar masses, 2014(23) and 2610(40) μg , respectively. Both deposits had a diameter of 8 cm and a 0.5 mm thick backing, making it impossible for any reaction products to traverse the target to the other side of the cathode (the range of a 5 MeV triton in aluminium is only about 100 μm [83]). The uranium targets were of similar areal densities, 193 and 222 $\mu\text{g}/\text{cm}^2$, but due to different diameters (4.5 cm and 7 cm, respectively) they had different masses, 3071(46) and 8520(40) μg ^{235}U , respectively. The isotopic mass ratio of ^{235}U in the uranium target material were 97.663(3) and 99.9336(14) % for the two targets, respectively.

On each side of each cathode, the chamber was equipped with an anode and a grid. The induced signals on each electrode were recorded by a 100 MHz digitiser, with 12 bits resolution. Signals from all electrodes were captured rather than only from the cathodes and anodes, in order to reduce uncertainties due to electronic drift [27]. In this experiment the grids consist of conductive meshes (rather than parallel wires, which is another option).

6.2.2 Analysis procedure

This section will go through how to determine the neutron energy from the ToF, how to extract the necessary information from the electrode signals, as well as how the full dataset is analysed.

6.2.2.1 Trace analysis

The digital sampling of the waveforms enables corrections in the post-analysis and has shown to be superior to analogue equipment [27]. The collection of stored waveforms needs to be iterated in order to extract the relevant informa-

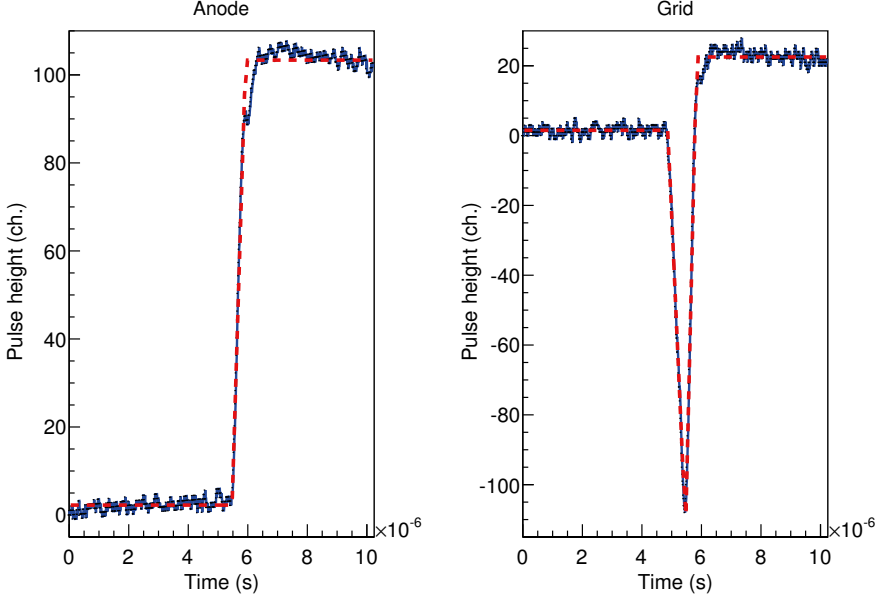


Figure 6.3. An example of anode (left) and grid (right) signals from an α -event. The dashed lines represent the fits made to the signals (the anode fit function is given in eq. 6.1).

tion. The parameters that are of interest, are in this case the time and the signal PH. Typical signal shapes are shown in fig. 3.2. The cathode and anode signals were fitted by

$$f_{C/A}(t) = \begin{cases} t < t_{\text{centre}} - \frac{t_{\text{width}}}{2} : & a_0 \\ t > t_{\text{centre}} + \frac{t_{\text{width}}}{2} : & a_1 \\ \text{else} : & \frac{a_0 + a_1}{2} + \frac{a_1 - a_0}{t_{\text{width}}} (t - t_{\text{centre}}), \end{cases} \quad (6.1)$$

where a_0 and a_1 are the constant signal levels before and after the signal respectively, t_{width} is the rise time and t_{centre} is the centre of the pulse rise. That is, the signal is fitted to three connected line segments. Similarly the grid signals are fitted to a function describing four connected line segments (six parameters). The anode and grid signals from an α -particle event are depicted in fig. 6.3 together with the corresponding fitted functions. The choice of fit function represents a compromise between the number of needed parameters, computation complexity and how well the function captures the signal features. The signal PH is derived, for all three electrode signals, by taking the difference between the signal level before and after the signal (a_0 and a_1 in eq. 6.1 for the cathode and anode).

By fitting the signals rather than just extracting the PH, more information become available, e.g. the signals' rise time. The deduced PHs from the

fitted signals were compared to the PHs obtained by applying a noise reducing $CR-RC^4$ filter and then extracting the PH. No preference for either method could be seen. The χ^2 -distribution from the fit results corresponded to the expected distribution considering the number of degrees of freedom as well as the uncertainty (noise) of the baseline.

6.2.2.2 Time-of-flight

The trigger to the digitisers was created by letting each cathode signal go through pre-amplifier followed by a *Constant Fraction Discriminator* (CFD) and then adding them by a logical OR operation. The resulting signal was then combined by a logical AND operation with a signal from the controlling computer indicating whether the acquisition system is ready or not. The event time t_e , recorded for each event, is the time difference between this trigger and the accelerator signal arriving with each beam bunch. This timing can be turned into the ToF t_{ToF} , if a reference time t_0 is known.

For calibration purposes bismuth and lead plates, with a total thickness of 35 mm and 15 mm respectively, were placed in the neutron beam in front of the chamber during the measurements, in order for resonances to be visible in the ToF spectrum. Neutrons with energies close to the resonances have a higher probability of being absorbed before they reach the measurement chamber and therefore negative peaks (a decrease of events) appear in the ToF spectrum at predictable energies. If either the corresponding nuclear levels (see section 2.2 for details) or the resonances themselves have been measured before, they can be used as calibration points.

Except at energies below about a meV and at the resonance energies, the total neutron cross section of lead and bismuth is in the order of 10 b or lower [81]. This roughly corresponds to a neutron attenuation coefficient of less than $0.03 \text{ cm}^2/\text{g}$. Compared to the attenuation coefficient for 5 MeV γ 's [84] the neutron dito is significantly smaller, but in the same order of magnitude. The γ -attenuation decreases with γ -energy, so it is clear that these plates will attenuate low energetic γ -flux much more than the neutron flux. Therefore a lower γ -background is achieved, at the expense of some neutron flux.

Unfortunately, even though previous experiments have used the same technique [85, Fig. 1] and some resonances from the inserted beam filters were visible, the resonances could not be unambiguously identified. Instead, the γ -flash coming from the neutron production target was used to determine the reference time t_0 . The peak in the ToF spectrum formed by γ -events, was clearly separated from the events induced by slower particles. Since the speed of light is known,

$$t_{\text{ToF}} = t_e - t_0 + L/c, \quad (6.2)$$

where L is the distance between the neutron production target and the relevant cathode. Once the neutron ToF is deduced the kinetic energy of the neutron

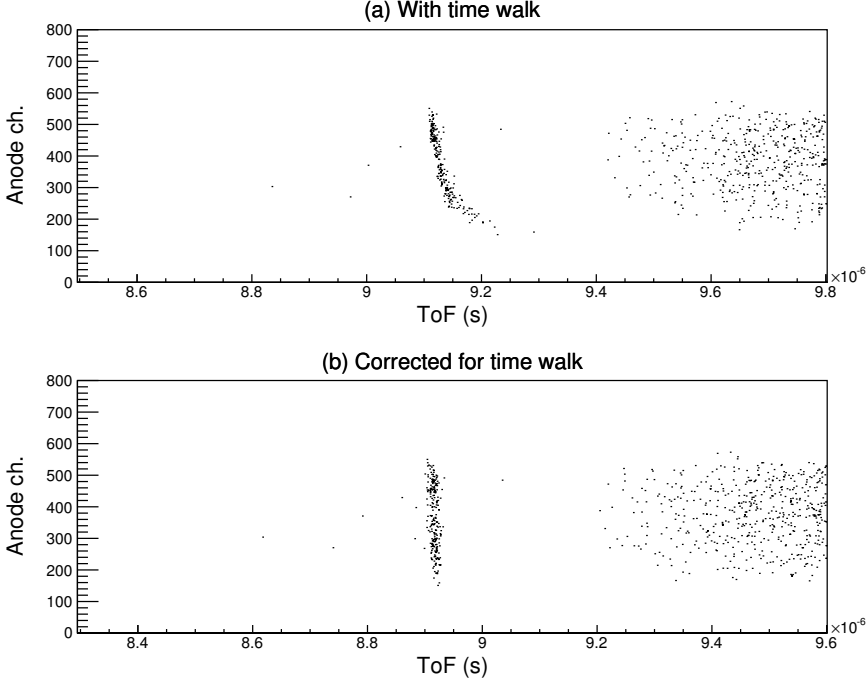


Figure 6.4. The top panel (a) shows the ToF plotted against the forward uranium anode PH, before the correction of the PH dependence (walk) of the timestamp. The bottom panel (b) shows the same plot but after the correction.

T_n , is given by:

$$T_n = m_n (\gamma - 1) = \frac{m_n}{\sqrt{1 - \frac{L^2}{t_{\text{ToF}}^2 c^2}}} - m_n, \quad (6.3)$$

where $m_n = 939.565\,379\,\text{MeV}$ is the neutron mass.

However, when the ToF spectrum was analysed we discovered that the γ -flash events did not end up with the same ToF (see fig. 6.4). The output of the CFD modules still depended on the size of the signal (walk), which had to be corrected for. Since all signals were digitised I could extrapolate the slope of the cathode signal to the baseline and correct the timestamp by the time difference between the extrapolated time, t_{extrapol} , and the time corresponding to the digitiser being triggered, t_{trigger} . Thus the corrected ToF was calculated by:

$$t_{\text{ToF}}^{\text{corr}} = t_{\text{ToF}} - (t_{\text{trigger}} - t_{\text{extrapol}}). \quad (6.4)$$

6.2.2.3 Fission events

Due to the much larger energy deposited in the gas by FPs, compared to other possible reaction products, it is fairly easy to distinguish them. A PH threshold

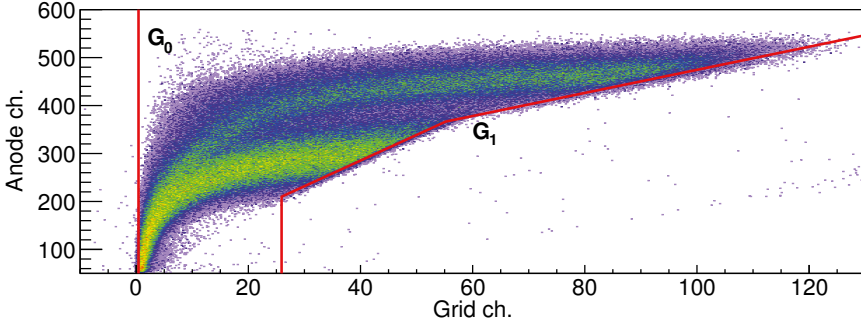


Figure 6.5. The anode PH plotted as a function of the anode PH, for all fission events in the forward direction. The lines represent the limits where the distribution height drops to half its maximum and defines $\cos \theta = 0$ and $\cos \theta = 1$.

separated the FPs unambiguously from the e.g. α -particles from the sample activity that were also present in the data. Due to the target and backing thickness, only one of the two FPs is detected for each fission event. The mass of the FP is, for each single event, unknown and can only be estimated based on its energy. The neutron energy does not reach more than a few MeV, so its influence on the fragment kinematics will be small. Due to this, all fission events emerging from the same side of the fission target are analysed together. In order to get the numbers of events in a specific neutron energy interval, an appropriate cut is applied later.

The analysis starts by plotting the anode signal PH versus the grid signal PH as in fig. 6.5. For each anode channel, corresponding to the detected energy, the fission events are projected onto the grid axis. The projection is used to determine for which grid values the distribution drops to half its maximum. These grid values, G_0 and G_1 , correspond to $\cos \theta = 0$ and $\cos \theta = 1$ (or $\cos \theta = -1$ for particles emerging from the backwards facing target). We then return to eq. 3.6 and remember that the grid PH is proportional to $\cos \theta$, allowing us to express $\cos \theta$ as a function of the detected grid PH $G(Q_G)$:

$$|\cos \theta| = \frac{G(Q_G) - G_0}{G_1 - G_0}. \quad (6.5)$$

The value of G_0 is very close to zero since the FP emitted in the target plane should not leave a net induced charge on the grid according to eq. 3.6. The value of G_1 will change with the fragment energy since it incorporates \bar{X} which in turn depends on the stopping range of the heavy ion in question. It turns out that G_1 can be well parametrised by two line segments as shown in fig. 6.5.

The fragments emitted in an angle close to 90° will suffer from larger energy losses in the target since the effective thickness of the target is proportional to $\frac{1}{\cos \theta}$. Corrections for the energy losses in the target can be made by observing the mean energy of all events for a certain cosine value. The inverse cosine is plotted against the anode PH, denoted A , and a straight line, $A = \frac{k}{|\cos \theta|} + m$,

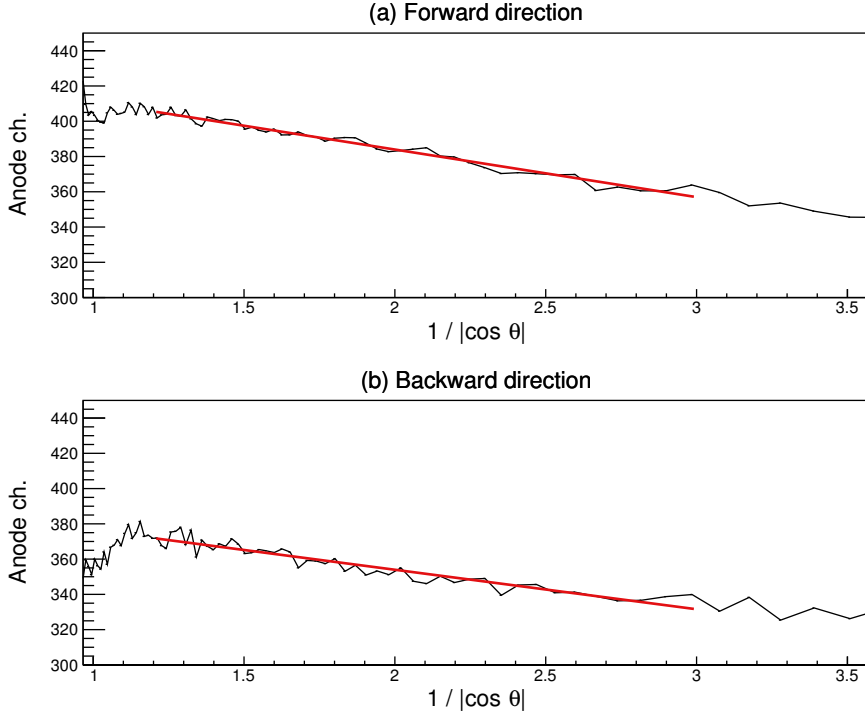


Figure 6.6. Mean anode PH plotted as a function of the inverse of the cosine value, for the fission events in both forward (a) and backward (b) direction. The fitted lines are used to correct for the angular dependent energy loss in the fission targets.

is fitted to the data where the losses are not too big ($1.25 < \frac{1}{\cos \theta} < 3$, see fig. 6.6). We can estimate the anode PH, in the absence of energy loss in the target, with

$$A_{\text{no loss}} = A(\theta) - \frac{k}{|\cos \theta|}, \quad (6.6)$$

through extrapolation of the fitted line by letting $\frac{1}{\cos \theta} \rightarrow 0$. For gracing angles the energy losses are too big to be well corrected for and some particle losses are unavoidable. For the final analysis only the events where $|\cos \theta| > 0.3$ are used. The anode PH can be roughly translated into energy by calibrating the anode spectrum using the two distinct humps of light and heavy fragments, respectively.

6.2.2.4 α -particle events

The two reaction products (^4He and ^3H) are in this case of comparable masses to the neutron's, which means that the kinematics are strongly dependent on both the neutron energy and the emission angles in the laboratory frame of reference. In the limiting case of an incoming neutron with negligible energy,

the angular distribution is isotropic and the α -particle and triton energies will be determined only by the reaction's Q -value together with the conservation of energy and momentum. In other words, the laboratory and the CoM frame are, in this case, identical.

For higher neutron energies difficulties arise. The two products will no longer be emitted in opposite directions in the laboratory frame, due to the momentum transfer of the incoming neutron. The *particle leaking* has already been discussed in section 6.1. The particle energy is the largest at small angles, where it is also increasing with neutron energy. For backwards particle emission the neutron momentum (q_n) transfer will decrease the particle energies but at the same time the neutron energy ($\propto q_n^2$), will increase the available reaction energy. These two opposing effects lead to a non-monotonic behaviour of the backwards emitted particle energies.

At this pressure of 1 bar, the tritons are not fully stopped in the chamber for small angles. Therefore, only the α -particles are of interest for this analysis. When the grid PH is plotted against the anode PH, the α -particle distribution can be recognised as a fairly straight 'banana' shape (see fig. 6.7). The distribution will move with neutron energy and the bent shape originates from both the reaction kinematics as well as energy losses in the target. An increased neutron energy will, for all forward angles, give rise to an increased particle energy, leading to an increased anode PH. The energy losses in the target will also change when the particle energy increases and therefore will the shape of the distribution also change. The relevant distribution was selected using manual cuts for several neutron energies. These cuts were parametrised so that the relevant events, of arbitrary neutron energies, could be selected. The tritons that are stopped, are seen as a fairly horizontal distribution. Much of the background can be attributed to partly stopped tritons.

The particle energy can be determined both by calibrating the anode PHs, as well as by kinematic calculations based on the neutron energy derived from the ToF. The angles can be determined in a similar fashion as described for the fission events. However, since in this case the neutron energy greatly affects the kinematics, the PH limits, G_0 and G_1 , in eq. 6.5 must be determined independently for each small energy interval of interest.

The energy loss in the target does not scale linearly with particle energy but is generally small, except for gracing angles. An crude energy calibration of the anodes can be performed by observing the events at the end points of the grid PH distribution. Since these corresponds to events of gracing angles or events along the chamber axis, respectively, the corresponding laboratory energies are known. The anode PH of these events were used to create two separate energy calibrations, $f_0^{\text{cal}}(A)$ and $f_{\pm 1}^{\text{cal}}(A)$, each valid only for $\cos \theta = 0$ and $\cos \theta = \pm 1$, respectively. The laboratory energy could then be estimated for each event by interpolation between the two endpoint calibrations.

$$E_{\text{lab}} = f_{\pm 1}^{\text{cal}}(A) |\cos \theta| + f_0^{\text{cal}}(A)(1 - |\cos \theta|) \quad (6.7)$$

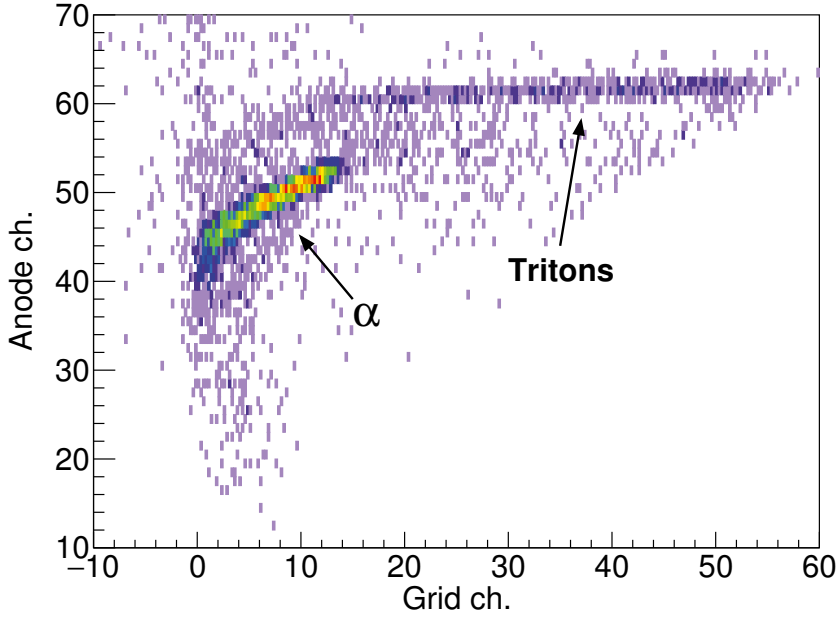


Figure 6.7. Events in the forward direction from the Li target. The neutron energy interval is 200–250 keV. The majority of the events are α -particles and are clustered in a bent shape. Since this shows the events in the laboratory frame of reference the α -particle distribution is bent due to both the frame boost and to energy losses in the target.

Once the laboratory properties of the α -particle are known they can be transformed into the CoM frame by Lorentz transformation and energy and momentum conservation. One finds that

$$T'_\alpha = \gamma \left(E_\alpha - v \cos \theta \sqrt{E_\alpha^2 - m_\alpha^2} \right) - m_\alpha \quad (6.8)$$

$$\cos \theta' = \pm \sqrt{1 - \frac{E_\alpha}{E'_\alpha} (1 - \cos^2 \theta)}, \quad (6.9)$$

where E denotes total relativistic energy, T denotes kinetic energy, m denotes mass, v denotes velocity (in terms of c), and all CoM properties are primed. The negative solution in eq. 6.9 is applied for the backwards facing side while the positive is applied for the forwards facing side. In addition $\cos \theta'$ is multiplied by -1 if $\cos \theta_{\text{limit}} > \cos \theta$ where θ_{limit} is given by

$$\theta_{\text{limit}} = \arctan \sqrt{\frac{(m_n + m_{\text{Li}})^2}{m_n m_\alpha} \frac{m_t}{m_\alpha + m_t} \frac{E_n + Q}{E_n}}, \quad (6.10)$$

Table 6.1. Ratios between fission event properties associated with the forward and backward direction with respect to the beam. The detected counts and average linear energy loss in the targets are compared to the expected values based on the target specifications. The relative difference between the measured and expected values are also reported.

Property	Ratio (f/b)	Expected value	Relative difference
Event counts	2.741(14)	2.774(43)	1.2%
Energy loss	1.20	1.15	4.7%

in order to take into account that the forward laboratory angle might have reached into the back hemisphere of the CoM frame.

6.2.3 Results

6.2.3.1 Uranium counts and distributions

For FP of gracing angles, the effective thickness of the target becomes large. Consequently, the energy losses will be large too, making accurate corrections more difficult. Sometimes the fragments will not even escape the target. One can see that some losses of events are occurring in the cosine spectra in fig. 6.8.

To avoid being affected by particle losses, only the fission events where $|\cos \theta| > 0.3$ were used. By comparing the ratio of event counts in the forward and backward direction with the ratio of ^{235}U atoms in the corresponding targets, one can conclude that the relative number of detected events is very close to the expected (see table 6.1). Another check is to compare the energy loss (the slopes of the fitted lines in fig. 6.6, see eq. 6.6) with the target thicknesses. Taking into account that the gain of the two different anodes are similar but not identical, the agreement between the measured value and the expected is once again good (see table 6.1).

To be able to compare the anode distributions they were transformed into energy distributions by using the two peaks (corresponding to the low energy heavy fragments and the high energy light fragments, respectively) as calibration points. Depicted in fig. 6.9 are the two energy spectra from the forward and backward direction. They match each other well, but some small discrepancy can be seen at lower energies.

6.2.3.2 $^6\text{Li}(n,\alpha)t$ in the centre-of-momentum frame

For each identified α event the laboratory properties were determined using eq. 6.7 after deducing the angle from the grid PH. By subsequently using eqs. 6.8 and 6.9 a transformation into the CoM frame was performed. The result is a distribution close to constant in energy (see fig. 6.10). The spread of the distribution can be attributed to uncertainties in the neutron energy as well as in the particle angle. However, the deviation from the predicted

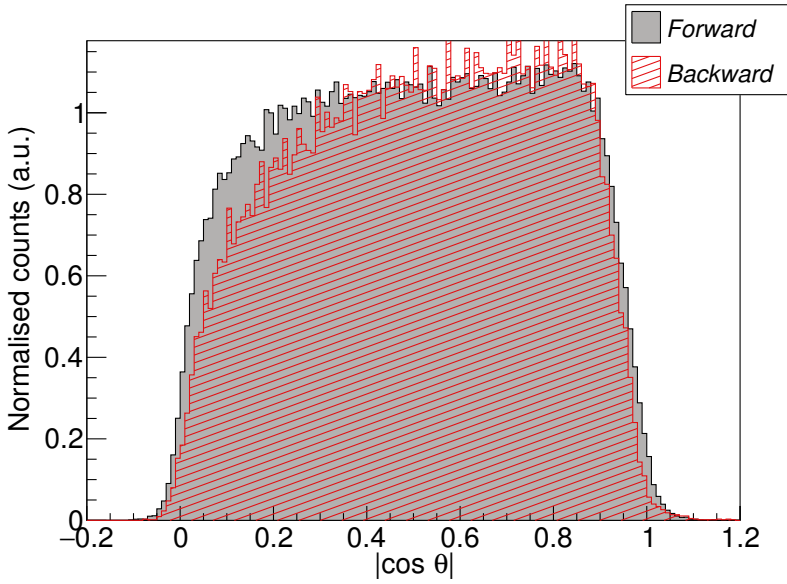


Figure 6.8. Cosine distributions of the events emerging from the forwards and backwards facing fission targets respectively. When $|\cos \theta| \lesssim 0.3$ the energy losses in the target becomes large and in the backward direction one clearly sees a loss of events due to this. The spectra have been normalised based on the events where $|\cos \theta| > 0.3$.

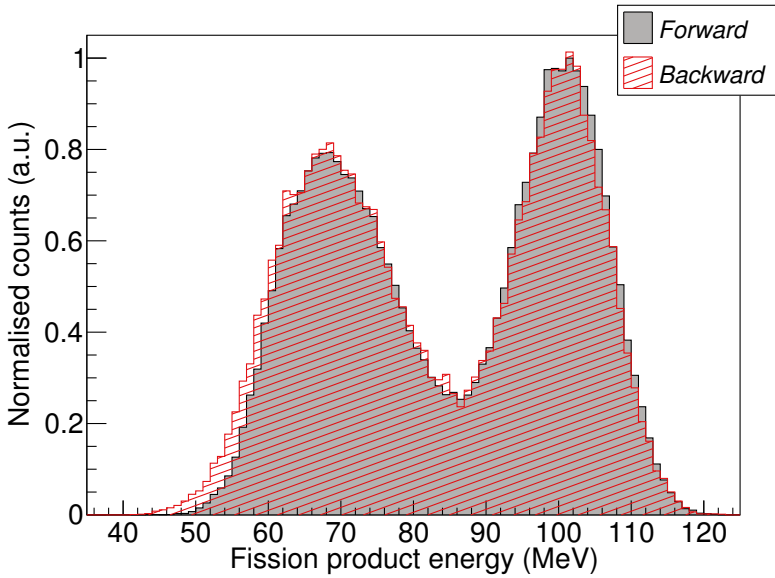


Figure 6.9. The peak positions are based on data of the thermal fission of ^{235}U . Both spectra were normalised according to the number of ^{235}U atoms in their respective targets.

linear behaviour is most likely an artefact of the big uncertainties in the energy calibration of the anodes. If one needs to calculate a precise α -particle energy, a more reliable way of determining it is to use the angle deduced from the grid PH together with the neutron energy.

6.2.3.3 Preliminary cross section

A preliminary cross section was calculated and compared to data from the ENDF/B-VII.1 evaluation [81] (see fig. 6.11). To obtain absolute values, in accordance with eq. 2.2, the ^{235}U cross section from the ENDF/B-VII.1 evaluation [81] was used. The measured fission counts have been extrapolated in the $|\cos \theta| \in [0, 0.3)$ region assuming an isotropic emission.

The experimental cross section shows a tendency of being systematically too low except for low energies, but around the resonance region the agreement is fairly good. The measured cross section peaks at 243 keV, close to the expected energy. With better statistics the binning can be made finer and the neutron-energy resolution is expected to improve if a couple of Bi and Pb resonances could be identified for the ToF calibration (see section 6.2.2.2).

For energies below ~ 150 keV or above 1 MeV large systematic differences compared to the evaluation are seen. In the low energy region the measurement overestimates the cross section due to a troublesome background. Also for the higher energies a cluster of background events partly overlaps with the α -particle distributions making it difficult to correctly select the appropriate events. These events were later confirmed to be partly stopped tritons (see section 6.4). Part of the underestimation of the cross section at higher energies can be explained by the *particle leaking* effect, discussed earlier in section 6.1, which becomes more important the higher the neutron energy is. Since the tritons are not fully stopped but still deposit some of their energy in the detector, the *particle leaking* effect becomes difficult to correct for.

6.2.3.4 Choice of gas

As was mentioned in section 3.1 the gas mixture is an important parameter to take into account, in order to obtain well behaving signals. The gas determines the size of recombination effects as well as formation of negative ions (by atomic or molecular capture of an electron).

Both P-10 (90% Ar+10% CH_4) and 95% Ar+5% CO_2 gas mixtures have been tried and the results were quite different (compare the distributions in fig. 6.12 to the distributions in fig. 6.5). For the Ar+ CO_2 mixture, the grid PH becomes increasingly negative with higher anode PH. Due to the distortion of the grid-anode spectrum when using Ar+ CO_2 , the data could not be properly analysed and a switch back to P-10 was performed.

According to studies of the drift velocities in these gas mixes [86–88], one concludes that a drift velocity, in the gas volume between the cathode and the grid, of 4 to 4.5 V/(cm Torr) is expected for both our gas mixes, given the voltages and pressure in use (reduced field strength of 0.428 V/(cm Torr).

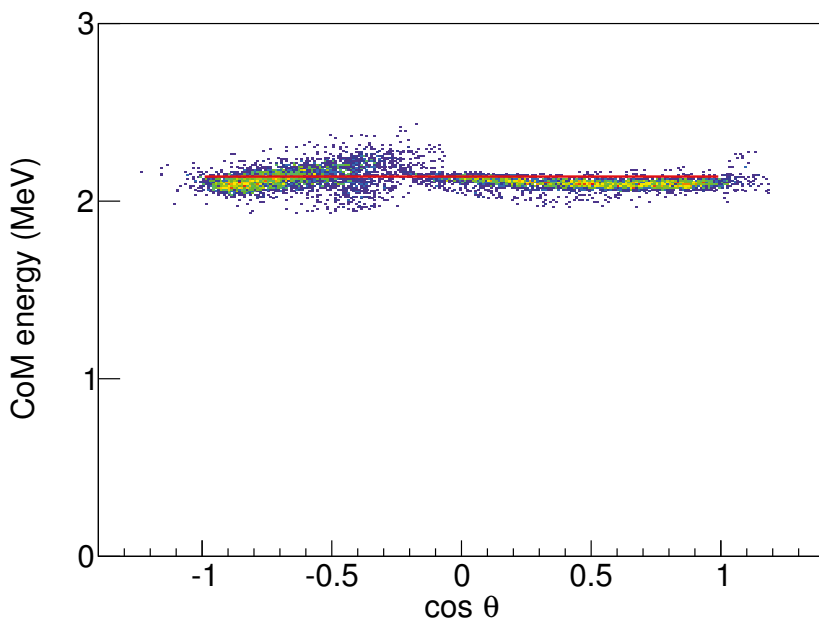


Figure 6.10. α -particle energies and angles in the CoM frame for events with neutron energies of 200 to 250 keV. The solid line represents the expected particle energy given a neutron energy of 225 keV.

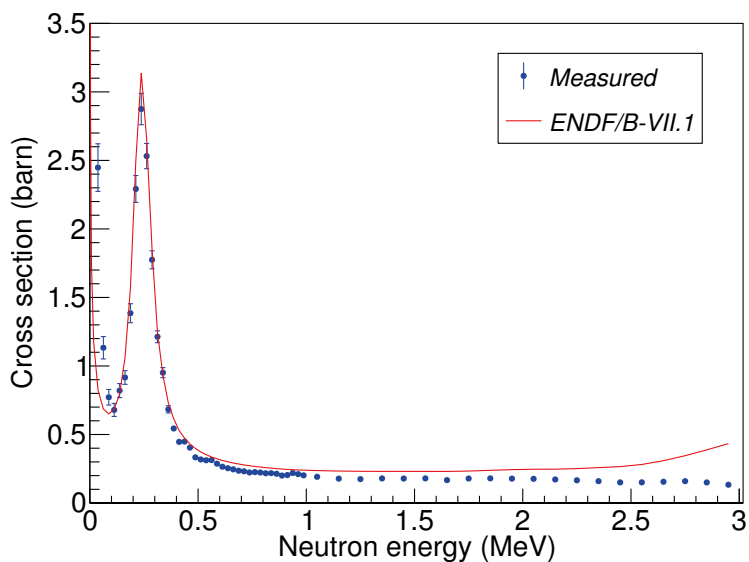


Figure 6.11. Deduced cross section of the ${}^6\text{Li}(n,\alpha)t$ reaction from the first experimental run, the error bars represent statistical uncertainties only. Agreement with evaluated data in the low energy region is poor, and the cross section in the high energy region is systematically underestimated. Nonetheless, around the resonance region our measured data agrees well.

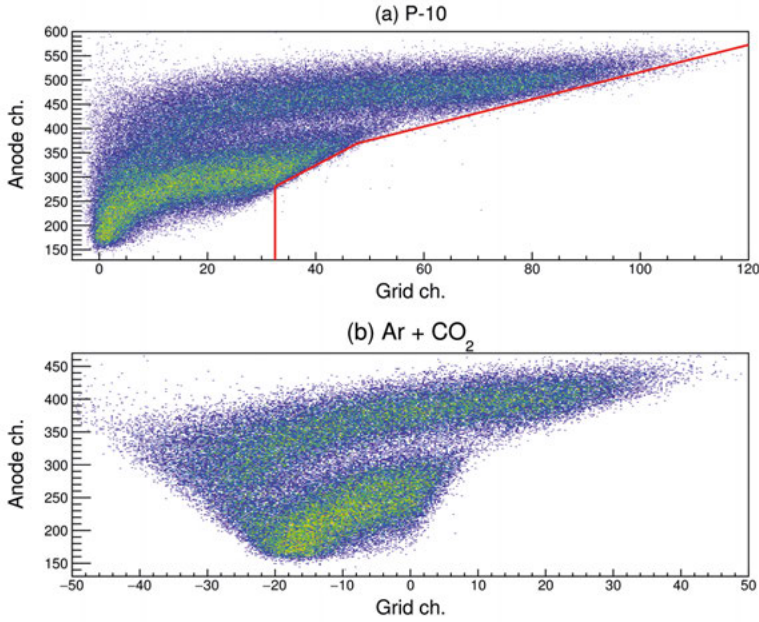


Figure 6.12. In the two panels the effect of using the 95% Ar+5% CO₂ gas mixture is seen. Roughly half the events in panel (b) have negative grid PHs, and a dependence on the anode PH is seen. Clearly this distribution is distorted compared to the one in panel (a), where P-10 gas was used.

Neither gas mixes actually reaches a plateau, the CO₂ mix is on or before the drift velocity maximum, while the corresponding position of the P-10 value lies well after the maximum. The appearance of negative grid signals in the Ar+CO₂ gas mixture can therefore not be explained by a difference in drift velocity. The more likely explanation is differences in chemistry, e.g., electron affinities of the gas molecules.

With adjusted and tuned voltage settings, it is possible to use Ar+CO₂ as the chamber gas without these distortions. The previous measurement by Knitter et al. [89] used this gas at 3.8 bar. More systematic studies like the one by Bevilacqua et al. [25] are needed to evaluate the best settings.

6.3 Second experiment

6.3.1 Changes compared to the original experiment

During the beginning of 2015 the setup was moved to a closer position (10 m) with a moderated beam. This allowed us to gather statistics and identify problems much faster since the neutron flux is more than an order of magnitude larger at the shorter distance. At the new position the background situation, for both low and high energies, seemed to have changed and did not disturb

the α -distributions as much. A major drawback of the first experiment was that the ToF could only be calibrated using the γ -flash, no resonances could be determined unambiguously. This was thought to be mainly a problem of low statistics, which the increased low energy flux should be able to remedy.

The data acquisition system had some limitations, since it was not designed with high count rates in mind. One of them was that the different digitiser modules could become unsynchronised. This happens when one, or more, of the digitiser modules are still processing the last event, while others are ready to take new data. One must make the quicker modules wait for the last module to finish by inhibiting their armed status, until all modules are ready. For low count rates this is a very rare problem, but the high flux from the moderated beam called for a correction procedure as this problem became much more common. A second limitation is that only the first event for each beam bunch could be collected, possibly affecting the cross section at high count rates since the high energy events would be predominately collected.

The events are collected in sets of 100. The first event in this set is guaranteed to be synchronised because the digitisers are all armed simultaneously from the acquisition software running on a nearby PC. All the modules have individual timestamps so the time difference between each subsequent event is known. Whenever one or more modules lag behind, that data becomes shifted with respect to the rest. The unsynchronised events are skipped for the lagging modules until all modules are in sync again. Some complications arise from the fact that each clock in the modules are not running at exactly the same speed but since the clocks can be synchronised at every 'good' event the problem never grows out of hand.

6.3.2 Results

The increased flux at lower neutron energies made the resonance structure of ^{235}U distinguishable in the ToF spectrum. These (positive) peaks served as calibration points in the eV to keV region. In addition the increased statistics also in $^6\text{Li}(n,\alpha)t$ events made it possible to identify a few Pb resonances that were also used in the ToF calibration. This was very important since the γ -flash was no longer well defined. The moderating polyethylene, as well as the several filters put in the beam (Pb, ^{10}B , Na, Co and Ag), greatly broadened the γ -flux. Regardless, the γ -flash would always be a high energy calibration point while we for this measurement needed calibration points in the low energy region.

Since the γ -flash was of no use to us, a veto time gate was setup as the γ 's arrived much prior to the low energetic moderated neutrons. The gate prevented those events completely from being collected. The low statistics at higher energies made it difficult to get good neutron energy resolution in those regions, but we achieved a proof-of-principle that our setup could see and use the filter resonances given enough statistics.

The data looked very promising but the deduced cross section was off, we had too few fission events. After much of the beam time already had passed, it was discovered that the chamber was misaligned and that the neutron beam did only illuminate part of the uranium targets.

The alignment is checked by taking photos of the beam. The γ 's in the beam will react with the photo plate and after some hours you will see exactly where the beam hits your chamber. This was done before the measurement began but most likely the chamber position was accidentally disturbed by, e.g., someone bumping into it or the table supporting it. Unfortunately this was impossible to correct for in the analysis.

The last weeks of beam time was instead used to experiment with new high voltage values and pressures. It had become apparent that the tritons were an unavoidable background. The often partly stopped tritons overlapped with the α -particle distribution. So we decided not to treat the tritons as background and instead try to detect them as well by increasing the pressure.

In order to keep similar voltage ratios and reduced fields, the high voltage must be increased proportionally to the increase in pressure which limited us as the setup could not handle more than 3 kV. It was quickly seen that doubling the pressure reduced the triton background significantly, but at the cost of worsened performance for both α -particle and fission events, which both now experienced a shorter stopping range. Especially the grid resolution was worsened due to lower grid PHs. When the tritons were fully stopped, the *particle leaking* could also be seen and these events counted, which was one of the aims of the measurement.

The higher pressure seemed to be the way to go for the ${}^6\text{Li}(n,\alpha)t$ reaction because with measurable tritons the α -particle were no longer necessary. However, a decent grid resolution is a must for the fission events in order to make the energy correction. A decision was made to split the chamber into two chambers with different pressures before the next measurement.

6.4 Third experiment

6.4.1 Changes compared to the second experiment

The lessons learned from both the previous experiments manifested into a few modifications. The first measurement struggled with low statistics due to the long flight path of 60 m while the second one, situated at 10 m, only had good statistics for low energies due to the moderation. The third experiment ended up at a distance of 30 m from the unmoderated neutron production, a compromise of the two previous experiments. Previous measurements by Knitter et al. measured up to a neutron energy of 330 keV at that distance [89].

The chamber itself was split into two chambers, due to the decision made at the end of the second experiment to employ different gas pressures for the

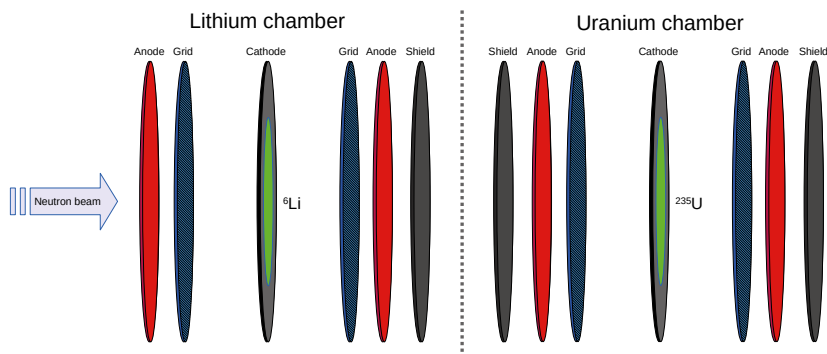


Figure 6.13. The different requirements when it came to gas pressure for the $^6\text{Li}(n,\alpha)t$ and $^{235}\text{U}(n,f)$ reactions forced us to leave the ‘twin’ design and use two separated chambers instead, each with its own gas supply. The arrangement is the same as in fig. 6.2, except that there are now two separate chambers and the lithium target are now closest to the neutron source.

fission and lithium chamber, respectively. The parts were still the same but naturally two new end caps for the flanges were needed.

For the $^6\text{Li}(n,\alpha)t$ chamber these caps were bulging outwards so that they would not ‘pop’ as the pressure changes, which can cause a pressure wave to travel through the chamber and therefore risk damaging the fragile targets. These end caps were already in use for the old chamber which enabled us to test a higher pressure already at the end of experiment two presented in the previous section.

Based on these tests we decided that 2 bar would probably be enough for all but the most energetic tritons, to be able to go higher in pressure we would also need to replace some of the high voltage units. As a consequence we still saw not fully stopped tritons but they were no longer interfering with any other distribution and could be counted. A schematic figure of the split setup is presented in fig. 6.13.

Already from the start the two different uranium targets had shown some inconsistencies, even though the targets were similar in thickness. One example of this, is the larger particle loss in the backward direction, seen in the cosine distribution (fig. 6.8). At the new flight path the beam spot would be larger (5.4 cm diameter in front and 6 cm right behind the setup) than the smaller of the uranium targets (4.5 cm in diameter). To conduct relative measurements the neutron flux for each target must be the same (see eqs. 2.1 and 2.2). Either the neutron beam should be very uniform and cover all targets completely or the targets should be very uniform and be big enough to contain the whole beam. This can be compared to the situation for the first measurement where the beam spot diameter was 9.8 cm, i.e. larger than any of the target diameters. So we exchanged the smaller of the uranium targets for another ^{235}U target

with characteristics much more similar to the the large one already installed. The new target has an areal density of $216.0(16) \mu\text{g}/\text{cm}^2$, a diameter of 7 cm and a total ^{235}U mass of $8310(4) \mu\text{g}$ with the same purity of $99.9336(14) \%$.

To fight the synchronisation issues found in the second run, the digitisers were now supplied a common clock as time reference through a clock and trigger distribution card.

We were running parasitically and the experiment in front of us needed a clean beam without filters. We planned to use some filters to get some resonances when the experiment in front of us was not taking data. However, as we started measuring, we immediately realised we were swamped by events induced by the γ -flash. Even though our flight path was at an 108° angle to the primary beam our chamber's metallic beam window and other parts created a lot of disturbing background and lots of space charges in our detector. Since our acquisition software could only handle one event per beam bunch it so happened that without any veto gate, it triggered on the γ -flash every single time. We made two adjustments to the setup to handle the situation.

The first adjustment was to extend our veto gate used in the previous experiment further, up to a time that roughly corresponded to a neutron energy of 3 MeV. Since no events were collected until this veto gate had ended, we had to accept that we would never be able to measure any higher neutron energies that that, but we never expected to do so anyway. We also decided we could not measure without a beam filter, so 2 cm of lead was installed (the other experiment experienced problems and could not start in time). These two measures made it possible to run the experiment, and with the filters in place we expected to see resonances to calibrate the ToF with.

The strong γ -flash also created a hassle to correctly fit the signals from the $^6\text{Li}(n,\alpha)t$ reaction. In all events induced by neutrons of a few 100 keV or more, the signal trace would contain the γ -flash induced signal as well as the sought for one, piled up on the γ -event. The higher the energy of the impinging neutron, the shorter the distance between the γ -flash and the proper event. A correct fit is imperative to determine the PH, but also the signal rise time, since it is used to correct the ToF.

An algorithm was written that identified the γ -induced part of the signal and removed it (see fig. 6.14). The identification was made based on an analysis of the ToF, PH and derivative. The anode channels had a much worse signal to noise ratio so the analysis of them were aided by the time information from the cathode (the onset of the anode signals are always later than the cathode signal, see fig. 3.2).

Above a neutron energy of about 1 MeV some of the $^6\text{Li}(n,\alpha)t$ events started merging completely with the γ -induced signal, why we had to discard the events of this energy or higher. In practice, only events below 0.5 MeV yielded any reasonable results.

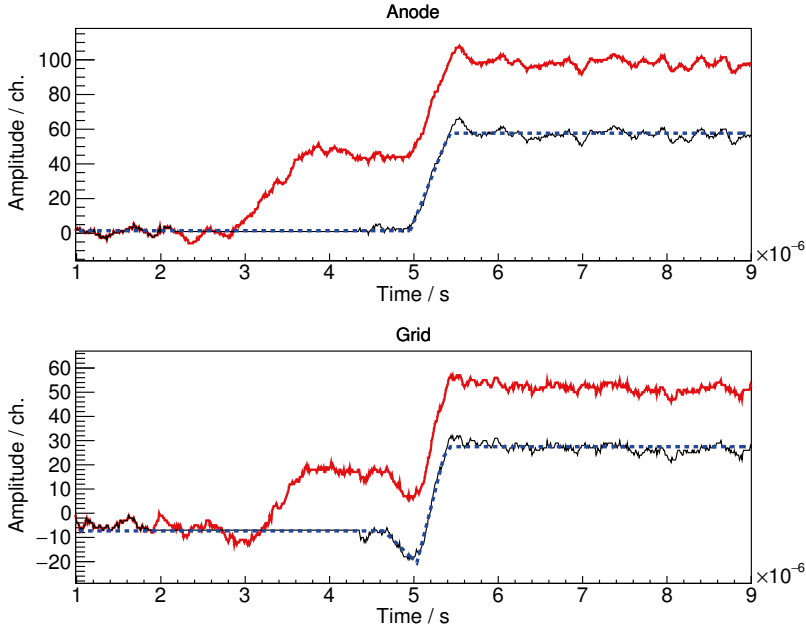


Figure 6.14. Fitted signals of an event from the lithium chamber, which is highly affected by the γ -flash. The lower signal (black) in each panel have had the interval affected by the γ -flash removed from the original signal (red) before the fit (blue) was made.

6.4.2 Results

Exchanging the smaller uranium target not only resulted in a more consistent cross section, but also in a more consistent cosine distribution. Both distributions from the targets are now very similar with a flat top until the particle losses for high angles kicks in (see fig. 6.15).

The improved statistics, compared to the first experimental run, made it possible to unambiguously identify and use seven resonances from ^{208}Pb for the ToF calibration. The resonances covered the energy range 78 to 723 keV, which improved the overall ToF calibration.

In fig. 6.16 a typical situation for the lithium side of the chamber, at intermediate (200 to 250 keV) neutron energies, is depicted. The α -particle distribution is now slightly more compressed since the pressure was increased. Some energy straggling is seen for angles close to 90° (grid channel ~ 0).

The tritons are, for these energies, not fully stopped at near forward angles. Most of them are gathered in a straight distribution leaning upwards, in accordance to the increased energy of forward directed particles. As the tritons managed to pass through the whole gas volume and reach the anode, they start to deposit less energy in the cathode-anode region. The distribution bends at

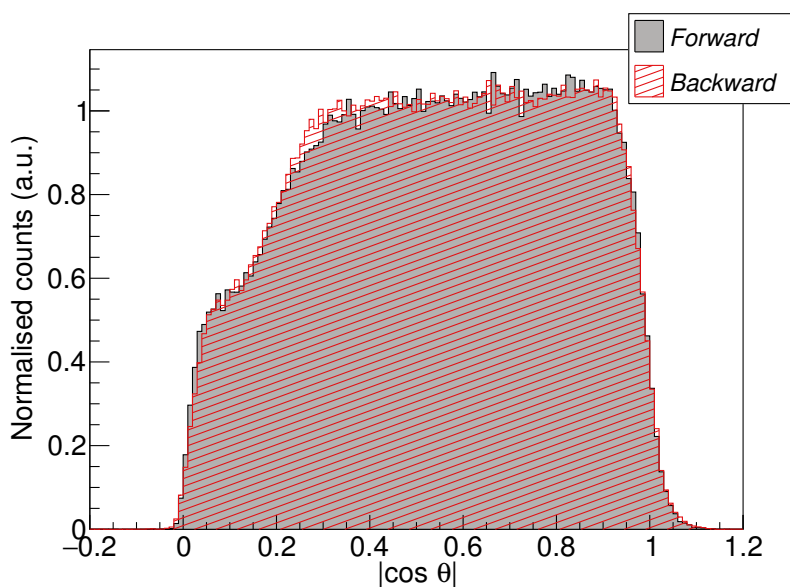


Figure 6.15. After the replacement of the smaller of the uranium targets, the two cosine distributions agree very well. See fig. 6.8 for details and comparison.

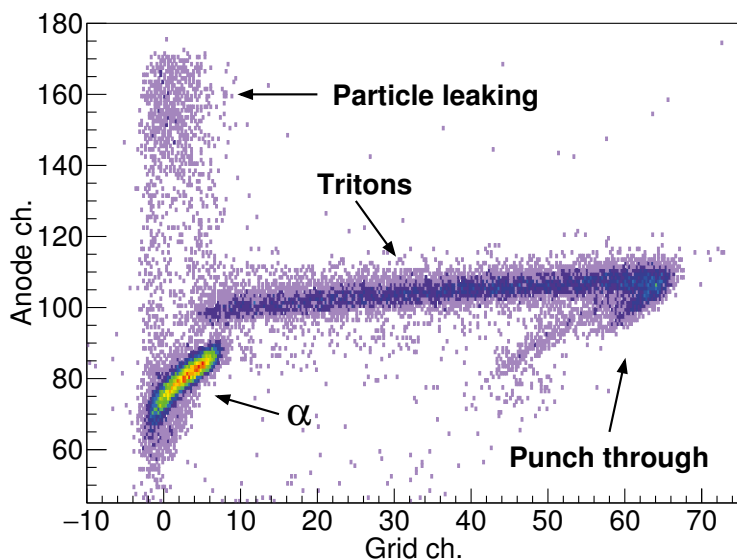


Figure 6.16. With the higher pressure more of the tritons are stopped and one can see the 'punch through' at high grid PHs. Also the *particle leaking* is now properly captured. See fig. 6.7 for details and comparison.

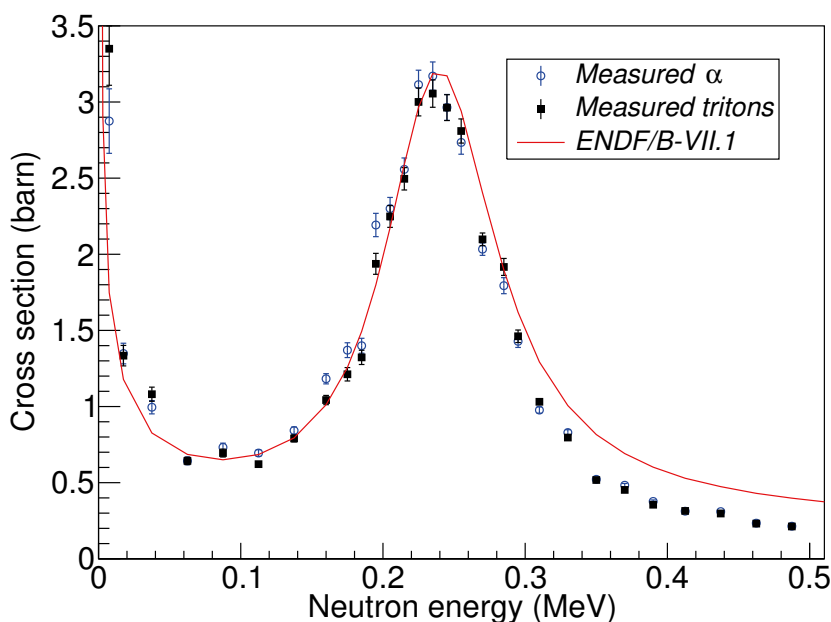


Figure 6.17. Compared to the cross section presented in fig. 6.11, large improvements have been made in the low energy region, and now both the tritons and α -particles have been measured, yielding conforming results. However, the measured cross section disagrees with the evaluation already after 300 keV, and despite much effort the data above a neutron energy of 0.5 MeV could not be properly analysed due to the γ -flash.

a critical angle since the tritons are inducing less net charge on both the anode and the grid.

For low angles, the triton distribution disappears and a cluster of events is formed at much energy. At these angles the *particle leaking* kicks in. The cluster of events at high anode and low grid channels consists of simultaneous detections of both reaction products, boosted into the forward hemisphere. All the distributions are almost completely separated and the background is very low.

Increasing the pressure seem to have improved the situation since the background is very low, and all distributions, including the *punch through* and *particle leaking* effects, are accounted for. Alas, the deduced cross section in fig. 6.17 still shows discrepancies, especially at energies higher than the first ^7Li resonance. At about 300 keV the γ -flash becomes increasingly difficult to handle and at energies above ~ 500 keV the analysis failed to separate the events properly.

Even if most of the γ -induced part of the signal is neutralised the ToF of the event is often affected. Another indication that the ToF calibration might be at fault, is that the the cross section deduced based on α -particles and

tritons, respectively, agree very well with each other at each energy point. The experimental cross section peaks before the cross section from ENDF/B-VII.1 [81], which could be due to a misaligned ToF.

6.5 Improvements for a next experiment

After each measurement, lessons were learned and the setup was improved. However, there are still many things that can be improved if a fourth measurement is attempted in the future.

6.5.1 DAQ

The limit of one event per accelerator repetition is an unnecessary constraint. Upgrading the module that measures the time interval between the start and the stop signal, to a model that can handle several subsequent stop signals would remove this constraint completely.

The higher count rate, the more important it becomes that the timestamps of the digitisers can confirm that the traces from the different digitisers actually describe the same event. Since the file structure was not aligned with the set structure the events were collected in, and since a synchronisation correction had to be performed, the data analysis could not be trivially parallelised. This increased either the time required for analysis or the complexity of the analysis code.

In the third run, it still happened that some of the digitisers become unsynchronised. The only difference, compared to the second run, was that it was easier to correct for, as all the digitisers used the same clock as a reference. It did not solve the fundamental problem of the unsynchronised events though.

6.5.2 γ -flash

The single biggest problem of the last measurements was the influence of the γ -flash. It limited the energy range we could measure and complicated the analysis. Comparing the situations concerning the first and third experiment we see the importance of enough beam filters to properly attenuate the γ -flux to manageable levels. The increased flight length also helped by separating γ and neutron events time wise.

Both these measures decrease the neutron flux as well as the γ flux, as an unwanted effect. As we saw that it was difficult to obtain well defined resonance dips in the ToF spectra, due to the low statistics at 60 m, one would either require much more beam time (and patience) or a shorter flight path. A new measurement at about 30 m with more beam filters (recall that the first experiment employed more than double the thickness than was used during

the third experiment) seems to be the most reasonable choice. A previous measurement by Knitter et al. at the same distance from the neutron source employed 12 cm lead and 18 cm copper, and still experienced large γ -induced signals that limited the available energy range [89]. Thicker filters would also deepen the resonances, leading to more of them being identified and the measured position of them more accurate.

6.5.3 The lithium chamber

The increase in chamber pressure from 1 bar to 2 bar led to a major improvement for the measurement of both α -particles and tritons since their distributions no longer overlapped. The pressure was still a compromise though. The higher pressure decreased the angular resolution for the α -particles and increased the energy loss drastically for events at close to 90° angles. On the other side, many of the tritons emerging from events of intermediate to high neutron energies at close to 0° angles were still only partially stopped in the gas. By accepting additional loss of performance for α -particles one could increase the pressure and focus on measuring tritons with good angular as well as energy resolution. Care would still be needed to make sure appropriate bias on the electrodes can be supplied without causing sparks or ending up with field strengths unfavourable with regards to the electron drift velocity in the gas.

7. Correlated fission observables with VERDI

*When I saw you I fell in love, and you
smiled because you knew.*

— Arrigo Boito

VERDI (*VELOCITY foR Direct particle Identification*) is a fission spectrometer developed at the JRC-Geel. It is designed to measure correlated fission observables through the 2E-2v method.

First results of the current design of VERDI was published by Fréreau et al. [90] at about the same time I joined the project. Since then the setup has been upgraded and the analysis refined. Effort has also been put into better understanding the 2E-2v method in order to explain the results VERDI produces, as well as guiding the continuation and development of the project.

I will focus on the 2E-2v method, but certain aspects of the 2E method will also be relevant to discuss to some degree. A small part of this was presented at the *ND2016* conference [91], but here the current VERDI will be presented and discussed in full for the first time.

7.1 Motivation

Still, after almost 80 years since the discovery of fission we do not know how the fission process works in detail. One important question is how the available excitation energy is distributed between the two FFs. This can be probed by measuring the neutron multiplicity, ν , since the ability to emit a certain number of neutrons requires enough excitation energy to pay for the neutrons' separation energies. The multiplicity can be measured directly, but detecting neutrons is always difficult. Instead one could measure the mass of a fragment both before and after neutron emission and thereby deduce the multiplicity.

To help, or rule out, the developed theoretical models of fission, correlated data is needed. If both the fragments' masses and energies are known simultaneously the correlations between them can say much more than a simple one dimensional spectrum. Providing such correlated data is what VERDI has been designed for. VERDI cannot provide correct correlations event-by-event but it can give average correlations between the masses, energies and other deducible observables.

Mass yields of higher quality than present measurements is also anticipated from VERDI, which could be interesting for applications like the next generation nuclear power plants and transmutation technologies.

7.2 Notation

Throughout this chapter there will be a lot of notation referring to different quantities, often both before and after neutron emission. The, so called, pre-neutron and post-neutron quantities will be marked by superscript (^{pre} or ^{post}, respectively). The variables M , E , t and v will be used to represent mass, kinetic energy, ToF and velocity (strictly speed), respectively. Directly measured uncorrected quantities will have a subscript (_m) differentiating them from their corrected counterparts.

The symbol $\bar{\nu}$ denotes the average neutron multiplicity, for one of the fragments. The average total neutron multiplicity, summed over both fragments, is denoted $\bar{\nu}_{\text{tot}}$. If I need to specify that a quantity belongs to a specific fragment, the corresponding symbol will carry an index of either 1 or 2, while a quantity belonging to a neutron has a subscript (_n).

7.3 The 2E method

Even though VERDI is designed for 2E-2v measurements, the calibration of the setup depend on a 2E analysis of a well-known system, e.g., ²⁵²Cf(sf). I will therefore briefly describe how the 2E method is implemented in the VERDI analysis, before I go through the main 2E-2v method.

As the name suggests the method is based on a measurement of both the FPs' energies. Since less information is obtained compared to a 2E-2v measurement, some previously obtained information is needed to deduce the fragment masses. In the following description it is assumed that there exists a function $\bar{\nu}(M^{\text{pre}}, \text{TKE}^{\text{pre}})$ that will provide the average neutron multiplicity given M^{pre} and TKE^{pre} . In reality, such a function would be based on previous measurements of the same, or similar, fissioning systems.

The analysis of each event will undergo a couple of iterations in order to converge toward the correct energies and masses. The kinetic energies of both particles is directly measured. The needed starting values of the other variables can be set to, e.g.,

$$E_{i=0}^{\text{pre}} = E^{\text{post}} \quad (7.1)$$

$$M_{1,i=0}^{\text{pre}} = M_{\text{sum}} \frac{E_2^{\text{post}}}{E_1^{\text{post}} + E_2^{\text{post}}}, \quad (7.2)$$

where M_{sum} is explained in detail in section 7.4.2.

The next iterations will calculate the properties according to:

$$M_{i+1}^{\text{post}} = M_i^{\text{pre}} - \bar{v}(M_i^{\text{pre}}, \text{TKE}_i^{\text{pre}}) \quad (7.3)$$

$$E_{i+1}^{\text{pre}} = E^{\text{post}} \frac{M_i^{\text{pre}}}{M_{i+1}^{\text{post}}} \quad (7.4)$$

$$M_{1,i+1}^{\text{pre}} = M_{\text{sum}} \frac{E_{2,i+1}^{\text{pre}}}{E_{1,i+1}^{\text{pre}} + E_{2,i+1}^{\text{pre}}}. \quad (7.5)$$

When the variables have converged, usually within a few iterations, the loop is terminated and the analysis proceeds with the next event.

For each emitted neutron two terms have been neglected in eq. 7.4. The expression in eq. 7.4 comes from the assumption that $v^{\text{pre}} = v^{\text{post}}$. The size of this approximation can be determined by estimating the average values of both the terms:

$$\frac{m_n}{M^{\text{post}}} E_n^{\text{CoM}} \quad \text{and} \quad m_n v^{\text{pre}} v_n^{\text{CoM}}.$$

The first term is small, in the order of tens of keVs, and the second term averages to zero in the same manner as discussed in section 7.4.1. We will need to come back and discuss these approximations later in section 7.7.5.

7.4 The 2E-2v method

To utilise the 2E-2v method one needs to know the compound nucleus, i.e., the fissioning system. The 2E-2v method is therefore only strictly valid for first-chance fission. However, for neutron energies high enough to enable multi-chance fission [22], corrections can be made. Here, I restrict myself to first-chance fission.

As the name suggests the 2E-2v method relies on the measurement of the energy and velocity of both FPs. Before I show how the energies and masses, both before and after neutron emission, are derived from this, an important assumption needs to be clarified. All prompt neutrons are assumed to be emitted soon after the FFs become fully accelerated by the Coulomb repulsion.

7.4.1 Isotropic neutron emission

Since no neutrons are measured, the angular distribution must be estimated somehow. For both the 2E and 2E-2v methods, the neutron emission is assumed to be isotropic in the CoM frame of each individual fragment. I will now demonstrate why this assumption is imperative to the 2E-2v method.

Let us observe the system consisting of one of the FFs before neutron emission. Its momentum, $M^{\text{pre}} v^{\text{pre}}$, is by definition along the fission axis. The

CoM velocity in the laboratory frame is therefore given by

$$\mathbf{v}_{\text{CoM}} = \mathbf{v}^{\text{pre}}. \quad (7.6)$$

Assume that this FF emits a neutron, of mass m_n . By letting quantities belonging to the CoM frame be primed I can write down the conservation of momentum in the CoM frame:

$$M^{\text{pre}} \mathbf{v}^{\text{pre}'} = M^{\text{post}} \mathbf{v}^{\text{post}'} + m_n \mathbf{v}_n'. \quad (7.7)$$

The velocities are not so large compared to the speed of light, so I allowed myself to make a non-relativistic derivation for the sake of simplicity. The following expression can be written for the laboratory fragment velocity:

$$\mathbf{v}^{\text{post}} = \mathbf{v}^{\text{post}'} + \mathbf{v}_{\text{CoM}}. \quad (7.8)$$

Combining eqs. 7.6 to 7.8 yields

$$\mathbf{v}^{\text{post}} = \mathbf{v}^{\text{pre}} - \frac{m_n}{M^{\text{post}}} \mathbf{v}_n', \quad (7.9)$$

since $\mathbf{v}^{\text{pre}'} = 0$. Next I take the modulus of both sides of the equation and get

$$\begin{aligned} v^{\text{post}} &= \left| \mathbf{v}^{\text{pre}} + \frac{m_n}{M^{\text{post}}} \mathbf{v}_n' \right| = \sqrt{\left(\mathbf{v}^{\text{pre}} + \frac{m_n}{M^{\text{post}}} \mathbf{v}_n' \right)^2} = \\ &= v^{\text{pre}} \sqrt{1 + \left(\frac{m_n v_n'}{M^{\text{post}} v^{\text{pre}}} \right)^2 - 2 \frac{m_n v_n'}{M^{\text{post}} v^{\text{pre}}} \cos \theta} = \\ &= v^{\text{pre}} \sqrt{1 + a^2 - 2a \cos \theta}, \end{aligned} \quad (7.10)$$

where I have introduced the helper variable $a = \frac{m_n v_n'}{M^{\text{post}} v^{\text{pre}}}$. After a Taylor expansion of the square root,

$$v^{\text{post}} = \left(1 + \frac{a^2}{2} - a \cos \theta - \frac{a^2}{2} \cos^2 \theta + O(a^3) \right), \quad (7.11)$$

we are ready to calculate the average. It is done by calculating the expectation value for each of the cosine terms, remembering that the Jacobi factor $\sin \theta$ comes into play. The final result becomes, after throwing away the higher order terms,

$$\langle v^{\text{post}} \rangle \approx \langle v^{\text{pre}} \rangle \left(1 + \frac{a^2}{2} - 0 - \frac{a^2}{6} \right) = \langle v^{\text{pre}} \rangle \left(1 + \frac{1}{3} \left(\frac{m_n v_n'}{M^{\text{post}} v^{\text{pre}}} \right)^2 \right). \quad (7.12)$$

One concludes that $\langle v^{\text{post}} \rangle = \langle v^{\text{pre}} \rangle$ is a very good approximation since

$$\frac{1}{3} \left(\frac{m_n v_n'}{M^{\text{post}} v^{\text{pre}}} \right)^2 \approx \frac{1}{3} \frac{m_n E_n}{M^{\text{post}} E^{\text{post}}}$$

evaluates to less than 0.01 % for relevant masses and energies.

In the whole 2E-2v analysis, v^{post} is used as an approximation for the non-measured v^{pre} . In the case of $^{252}\text{Cf}(sf)$, estimating v^{pre} by v^{post} is approximately equivalent to a 1 % normal distributed random error in v^{pre} . This error translates into a pre-neutron mass resolution inherent to the method of about 0.8 amu.

7.4.2 Pre- and post-neutron masses and energies

For every event the post-neutron energies are known from start, since they are directly measured along with the post-neutron velocities. The post-neutron masses are easily calculated through

$$M^{\text{post}} = \frac{E^{\text{post}}}{\gamma - 1}, \quad (7.13)$$

where γ is the Lorentz factor. The difference between Newtonian and relativistic calculations is small, but doing it relativistically avoids a systematic error in the order of 0.1 amu. The pre-neutron masses are determined by observing the momentum conservation of the FFs, and using $v^{\text{pre}} \approx v^{\text{post}}$:

$$M_1^{\text{pre}} v_1^{\text{post}} \gamma_1 = M_2^{\text{pre}} v_2^{\text{post}} \gamma_2 \Leftrightarrow M_1^{\text{pre}} = M_{\text{sum}} \frac{v_2^{\text{post}}}{v_1^{\text{post}} \frac{\gamma_1}{\gamma_2} + v_2^{\text{post}}}, \quad (7.14)$$

where $M_{\text{sum}} = M_1^{\text{pre}} + M_2^{\text{pre}}$ and $\gamma_2/\gamma_1 \approx 1$.

One can estimate M_{sum} as the compound nucleus mass, M_{CN} (for VERDI at this stage, always the mass of ^{252}Cf), but that will overestimate the pre-neutron masses. The difference in binding energy goes into the kinetic energy of the fragments thus decreasing the mass of the full system. We can estimate TKE^{pre} classically by

$$\text{TKE}^{\text{pre}} = \frac{M_{\text{CN}}}{2} v_1^{\text{post}} v_2^{\text{post}}, \quad (7.15)$$

and thereby estimate M_{sum} better:

$$M_{\text{sum}} \approx M_{\text{CN}} - \text{TKE}^{\text{pre}} = M_{\text{CN}} \left(1 - \frac{v_1^{\text{post}} v_2^{\text{post}}}{2} \right). \quad (7.16)$$

With this approximation the systematic error is in the same order of magnitude as the excitation energies before neutron evaporation (tens of MeV, or a few percent of an atomic mass unit). Note that one does not ever actually calculate the rest masses since the fragments are, in general, excited after scission. Also, one does not know exactly how many electrons are accompanying them.

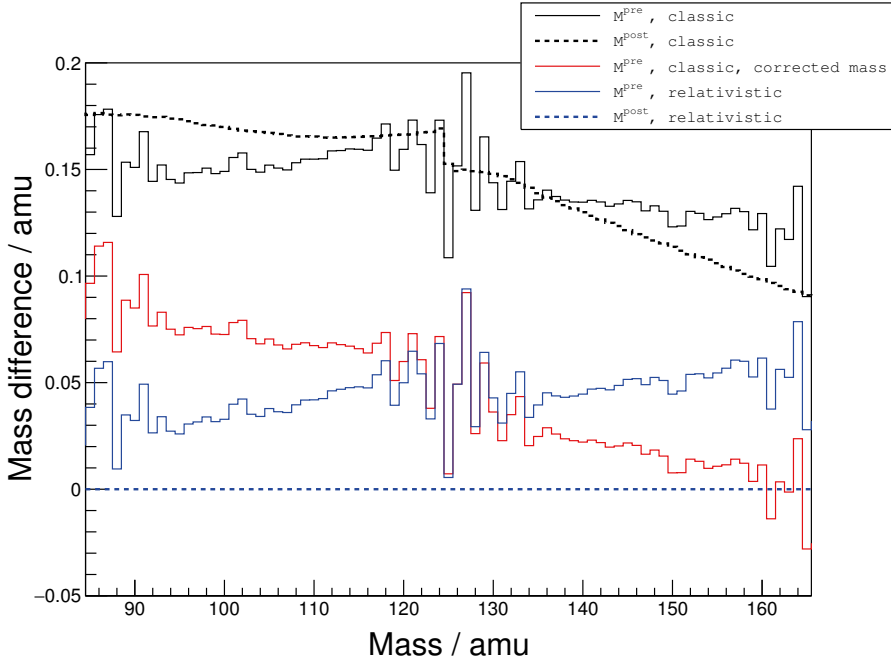


Figure 7.1. Not using the corrected mass in eq. 7.16 introduces systematic errors in M^{pre} . For M^{post} it is important (~ 0.15 amu systematic error) not to calculate the mass using classical kinematics.

Once M^{pre} is known, E^{pre} is given similarly to eq. 7.13:

$$E^{\text{pre}} = M^{\text{pre}}(\gamma - 1). \quad (7.17)$$

The neutron multiplicity, ν , can be estimated using the mass difference before and after neutron emission:

$$\nu = \frac{M^{\text{pre}} - M^{\text{post}}}{m_n}. \quad (7.18)$$

Several papers, including the previously published results of VERDI, report that they are using classical calculations in their 2E-2v analyses [90, 92, 93], mixing proper masses with mass numbers as well as not correcting the compound mass (eq. 7.16). It can easily be shown that these mistakes can introduce small but systematic errors in the results. How these mistakes affect the derived masses is illustrated in fig. 7.1, where one observes how well different calculations will reproduce the true mass.

When calculating M^{pre} , correcting the compound mass (eq. 7.16) is important, while both classical and relativistic kinematics show small remnant discrepancies. In the 2E-2v case these are predominantly caused by the unknown amount of excitation energy and electrons carried by the fragments. For

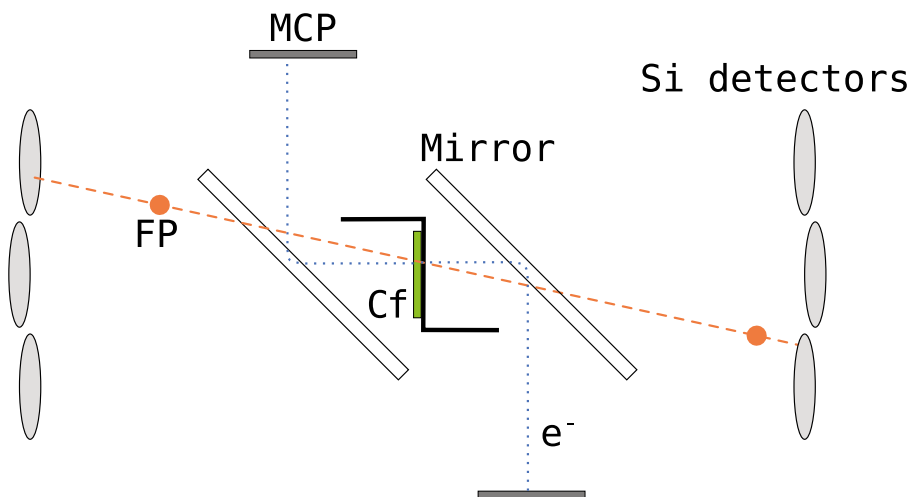


Figure 7.2. A not-to-scale sketch of the VERDI setup. The sputtered electrons (blue dotted lines) are directed toward the respective MCPs by electrostatic reflection in the mirrors. The mirrors are mostly transparent to the FPs so that they can be detected in the silicon detectors. A bent metallic structure shields the MCPs from direct radiation from the ^{252}Cf source, it does not disrupt neither the electrons or FPs.

the M^{post} calculation, it is clear that classical kinematics is inferior and should not be used.

7.5 Experimental setup

The VERDI spectrometer, illustrated in fig. 7.2, consists of a vacuum chamber kept at an operating pressure of less than 1×10^{-7} mbar. Keeping a low pressure is necessary because of the two *Multi Channel Plates* (MCPs) that detects sputtered electrons from particles leaving the target. One MCP is placed on each side of the target. Two electrostatic mirrors, each pairing up with one of the MCPs, face the centred target at a 45° angle, reflecting the electrons onto the respective MCP. A photo of one of the MCP assemblies, just a few moments before it was mounted inside the vacuum chamber, is shown in fig. 7.3. In order to collect all electrons and steer them towards the mirror, an acceleration grid is positioned on each side, 4 mm from the target.

32 silicon detectors are mounted on a spherical surface at about 0.5 m distance from the target. These form 16 detector pairs, facing each other in order to be able to detect both FPs emerging from the target at a relative angle close to 180° . Each of the silicon detectors has a circular surface area of 450 mm^2 . They are of the type *Passivated Implanted Planar Silicon* (PIPS) detectors which features thinner entrance windows and lower leakage currents than standard SSB detectors, but operates in a similar fashion.

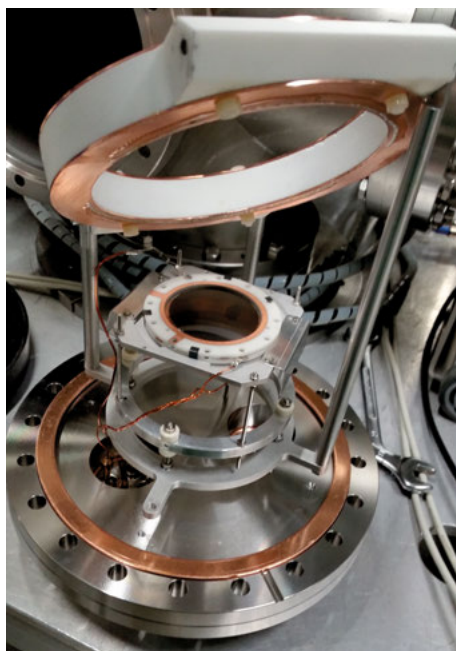


Figure 7.3. One of the two MCP assemblies, moments before it was installed in the VERDI vacuum chamber. The whole assembly is mounted on a vacuum flange. The circular structure in the centre is the MCP, while the larger upper one is the electrostatic mirror.

The particle energies are measured by the silicon detectors which also provide a stop signal for the ToF measurement. The start signal is provided by the sputtered electrons detected on the MCPs. No emission foils are used, enough electrons are emitted from the target itself. This minimises the energy losses of the FPs, which mainly lose energy in the target. The acceleration grids as well as both the front and back planes of the electrostatic mirrors consist of parallel tungsten wires of $50\text{ }\mu\text{m}$ diameter at a 1 mm pitch. The FPs will have to pass through both the acceleration grid and the mirror in order to be detected in one of the silicon detectors. The total transparency for FPs is 85.7% .

Both the acceleration grids and the front plane grids of the mirrors are kept at ground potential. The target itself is kept at -3 kV but due to the symmetric positioning of the acceleration grids, no net force is put on the target. The potential of the back plane of the mirrors, -2950 V , was chosen based on a study of the detection efficiency of α -particles.

The MCPs are in a chevron configuration with the front kept at ground potential and the back plane at 2.3 kV . The silicon detectors were all operated fully depleted. Due to some being regular *Passivated Implanted Planar Silicon* (PIPS) detectors and others neutron transmuted PIPS detectors the required

voltages varied from 70 to 140 V. No performance differences between the two different types of PIPS detectors have been noticed.

The silicon detector signals were fed into pre-amplifiers in a standard fashion. The energy signals were sent to an *Analogue to Digital Converter* (ADC) while the time signals were fed into a *Constant Fraction Discriminator* (CFD). A fission event will only trigger two opposing detectors, so at low count rates only two silicon detectors will have a signal at any given moment. Therefore, only one ADC in conjunction with a signal router was employed for each side of VERDI. Each of the routers directs the active detector signal only, to its corresponding ADC. Similarly, the logical OR of all CFD channels were coded into voltage levels by a *Tag Word Coder* (TWC) module before sent to an ADC. The timing signal from the MCP was fed into a *Time to Analogue Converter* (TAC) together with the timing signal from the silicon detector of the corresponding side. The time difference gave rise to an output signal that in turn was fed into an ADC. A complete scheme of the electronic setup is provided in fig. 7.4.

The $^{252}\text{Cf}(sf)$ source had a 250 nm thick nickel backing. Unfortunately the ^{252}Cf migrates into the backing with time. By observing the different energy losses in events coming from the deposit and backing side, respectively, both in the VERDI data as well as in previous experiments using the same target, an average depth of the ^{252}Cf could be estimated to 62.5 nm. The fission rate was in the order of 2 kHz.

Previously, VERDI had only one MCP installed on one side of the target. After the installation of the second MCP, improvements of the time resolution were expected. The ToF calibration improved, since it relied on detecting α -particles. The α -particles do not sputter many electrons in the opposite direction of the α -particle's movement. This was problematic when a MCP was only available on one of the sides, i.e., the calibration of the opposing side was sub-optimal. With an MCP on each side, this is no longer a problem.

An increase in the coincidence rate of FP pairs was also observed, most likely due to a careful recentring of the target. It is now about 45 % compared to the non-coincident FP detection rate. This is in good agreement with estimations based on simulations, taking the geometry and neutron emission into account as well as the total transmission efficiency of all the grids.

7.6 Simulation study

The conservation of momentum forces the FFs to be emitted collinearly in the event of spontaneous fission (or neutron-induced fission when the incoming neutron has negligible energy). However, this linearity will be broken as soon as a FF emits one or more neutrons. The much more massive fragment, compared to a neutron, will not change its direction much. Nonetheless, a deviation from collinearity by a mere degree will change the position of the

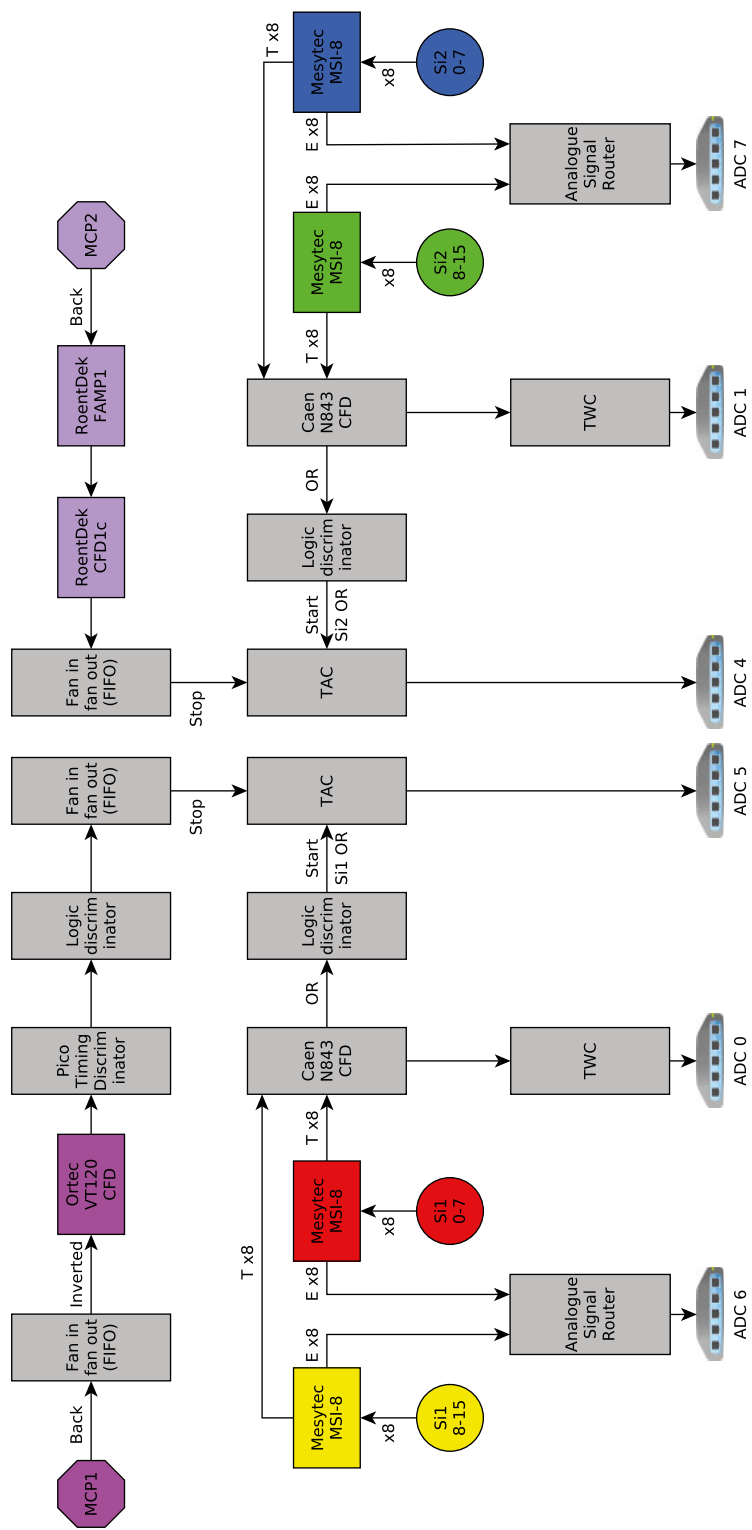


Figure 7.4. Schematic of the electronic setup of VERDI. Ideally, the electronic chains of the two MCPs would be identical, but at the time we did not have duplicates of all modules, and neither did we know which modules performed the best.

fragment, at a distance of 0.5 m, by almost 1 cm, i.e, in the same order of magnitude as the diameter of the silicon detectors used in the VERDI setup.

To investigate and quantify the kinematical influence of neutron emission, a Monte-Carlo sampling scheme was developed. The simulation was also used to answer other questions that emerged during the analysis of the experimental data, e.g., how the PDT (see section 3.4.2) is best handled.

In order to get realistic mass and energy distribution I used GEF (*a GEneral description of Fission observables*) [16] to generate 1×10^6 spontaneous fission events of ^{252}Cf . For each event all necessary properties of both the light and heavy fragments are specified, e.g., mass, kinetic energy and the multiplicity of the neutron emission. Although, GEF manages to reproduce a post-neutron TKE in agreement with measurements of $^{252}\text{Cf}(sf)$, it does not calculate the full kinematics of the neutron emission. Unfortunately, this was the information I was mainly after.

Therefore, I extracted the pre-neutron state of the fragments and the list of neutron energies emitted by each fragment in the CoM frame, both generated by GEF. Subsequently I calculated the neutron emission kinematics relativistically, assuming the neutrons were emitted isotropically in the CoM frame. Since GEF also provided γ -emission information the procedure was repeated for the γ s, even though their kinematical influence on the fragments were minimal. Since GEF does not list masses but rather the nuclear species (A and Z), I fetched the masses from *The Ame2012 atomic mass evaluation* [94, 95].

For each event, a realistic PDT was calculated based on the systematic study of Bohne et al. [96]. The effective fields inside the silicon detectors are well inside the *region I* defined by Bohne et al., so the PDT was always calculated using eq. 3 in their published article [96].

After neutron emission, one is left with two FPs with an angle between their momenta. Since the VERDI setup positions all silicon detectors facing each other pair-wise, as well as facing the target, a too large angular deviation from 180° might cause one of the fragments to miss its detector, even if the other fragment is properly detected. Next, I will outline how the probability of having a coincident event, *given* that one of the fragment is detected, is estimated.

To aid the reader in the geometrical reasoning a simple sketch has been drawn in fig. 7.5. Assume that fragment one (F1) is detected in silicon detector one (D1). Let the horizontal axis coincide with F1's trajectory. The position on the detector surface where F1 hits D1 is uniformly randomised, which determines D1's position relative the z -axis. The position of the second detector (D2) is found by mirroring the vector pointing at D1 from the target centre. Since one knows the relative angle, θ , between F1 and the second fragment F2, the trajectory of F2 only has one degree of freedom, an angle φ (not drawn in figure). By uniformly randomising φ and evaluating the final position of F2, one can determine whether it hits D2 or not, just by comparing the distance between F2 and D2. If it is less than the detector radius, both fragments

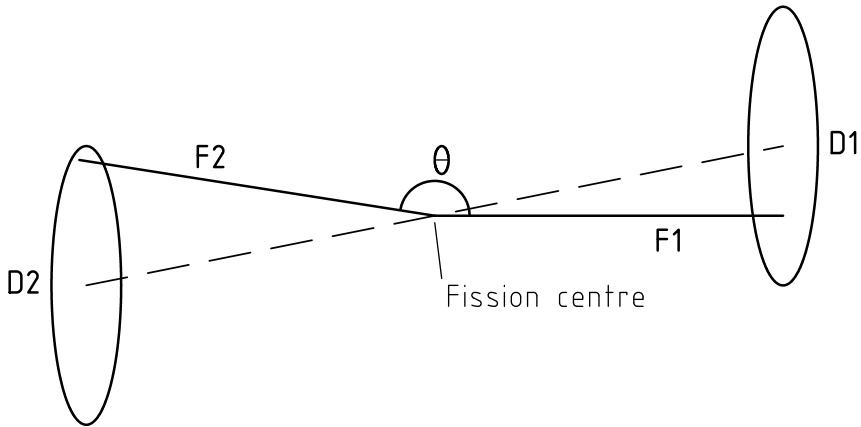


Figure 7.5. Simple (and exaggerated) drawing of how the coincidence rate is estimated in the VERDI setup, given that the first fragment (F1) is detected in a silicon detector (D1). If the second fragment (F2) ends up close enough to the detector centre of D2, it is a coincident event.

are detected in coincidence. This is evaluated 1000 times for each simulated event, and the number of coincident detector hits divided by 1000 is taken as the coincidence probability.

By this treatment, I had access to synthetic data where one could directly see how large of an effect the non-collinearity, due to neutron emission, would have on a 2E or 2E-2v measurement of $^{252}\text{Cf}(sf)$.

Applying the 2E and 2E-2v methods on the synthetic data revealed many new things about the methodologies. How to best correct for the PDT, as well as intrinsic properties of the 2E and 2E-2v methods. The results from these pseudo analyses are presented together with, and in comparison to, the experimental VERDI data the following section.

7.7 VERDI data analysis

The analysis needs several steps to calibrate different aspects of the detection system. Especially the PDT correction described in section 7.7.3 is a complicated matter and require an in-depth discussion. In section 7.7.4 the different calibration options will be compared and in the following section 7.7.5 some inherent effects of both the 2E and the 2E-2v analysis methods will be investigated. Lastly, the detection efficiency of the VERDI setup and consequences due to it will be discussed in section 7.7.6.

Table 7.1. Particle data used for fitting the four parameter schmitt function (eq. 7.19).

M/ amu	Schmitt et al. E/ MeV	Iterative E/ MeV	Müller et al. E/ MeV	ADC peak
4.0012	6.01	6.01	6.01	α
79.92	73.69	73.18	73.33	Heavy
79.92	100.57	99.49	99.28	Light
126.9	78.45	77.58	77.44	Heavy
126.9	107.01	104.59	105.39	Light

7.7.1 Time-of-flight calibration

By using one of the MCPs as the start signal and the other as the stop signal, the timing resolution was deduced from the resulting distribution width. The distribution had a FWHM of 510 ps which corresponds to an individual 360 ps FWHM ($\sigma = 150$ ps) for each of the MCPs assuming that their respective timing resolutions were the same. This is a worse resolution than was found by Zhang et al., using similar MCPs but with larger channel diameters (25 μm instead of our 13 μm) [33]. However, the estimated resolution includes possible contributions from the DAQ system, and the VERDI timing resolution will anyway be dominated by the silicon detector contribution.

The α -particles coming from the ^{252}Cf sample allow me to calibrate the ToF. The different α -particle energies were not all resolved, rather the estimated mean energy 6.01 MeV was used, based on the relative contributions of the unresolved peaks. In addition to the α -decay from ^{252}Cf , significant amounts of ^{249}Cf , ^{250}Cf , ^{251}Cf and decay products were present.

Since mass, charge and energy were all known for these α -particle it was possible to correct for the small energy loss in the sample backing. These light particles do not suffer from any PDT, thus leaving the ToF to be precisely determined. When detecting FPs, this calibration enable VERDI to determine the time between fission and the main charge collection in the silicon detectors. The PDT, which is suppressing the onset of the charge collection process, must be corrected for in these cases.

7.7.2 Energy calibration and PHD corrections

The energy calibration mainly follows the method outlined by Schmitt et al. [38]. For each of the ADC spectra, coming from single silicon detectors, the α -particle, light FP and heavy FP peaks are localised. Their channel positions are extracted by gaussian fits in narrow regions around the bin maximums. The values are used to construct an energy calibration.

The α -particle mass and its mean energy are known, while the masses and energies for FPs corresponding to the light and heavy peak, respectively, are taken from Schmitt et al. [38]. This peak data (found in table. 7.1) are

corrected for the energy losses due to the sample backing, and then fitted to a four parameter function,

$$E_m = \text{schmitt}(x, M) = (a + a'M)x + b + b'M, \quad (7.19)$$

where E_m is the kinetic energy of the detected particle, x the ADC channel, M the particle mass. a , a' , b and b' are the fit parameters. The energy loss, ΔE , in the target backing is calculated using the free library *Range* [97] yielding the post-neutron energy:

$$E^{\text{post}} = E_m + \Delta E(M^{\text{post}}, E_m). \quad (7.20)$$

Since the ^{252}Cf has diffused into the backing the measured energies of both sides needs to be corrected based on the average depth of the ^{252}Cf . The measured velocities are corrected correspondingly:

$$v^{\text{post}} = v_m + \Delta v \quad (7.21)$$

$$\Delta v = \sqrt{\frac{2E^{\text{post}}}{M^{\text{post}}}} - \sqrt{\frac{2E_m}{M^{\text{post}}}}. \quad (7.22)$$

The FP energy spectra produced by this calibration agrees fairly well with the data of Schmitt et al. [38], but overestimates the energy somewhat. However, while it produces a similar $\langle \text{TKE} \rangle$ as Schmitt et al. it disagrees with later measurements [98] that measured a significantly lower $\langle \text{TKE} \rangle$. In order to remedy this problem several different calibration procedures were tried. The resulting E^{post} distributions are found in fig. 7.6 and their corresponding parameters values are found in table 7.1.

Among the more successful ones were an iterative procedure. It was based on a Monte Carlo search in the Schmitt parameter space, trying to reproduce well known quantities like average masses and energies for the light and heavy fragments and \bar{v}_{tot} . The resulting parameter values, that gave seemingly correct distributions as well as good average values of TKE^{pre} and TKE^{post} , are found in table 7.1 in the ‘iterative’ column.

In the end I settled for using the analytically corrected parameters by Müller et al. [92], which gave mostly qualitatively similar results as the previously described iterative method, but required no iterations and are not affected by the PDT correction discussed in section 7.7.3. That energy calibration also improved the $\bar{v}_{\text{tot}}(\text{TKE}^{\text{pre}})$ distribution which is discussed in section 7.7.4.

I also investigated, if one could deviate slightly from the prescription of Schmitt et al. [38] by using the information of the α -particles in addition to the heavy ion data (and thereby having one more degree of freedom than the number of parameters). By also using the α -peak I could apprehend a calibration valid also for lower masses and energies, useful to look for, e.g., ternary fission. However, some precision in the fission mass region had to be sacrificed so it was not used in the main analysis.

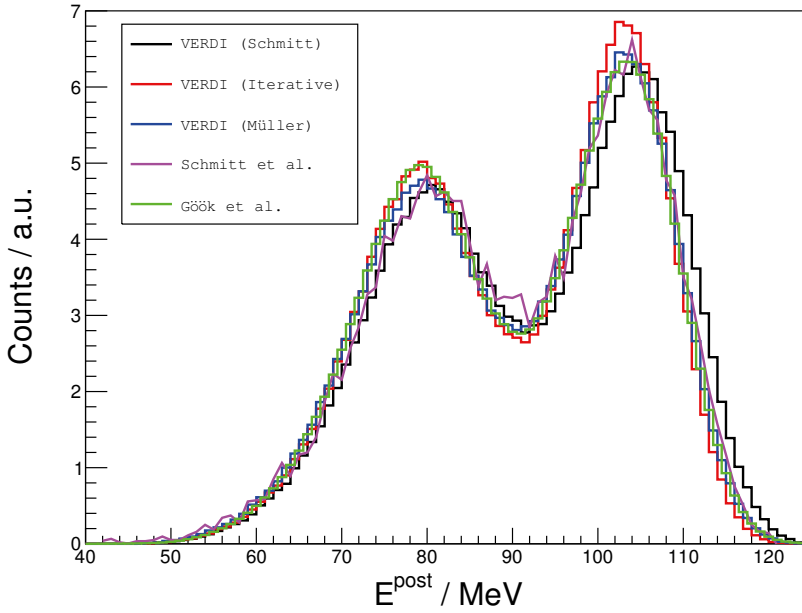


Figure 7.6. The results of applying different energy calibrations to the VERDI data, compared to the energy distributions of Schmitt et al. [38] and Gök et al. [98].

7.7.3 PDT corrections

There are many recipes in literature of how one should correct for the PDT in silicon detectors. Studies of the PDT itself have been performed using accelerated ions [96, 99] but the results have not been easy to apply to new experimental setups, so experimentalists have found their own ways of dealing with this. The true ToF is often determined by the 2E method [93] and due to the dependence of a previously ‘known’ \bar{v} such measurements could arguably be called $2v$ assisted 2E. However, as in the case for VERDI, one could use one fairly well known system, i.e. $^{252}\text{Cf}(sf)$, to calibrate the PDT correction, and after that make a ‘true’ 2E- $2v$ measurement on another system. A similar approach was used by Müller et al. [92].

7.7.3.1 Former PDT correction

The PDT correction procedure previously used for the VERDI analysis, originally suggested by Velkovska and McGrath [99] (hereby referred to as the Velkovska method), prescribes that a linear fit is made, relating the measured apparent velocity, v_m , to the true velocity, v^{post} .

In the case of VERDI, the true velocity was taken as the velocity derived by the 2E method. However, the linearity is deluding. Since $v_m \approx v^{\text{post}}$ it is obvious that the relation can be fairly well described by a linear function. But

this relation does not capture the small perturbation introduced by the PDT, at least not in any other way than a coarse grained average.

Still, this correction is enough to make many of the one dimensional plots agree quite well with previous measurements and the errors do not show up clearly in the experimental data until you observe correlations in, e.g., two dimensional plots. The, with previous measurements [98], seemingly well-agreeing one-dimensional distributions are depicted in fig. 7.7, while $\bar{v}(M^{\text{pre}})$ and $\bar{v}_{\text{tot}}(\text{TKE}^{\text{pre}})$ are discussed later together with the results of the other correction methods in section 7.7.4.

While the calibration of the energy and the timing can influence each other in an experimental situation, it is easy to separate them when working with synthetic data. The energy calibration can cover up problems in the PDT correction and vice versa. To properly establish that the linear correction does not estimate the PDT well, I made a 2E-2v analysis of the synthetic data, using the Velkovska method to correct for the PDT. In fig. 7.8 several plots are shown that show the effect of correcting the PDT the wrong way.

If one looks carefully, it is clear that the relation between the measured and true velocity is not very well represented by a linear function. The \bar{v} as a function of M^{pre} gets distorted, and the seemingly rather well agreeing experimental $\bar{v}(M^{\text{pre}})$ (see **Ana II** in fig. 7.12) is most likely due to a compensation in the energy calibration procedure. One can also directly observe the PDT corresponding to this correction, which does not reproduce the true PDT and has a completely different shape. These findings leave only one conclusion, the Velkovska method is ill-suited to correct for the PDT.

7.7.3.2 New iterative PDT parametrisation

Even though the Velkovska method turned out to be wrong, one notes that especially the M^{pre} distribution in fig. 7.7 looks really good including a higher peak-to-valley ratio which can be interpreted as higher resolution. The division in eq. 7.14 will, to a large part, cancel systematic errors and that makes the M^{pre} distribution more resilient to small disturbances, e.g., erroneous PDT corrections. The PDT calculated by the 2E method was therefore parametrised as a function M^{pre} and E^{pre} calculated with the 2E-2v method, believing them to be more trustworthy. It would be a more natural choice to parametrise using M^{post} and E^{post} , since those variables actually describe the particle hitting the silicon detector, but M^{post} is expected to have larger uncertainties than M^{pre} .

For most 1 amu mass intervals the trend was very clear; the PDT as a function of E^{pre} was a linear function. Fitting linear functions to this data and then plotting the slope and intercept as functions of M^{pre} revealed that they too behaved linearly. These linear behaviours are depicted in fig. 7.9. Thus, one gets a similar parametrisation for the PDT as one already have for the PHD (eq. 7.19):

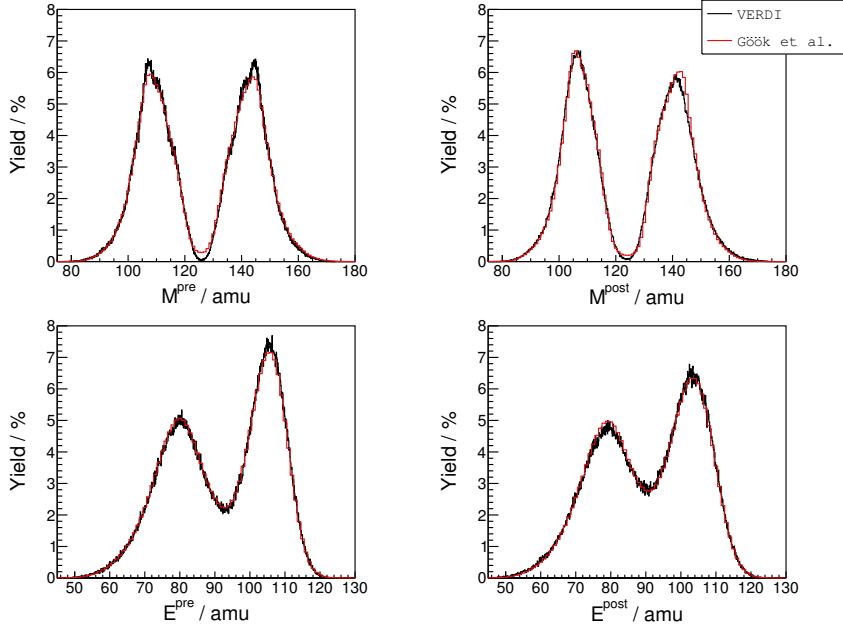


Figure 7.7. Even though the Velkovska method [99] could be shown (fig. 7.8) to be incorrect, many distributions were still in good agreement with the previous ones measured by Gök et al. [98].

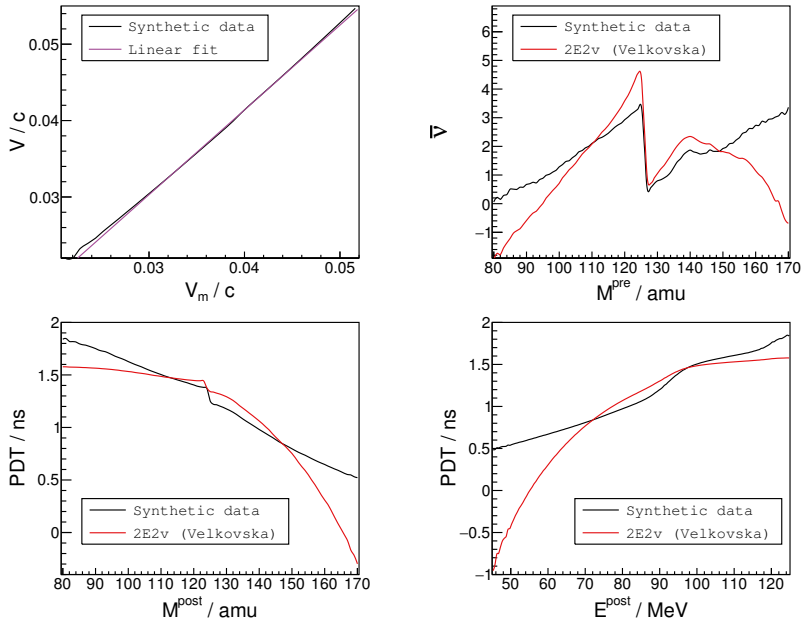


Figure 7.8. The Velkovska method fails to reproduce the synthetic data, and the linear relationship the method is based on is not observed.

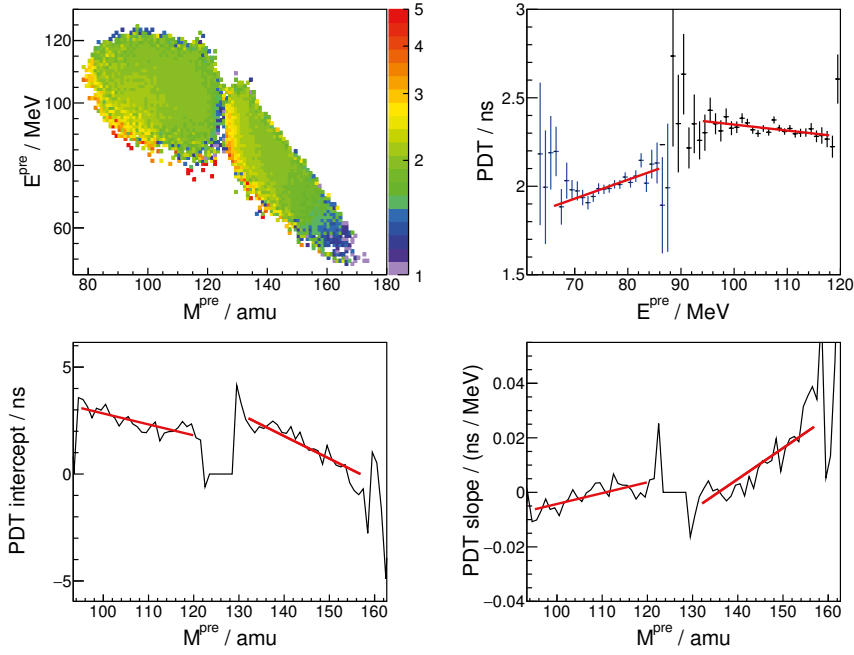


Figure 7.9. The development of a new PDT correction procedure is based on the observed linearity of the 2E-calculated PDT as a function of M^{pre} and E^{pre} . In the top left panel the PDT is plotted as a function of M^{pre} and E^{pre} . In the top right panel one finds the PDT as a function of E^{pre} for two example masses, ~ 105 amu (black) and ~ 147 amu (blue), which are both fitted to linear functions (red). In the bottom panels, the intercept and the slope of the just mentioned functions are given as functions of M^{pre} . The intercept and slope are then in turn fitted to linear functions, separately for light and heavy masses. No fits are made for masses around symmetry due to a non-linear behaviour.

$$PDT(M^{\text{pre}}, E^{\text{pre}}) = (c + c' M^{\text{pre}}) E^{\text{pre}} + d + d' M^{\text{pre}}. \quad (7.23)$$

There are two caveats though. Firstly, the linear relationship for light fragments is different from the heavy fragment dito. This is because the light and heavy fragments have two separate distributions of kinetic energy. Secondly, the correction parameters must be determined iteratively. The 2E-determined PDT will not be correctly correlated with the M^{pre} calculated using the 2E-2v method, since both methods can only predict average behaviours. One needs the average PDT from the 2E method as a function of M^{pre} and E^{pre} from the 2E-2v method. But, without an accurate PDT, the 2E-2v method's estimations of M^{pre} and E^{pre} will themselves be less accurate. Therefore, the first iteration will perform the 2E-2v calculation assuming the PDT is zero. Each following iteration will use the result of the previous iteration to get better and better

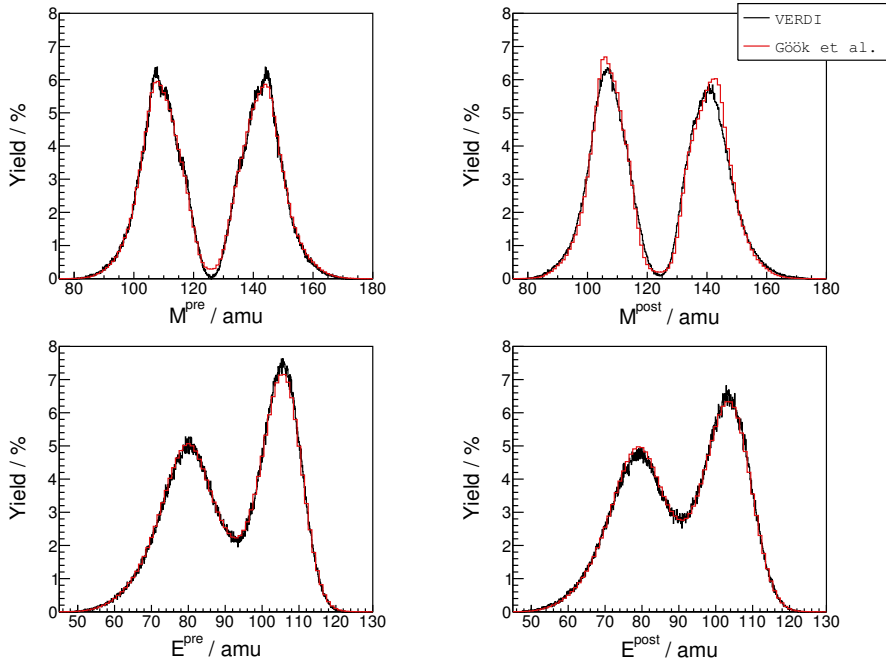


Figure 7.10. The new PDT correction produces several one dimensional distributions that agree well with the previous ones measured by Gök et al.

estimations of the PDT. Only a few (~ 3) iterations are needed for the results to stabilise.

At this stage the correction can reproduce several distributions at least qualitatively (see fig. 7.10 and the comparison in figs. 7.12 and 7.13), but improvements are still needed. Some suggestions for such improvements are provided after the comparison of the different methods in section 7.7.4.

Since I could rule out the Velkovska method based on simulations, it is not more than fair that also this new method is put to the test. Figure 7.11 shows the derived PDTs as a function of M^{pre} . The same pseudo data used to disprove the Velkovska method have been analysed using the new PDT correction method. At the same time the PDT derived from the 2E method is plotted, as well as the true PDT as a reference.

In this case, it turned out that the average PDT could be very well parametrised by eq. 7.23. However, only if the parametrisation was based on the true PDT, not the one derived from the 2E analysis. In fact, the 2E method was found not being able to fully reproduce the PDT, showing deviations exceeding 10 %.

The failure of the 2E method lies in eq. 7.4 where the recoil due to neutron emission has been neglected. The error then propagates to M^{pre} of both the

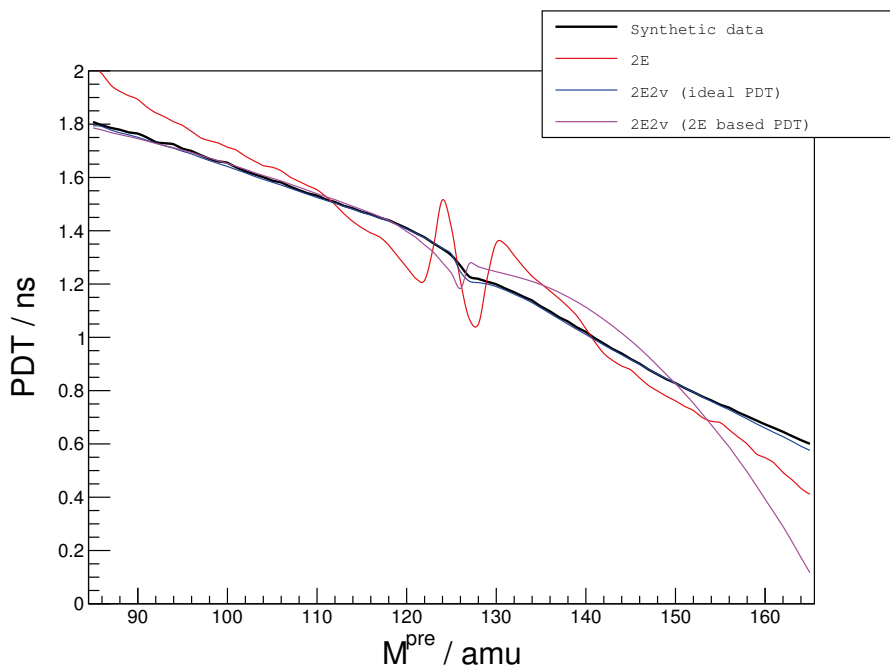


Figure 7.11. The new iterative PDT correction is tested in two ways. One curve shows the derived PDT when it tries to parametrise the true PDT from the synthetic data. Another curve shows the PDT when the parametrisation is based on the 2E calculated PDT. The true PDT and the 2E PDT is also shown as references.

fragments through eq. 7.5. The inability to determine the correct ToF, shows that the 2E-deduced correlation between M^{post} and E^{post} is not correct.

7.7.3.3 Another option?

Another very simple correction has been suggested by Brinkmann et al. which utilises the target backing in a clever way [100]. Small intervals around the heavy and light fragment peaks in the energy spectrum were used in order to know the mass approximately. Due to the energy loss on the backing side Brinkmann et al. could calculate how the PDT changed with energy for the peak masses. The observed PDT behaviour was then extrapolated to the whole dataset.

Unfortunately this is difficult to do for the VERDI setup since much of the ^{252}Cf have diffused into the nickel backing of the currently used target. With a new target the position of the ^{252}Cf would be well defined and this method could be attempted.

7.7.4 Comparison of calibration methods

While it is fairly easy to reproduce one dimensional distributions with several different calibration methods and parameter sets, the differences show up more clearly when observing the important variable \bar{v} as a function of other observables. Especially the correlation between \bar{v}_{tot} and TKE^{pre} is sensitive to both the PHD and the PDT correction in use. In figs. 7.12 and 7.13 I show the results from three different analyses which are defined by the different choices of PHD and PDT corrections:

- Ana I** Using the ‘iterative’ Schmitt parameters (see table 7.1) for the PHD correction, and the Velkovska method for the PDT correction.
- Ana II** Using the Schmitt parameters from Müller et al. (table 7.1) for the PHD correction, and the Velkovska method for the PDT correction.
- Ana III** Using the Schmitt parameters from Müller et al. (table 7.1) for the PHD correction, and the new iterative PDT correction method.

Running the analysis with the set of parameters from Müller et al. also corrected an erroneous behaviour when observing \bar{v}_{tot} as a function of TKE^{pre} . A high TKE^{pre} implies a low TXE. Therefore, one expects a lower \bar{v}_{tot} for fission events with high TKE^{pre} , since the neutron boil-off only stops when there is no excitation energy left to pay for the neutron separation energy with. The negative inverse of the slope therefore relates to the average needed energy needed to emit a neutron. The kinetic energies of the fragments do not change much on average during the neutron emission, so a very similar correlation is expected for $\bar{v}_{\text{tot}}(\text{TKE}^{\text{post}})$.

When several different correction methods show similar mass and energy distributions $\bar{v}_{\text{tot}}(\text{TKE}^{\text{pre}})$ can often tell which ones make sense to use. A method not reproducing a reasonable trend in \bar{v}_{tot} is unacceptable and even unphysical. In fig. 7.13 one sees one such an example, where the analysis **Ana I** gives a positive slope for $\bar{v}_{\text{tot}}(\text{TKE}^{\text{pre}})$ even though the $\bar{v}(M^{\text{pre}})$ in fig. 7.12 looks very promising. The slope when **Ana II** is used (also in fig. 7.13) still deviates significantly from the expected value of about $-\frac{1}{12.6} \text{ MeV}^{-1}$ [98], but it is at least negative.

We see improvements going from **Ana I** to **Ana II** due to the improved Schmitt parameter values used in the energy calibration that describes the PHD better. Going from **Ana II** to **Ana III** one sees similar performances when looking at $\bar{v}(M^{\text{pre}})$ in fig. 7.12, but **Ana III** gives slightly better slopes in fig. 7.13. The slope for **Ana III** corresponds to 12.7 MeV per neutron in the TKE^{post} case, but 23.5 MeV per neutron for the TKE^{pre} case. For **Ana II** these numbers instead become 15.4 MeV and 39 MeV per neutron, for TKE^{post} and TKE^{pre} respectively.

It might still require some refinements, but the new iterative PDT correction method is currently the most promising for VERDI at the moment. Comparing the analysis options once again in fig. 7.14, one sees how the new PDT

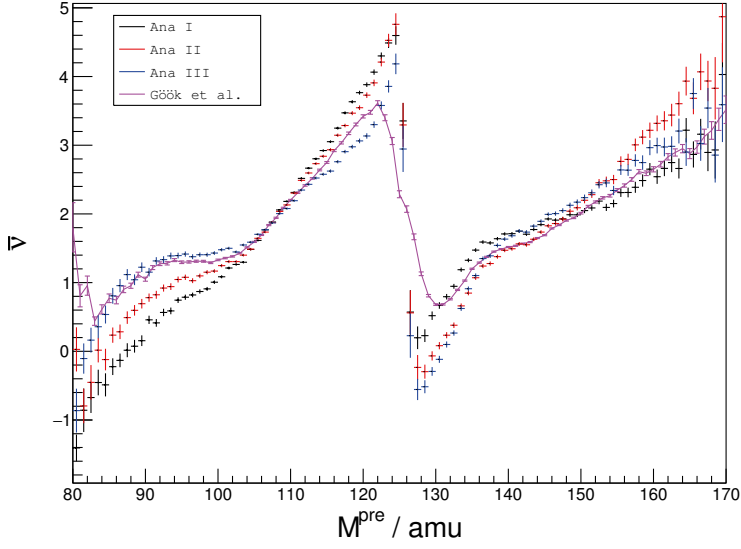


Figure 7.12. The average neutron multiplicity ($\bar{\nu}$) as a function of M^{pre} calculated using the different analysis choices **Ana I–Ana III**. The measurement of Gök et al. [98] was added as a reference. See the text for definitions and discussion.

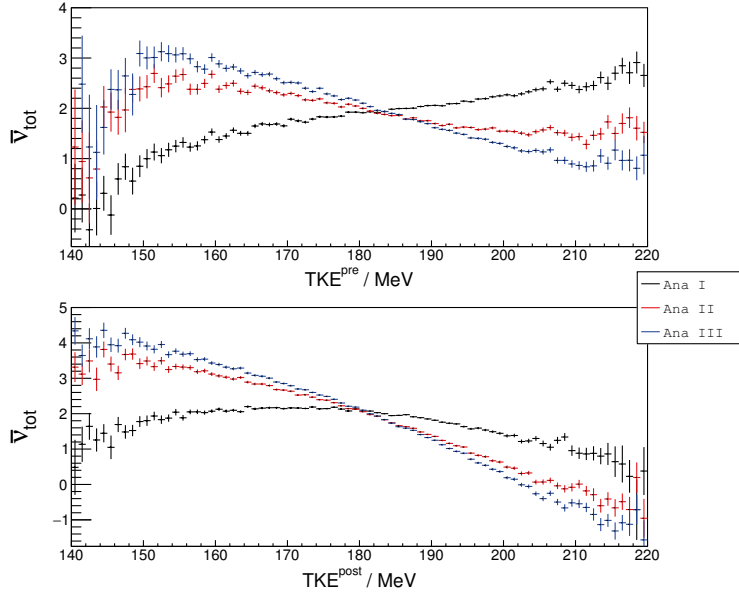


Figure 7.13. The total neutron multiplicity ($\bar{\nu}_{\text{tot}}$) from both FPs as a function of TKE^{pre} and TKE^{post} , calculated using the different analysis choices **Ana I–Ana III**. See the text for definitions and discussion.

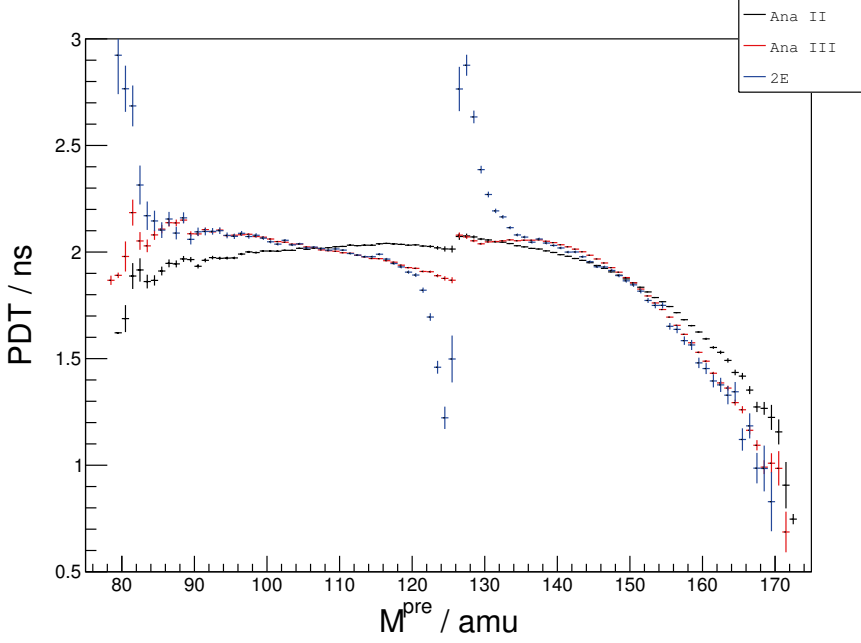


Figure 7.14. Experimentally derived PDT using the Velkovska method (**Ana II**), the newly developed parametrisation (**Ana III**) and the 2E method, respectively.

correction manages to replicate the 2E PDT for all masses except in the symmetry region. The discontinuity seen in the 2E result around symmetry, partly originates from the differences in the kinetic energy distributions of the light and heavy fragments respectively. Though, it was shown already in fig. 7.11 that basing the PDT correction of a 2E analysis might be problematic.

7.7.5 Intrinsic deficiency in the 2E-2v method

Previously, the simulated synthetic data have reflected the experimental situation by modelling the PDT in the silicon detectors. In this section the PDT will be removed from the data so that the 2E-2v analysis has access to perfectly known velocities.

The 2E-2v method is generally performing well, and reproduces the synthetic data once the PDT has been taken care of. There is, however, one important exception: the 2E-2v calculated $\bar{v}(M^{\text{pre}})$ shows large discrepancies in the symmetry region as well as in the tails of the mass distribution (fig. 7.15). Parts of the discrepancies in the experimental data are very similar to the simulated results.

The reason for these discrepancies goes back to the original assumption of the 2E-2v method. The neutron emission might be isotropic on average, but

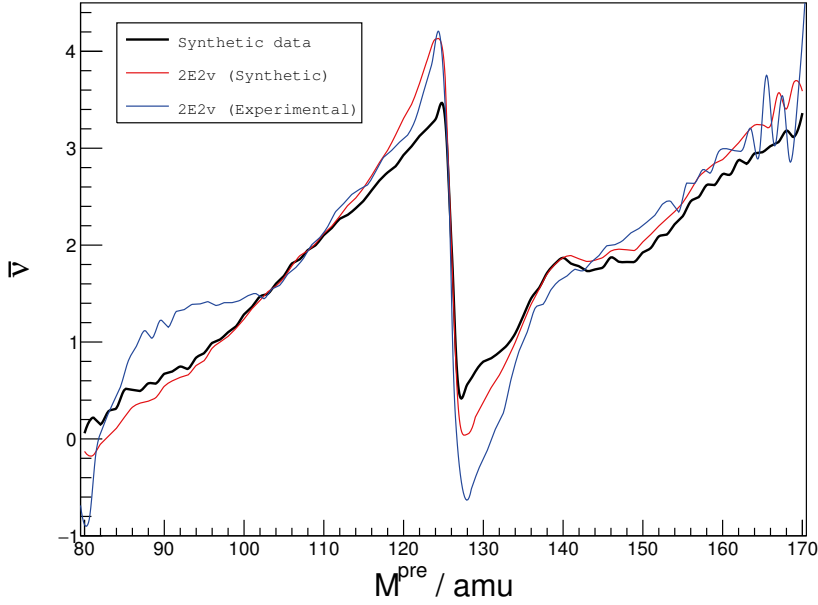


Figure 7.15. Calculated average neutron multiplicity by analysing synthetic data without PDT with the 2E-2v method. Some features are common with the experimental $\bar{\nu}(M^{\text{pre}})$ (**Ana III**) which is shown as a reference.

certainly not for any single event. Only in the case of cold fission, where no neutrons are emitted, will the analysis ever be able to calculate correct masses and energies on an event-by-event basis. One should note that the average neutron multiplicity is not affected, the problem only shows when $\bar{\nu}$ is observed as a function of another correlated observable. Even though the same assumption is made, such an effect will never be observed from a 2E analysis since the $\bar{\nu}$ used as input is reproduced by design, which thereby masques the problem to some degree.

Approximating v^{pre} with v^{post} leads to an equal chance of over- and underestimating v^{pre} , respectively. This affects the calculations in eqs. 7.14 and 7.17 where this approximation has been made. Since this approximation is not present in eq. 7.13, M_1^{post} and M_2^{post} are unaffected. Thus, from eq. 7.18 it is then clear that ν will be over- respectively underestimated if M^{pre} is. That is, the error due to our estimation of v^{pre} creates a positive correlation between the calculated values of M^{pre} and ν .

Three examples, for events of specific mass numbers (110, 120 and 130), is shown in fig. 7.16. The 2E-2v method creates a clear positive correlation between M^{pre} and ν as expected from eq. 7.18.

One needs to take the mass yield into account since $\bar{\nu}$ is an average quantity. As an example we will observe how $\bar{\nu}(M^{\text{pre}})$ is affected when it is evaluated for

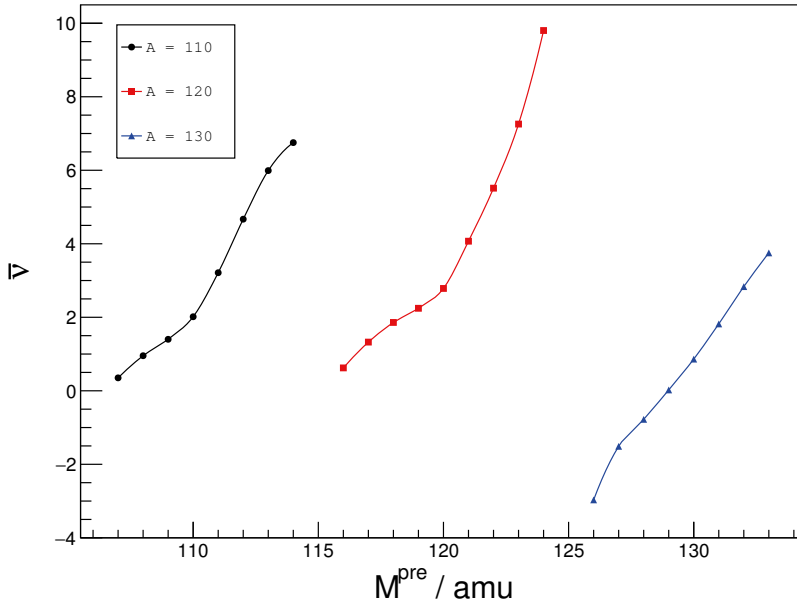


Figure 7.16. Calculated values of M^{pre} and \bar{v} shows a clear correlation when one observes events from different isobaric chains separately.

a mass slightly lower than the mass of symmetric fission. Since the mass yield is steeply sloped in this region, $\bar{v}(M^{\text{pre}})$ will predominantly be formed by events that has overestimated masses, i.e. lower true masses. Since an overestimated M^{pre} is coupled to an overestimated neutron multiplicity, the overall average is also overestimated. The effect is mirrored at the other side of symmetry, and also significant at each of the tails of the mass distribution. The complete effect of this is an exaggerated saw tooth shape depicted in fig. 7.15, which bears large similarities with the experimental results from VERDI.

It is at this point interesting to look into exactly how previous experiment-alists have dealt with the effects of neutron emission. While the broadening effect usually is recognised, the distortion it can cause on, e.g. \bar{v} , has not been realised. Nishio et al. [93] measured $^{239}\text{Pu}(n_{\text{th}},f)$ with the 2E-2v method but did not give the velocity assumption much attention and did not even included in the error estimation. In a paper by Brinkmann et al. [100] the errors introduced by neglecting neutron evaporation is commented as “possibly serious” but since $\bar{v}(M^{\text{pre}})$ is never presented in the paper the correlation effect was never observed. Müller et al. gives a very detailed error analysis a 2E-2v measurement of $^{235}\text{U}(n_{\text{th}},f)$ [92] where a mass uncertainty of 0.325 amu was attributed to the neutron emission. In their work they presented a plot of the $\bar{v}(M^{\text{pre}})$ and indeed were there indications of an over- and undershoot for $\bar{v}(M^{\text{pre}})$ in the

symmetry region. However, it was interpreted as a “better mass resolution” (FIG. 11 and 12 in ref. [92]). Since they never mentioned any correction for the found correlation problem, I must assume that their results were affected by it, and need to be corrected.

I will now derive a correction procedure by deconvoluting the resulting $\bar{v}(M^{\text{pre}})$ from the 2E-2v method. It is a simple correction that can be applied also to previously measured data and it does not rely on any input data except the measured (uncorrected) pre-neutron mass distribution and neutron multiplicity.

The algorithm works with binned data, preferably with much smaller bins than the experimental resolution. In my implementation, a bin width of 0.1 amu was used. First I construct a response matrix R relating the actual pre-neutron mass M^c with the obtained measured pre-neutron mass M^m such that

$$M_i^m = \sum_j R_{ij} M_j^c. \quad (7.24)$$

The neutron emission appear as a broadening of the mass resolution which can be kinematically estimated using the preliminary $\bar{v}(M^{\text{pre}})$. In the case of $^{252}\text{Cf}(sf)$ the standard deviation due to neutron emission was on average 0.8 amu. The mass dependant estimates are depicted in fig. 7.17, where one sees how the broadening follows the shape of the *total* neutron multiplicity since *both* velocities affect M^{pre} (eq. 7.14). The response from each true mass M^c was modelled by a gaussian centred on M^c with a mass dependent width according to fig. 7.17. The mass spectrum is taken into account by weighting each matrix element R_{ij} with the yield $Y(M_j^c)$.

To express the inverse relationship,

$$M_j^c = \sum_i R_{ij} M_i^m. \quad (7.25)$$

it was assumed that the transpose of R could approximate R^{-1} , even though R is not necessarily strictly orthogonal.

I find the correction formula by expressing the actual \bar{v}^c ,

$$\bar{v}_j^c = \frac{1}{m_n} (M_j^c - M_j^{\text{post}}) = \frac{1}{m_n} \sum_i R_{ij} (M_i^m - (M_i^{\text{post}} + \Delta M_{ij})), \quad (7.26)$$

where I have used eq. 7.25 to rewrite M_j^c , and ΔM_{ij} is just the distance between the bins i and j in mass units. Since $\bar{v}_i^m = (M_i^m - M_i^{\text{post}})/m_n$, this can be written

$$\bar{v}_j^c = \sum_i R_{ij} \left(\bar{v}_i^m - \frac{\Delta M_{ij}}{m_n} \right). \quad (7.27)$$

This rather crude correction method reproduces the true $\bar{v}(M^{\text{pre}})$ well. Figure 7.18 shows the resulting corrected $\bar{v}(M^{\text{pre}})$. The total average neutron

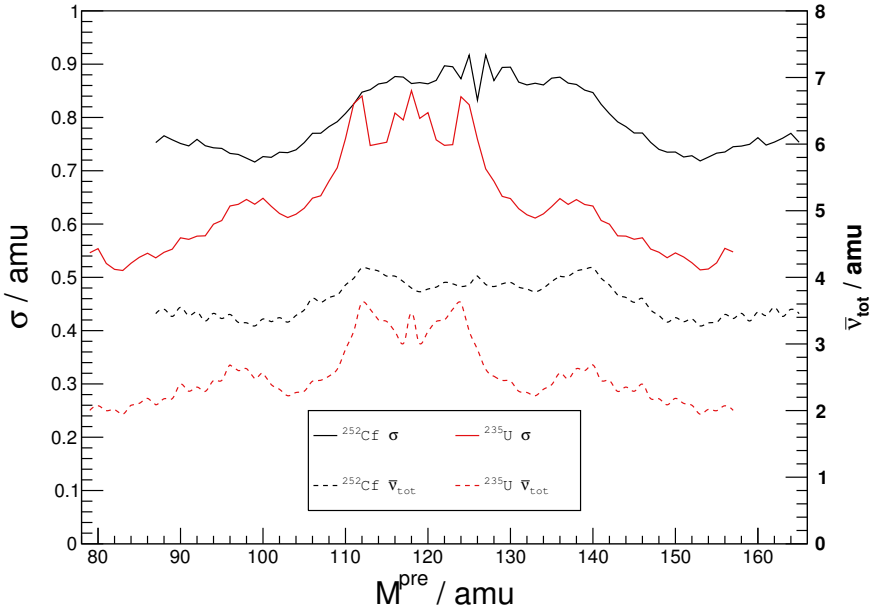


Figure 7.17. Standard deviations of the mass broadening due to neutron emission, for $^{252}\text{Cf}(sf)$ and $^{235}\text{U}(n,f)$, respectively. The total average neutron multiplicity $\bar{\nu}_{\text{tot}}$ is plotted as a reference.

multiplicity is conserved, but a smearing effect is present, leaving some structures in the synthetic $\bar{\nu}(M^{\text{pre}})$ unresolved.

Regarding the previously mentioned results from Müller et al., the lower neutron multiplicity of $^{235}\text{U}(n_{\text{th}},f)$ compared to $^{252}\text{Cf}(sf)$, makes the exaggeration of $\bar{\nu}(M^{\text{pre}})$ less severe, but I observed the same trend of over- and undershoots by running our simulation also for the $^{235}\text{U}(n_{\text{th}},f)$ case (fig. 7.19). The synthetic $\bar{\nu}$ generated by the GEF code shows much more structure than one sees in experimental data, but this makes it an even better test to determine how much of the structure in the synthetic data the correction method reproduces.

In both figs. 7.18 and 7.19 the mass yield was added as a reference. One can easily see how the correction is the largest where the mass yield changes the most between neighbouring masses.

7.7.6 Detection efficiency

Without neutron emission, the detection of one FP would also result in a detection of the complementary FP, as long as one is dealing with spontaneous fission. For the overwhelming majority of the $^{252}\text{Cf}(sf)$ events one or more neutrons will be emitted, and the higher the multiplicity the larger risk it is that

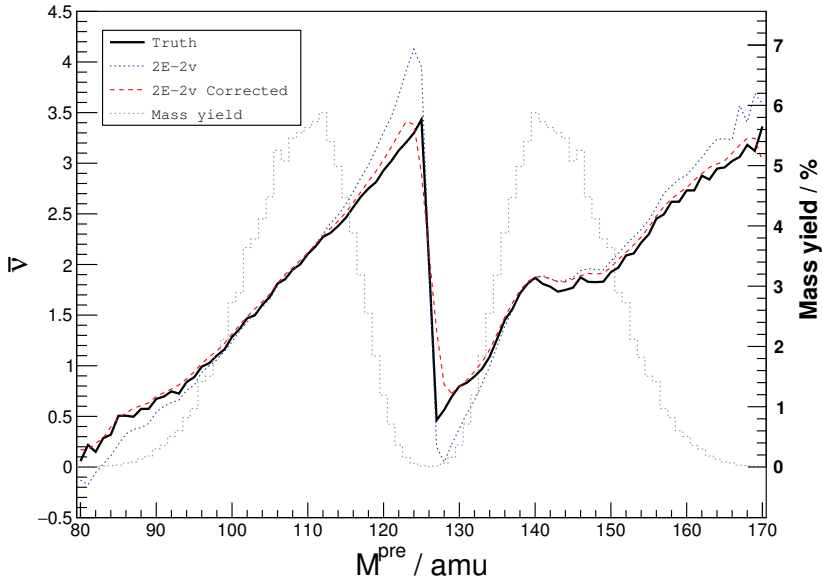


Figure 7.18. The corrected $\bar{\nu}(M^{\text{pre}})$ from $^{252}\text{Cf}(sf)$ shows signs of smearing, but reproduces the synthetic data well apart from that. The ‘true’ $\bar{\nu}(M^{\text{pre}})$, the uncorrected $\bar{\nu}(M^{\text{pre}})$ and the mass yield are shown as references.

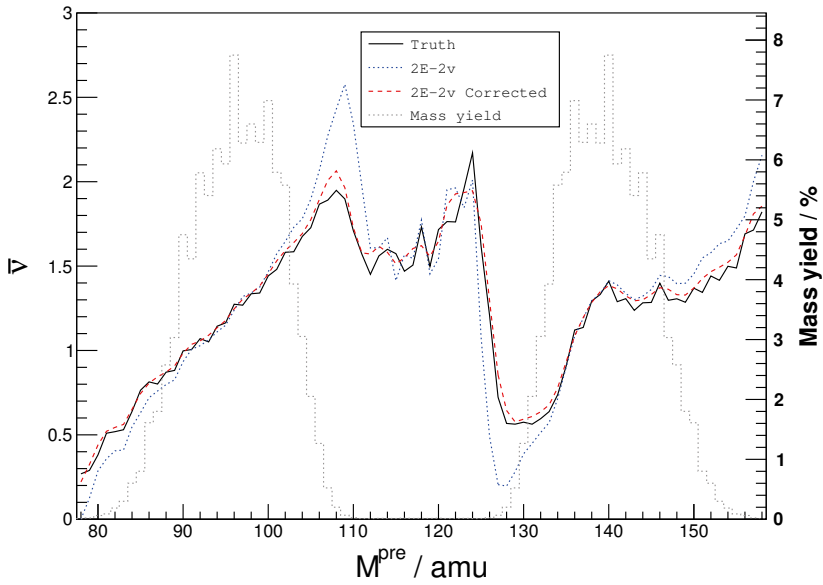


Figure 7.19. The correction method behaves the same way applied to $\bar{\nu}(M^{\text{pre}})$ from $^{235}\text{U}(n_{\text{th}},f)$ as when it is applied to $\bar{\nu}(M^{\text{pre}})$ from $^{252}\text{Cf}(sf)$. The ‘true’ $\bar{\nu}(M^{\text{pre}})$, the uncorrected $\bar{\nu}(M^{\text{pre}})$ and the mass yield are shown as references.

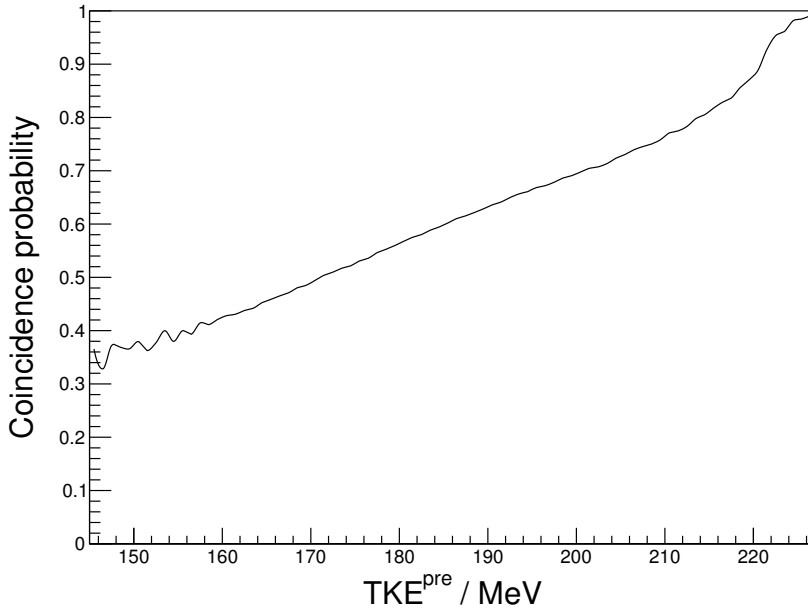


Figure 7.20. The simulation shows that the detection efficiency is strongly dependent on TKE^{pre}

not both FPs will be detected in coincidence. The effect the detector efficiency might have on the observables was investigated by calculating the coincidence probability for each event as outlined in section 7.6.

I explained previously in section 7.7.4 how the average total neutron multiplicity is inversely proportional to the TKE^{pre} . Not surprisingly, one sees in fig. 7.20 a much lower detection efficiency, around 40 %, for events with low TKE^{pre} while it reaches more or less 100 % for high TKE^{pre} .

This bias for events with low neutron multiplicity will distort the shape of some distributions which is demonstrated in fig. 7.21. The mass distributions are not greatly affected, since each mass can be emitted with an energy sampled from a broad energy distribution. Although, some of the structure due to the proton-neutron ratio start to wash out.

The energy distributions however, shift toward higher energies since high energy events are favoured. It is therefore important that the energy calibration is performed without a coincidence condition, or the wrong peak positions would be obtained.

Even though the mass distributions are less affected, the $\bar{\nu}(M^{\text{pre}})$ will be generally slightly underestimated under coincidence conditions, especially where the neutron multiplicity is the highest (see fig. 7.22).

The experimental data collected with VERDI exhibits an instrumental asymmetry, which is not explained by the efficiency due to neutron emission. It only

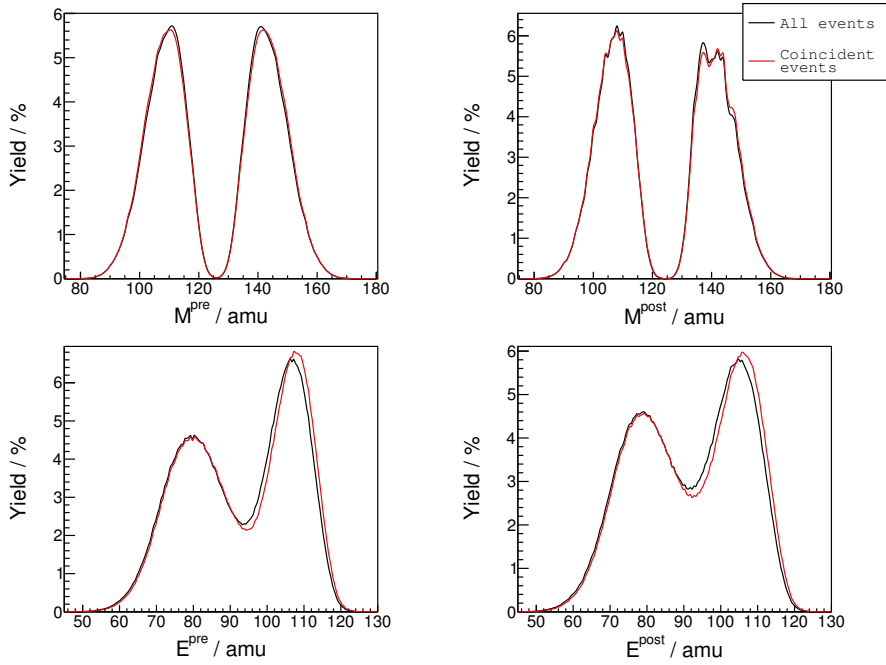


Figure 7.21. The simulated effect of detection efficiency for a few different one dimensional distributions.

affects coincident events. When no coincidence requirement is applied both sides show a 1 : 1 ratio of light versus heavy FPs. When observing coincident events, the ratio between light and heavy FPs is approximately 47 : 53 on one side. Whereas the ratio is inverted when observing the other side.

Since it only affects the coincident events, it might be due to some scattering effect increasing the deviation from collinearity. The scattering in the acceleration and mirror grids could be mass dependant but the grids are setup symmetrically and would not affect the sides differently.

The only intentional asymmetry in the VERDI setup is the target, which has a backing and a deposit side. It was theorised that the increased angular scattering of heavy fragments on the backing side of the target could cause this asymmetry. The angular straggling from SRIM [83] was used to estimate this effect. Despite that this indeed caused an asymmetry, its magnitude was at least a factor of ten too small even in the most extreme cases. Alas, this discrepancy is still unexplained.

However, since the detection efficiency seems not to be affected as long as no coincidence requirement is put on the data, the energy calibration is still ok and will not be affected by the E^{post} -shift seen in fig. 7.21. All the experimental results presented here has been symmetrised, i.e., the results from each of the sides has been added together, thus eliminating the asymmetry.

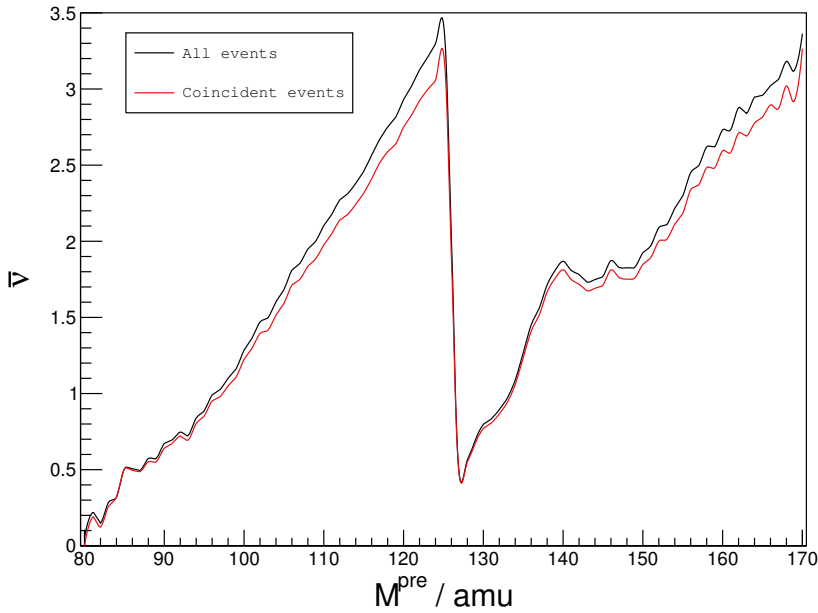


Figure 7.22. The detection efficiency has only a minor effect on $\bar{v}(M^{\text{pre}})$ but leads to a systematic underestimation, especially around the maximum and for heavy fragments.

7.7.7 Ternary fission

By looking at the non-coincident events it is possible to study ternary fission with the VERDI setup. Although some data was taken for this purpose, no detailed analysis has been performed on it yet. In addition to the complex energy and PDT calibrations, the MCP efficiency for particles lighter than typical FPs also needs more attention before any proper results can be obtained.

For demonstrating purposes, I made a simple polynomial energy calibration based on the detected ternary α -particles. The measured velocity has not been corrected for PDT in any way. Figure 7.23 shows several ternary particle species separated in the energy versus velocity plot. In addition to the numerous α -particles, one can distinguish tritons and ^6He clearly. There is also a clear contribution of sputtered nickel from the target backing. At least three other particle species are present but no clear identification could be made without better calibration of both timing and energy. Once the setup is fully calibrated, the ternary fission measurements could be revisited.

7.8 The future and unresolved issues

The PDT parametrisation in eq. 7.23 performed very well under ideal simulated circumstances, but was hampered when it was applied to real data. This

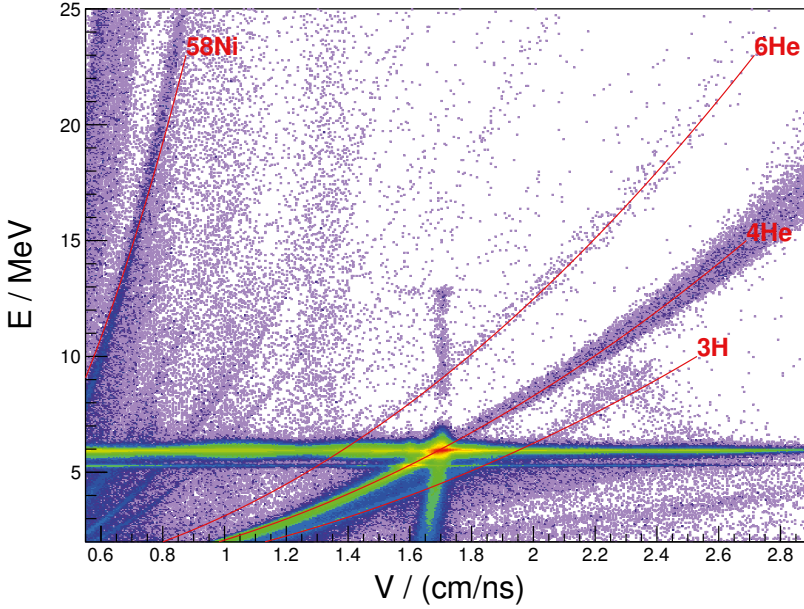


Figure 7.23. Ternary particles detected by VERDI. The energy calibration is only approximate. The solid lines represent the energy calculated using the measured velocities and the respective particle masses.

happened because the PDT from the 2E method was used. VERDI is therefore in need of either an independent characterisation of all its silicon detectors, or a working theoretical model of the PDT mass and energy dependence.

One could, for example, take the expression given by Bohne et al. and combine most of the constants:

$$PDT = C_1 \frac{\bar{Z}^2}{M^{\text{post}}(d - x)} \exp\left(-C_2 \frac{E^{\text{post}}}{M^{\text{post}}}\right), \quad (7.28)$$

where \bar{Z} is the effective charge, d the depletion depth and x the median depth of the created electron-hole pairs. C_1 and C_2 are the two remaining parameters that could be fit to the VERDI detector characteristics. The parametrisation of Bohne et al. has previously turned out to be difficult to adapt to new sets of silicon detectors [100], but treating C_1 and C_2 as free parameters might remedy this if the functional form is sound. A first attempt to do this for VERDI was performed, but was unsuccessful as it was found that every single detector would need different parameters and the lack of reference PDT made it difficult to determine the parameters. The model also showed a heavy dependency of how the average charge was calculated, indicating that the expression might not be very general. It seems a detailed characterisation of the detectors will be needed for this to work.

A longer flight path would effectively decrease the importance of the PDT correction, but also further reduce the detection efficiency, which is already causing trouble since it was shown to be strongly dependent on neutron emission (fig. 7.20). Increasing the size of the silicon detectors could remedy this but only if they keep their good timing properties. If silicon strip detectors could provide good enough timing resolution, it would be an interesting choice also due to the position sensitivity. The detection efficiency will see even larger challenges once VERDI measures neutron-induced fission, since the neutron momentum transfer from the primary neutron will affect the angle between the fragments in an energy dependent manner.

Overall the VERDI project is making progress, even though there are several improvements needed, especially for the PDT correction procedure. The recent scrutiny of the analysis procedure identified a flaw, overlooked by many previous experimentalists. It can be corrected by a simple deconvolution procedure, but with some smearing as a side effect. Considering that, in addition to VERDI, several 2E-2v projects [101–103] are under development around the world, it is important to show that it is possible to obtain correct independent data. Next, one needs to determine how much and in what way this limits the obtainable resolution of these upcoming experiments.

When the PDT can be well estimated, the detection efficiency has been improved, and the intrinsic problems of the 2E-2v method have been overcome, the next step for VERDI is to confirm all calibrations and corrections against a new fissioning system. Thermal neutron-induced fission of ^{235}U is also a well known system and would serve as a cross-check of the calibrations achieved with $^{252}\text{Cf}(sf)$. Once a successful measurement of $^{235}\text{U}(n_{\text{th}},f)$ is achieved, many systems, including neutron-induced fission at higher energies, are waiting.

8. Simulated ion stopping at IGISOL

*Finland, Finland, Finland.
The country where I want to be,
pony trekking or camping, or just
watching TV.*

— Michael Palin

As mentioned in section 4.3, yield measurements using the IGISOL method relies on the measured isotope yield to be compared to the yield of another isotope. That isotope must exhibit the same stopping, extraction, and transport efficiency through out the whole system, from the fission moment until the last capture and detection in the Penning trap. In order to compare yields of non-neighbouring isotopes there must be a connection through several relative measurements.

Approximate efficiencies are known, partly based on the large experience gathered at IGISOL, but systematic studies of them are lacking. Knowing them better could allow for a better understanding of the experiments, and possibly identification of problems or improvements to the method. One possible improvement could be optimising the efficiencies in order to study more low-yield FPs.

At IGISOL experiments are conducted both for measuring fission yields [104] but also for the production and study of exotic nuclei. Most previous measurements at IGISOL up until now, has been using proton-induced fission [45]. Neutron-induced fission changes the yield significantly, especially for neutron-rich FPs. Previous experiments, using neutron-induced fission, reported a shift of the average atomic charge value by 0.88, compared to the proton-induced case [105]. In fig. 8.1 it is demonstrated how the predicted neutron-induced yields for different tin isotopes compares to the proton-induced yields. These tin nuclei in particular are important to understand the r -process [106], a mechanism to create nuclei heavier than iron through cosmological nucleosynthesis.

For the studies of the proton-induced case, which were published in 2015 [107], I wrote the simulation software and assisted the analysis. When it comes to the neutron-induced studies, I developed the simulation software and performed the analysis.

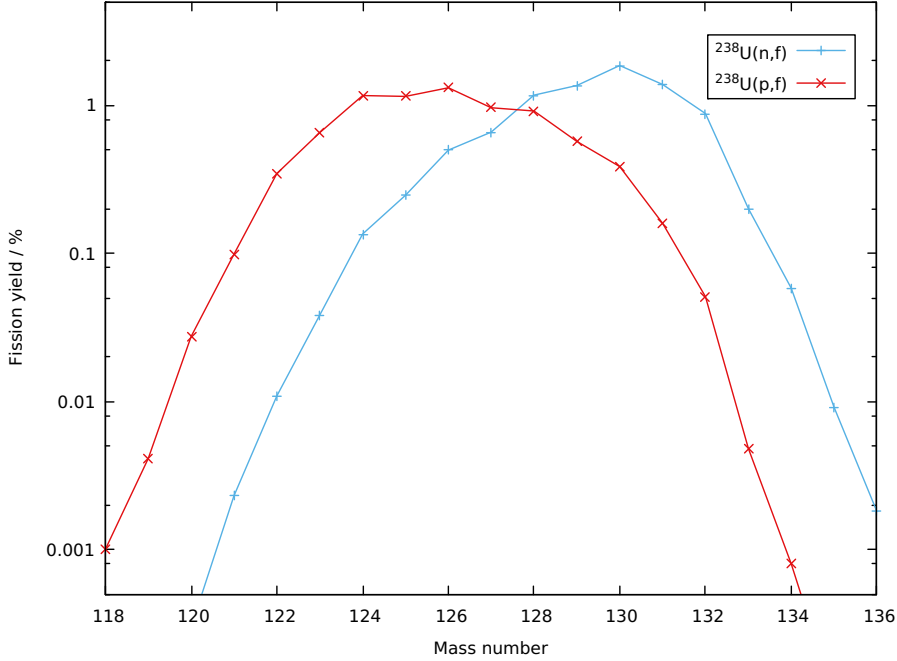


Figure 8.1. Estimates of the yields of different tin isotopes from neutron- and proton-induced fission of ^{238}U . The yields were calculated using GEF [16] for 12 MeV neutron and 25 MeV protons, respectively.

8.1 Ion guide for proton-induced fission

8.1.1 Experimental setup

The experimental setup for this experiment is rather simple and is depicted in fig. 8.2. The proton beam hits a natural uranium target at a 7° angle. Only a few per cent of the FPs will escape the 15 mg/cm^2 thick target into the 200 Torr helium stopping gas filling the chamber. In order to shield the rest of the ion guide from the plasma induced by the proton beam a thin (1 mg/cm^2) nickel foil is separating the target from the rest of the chamber volume. Only the FPs that pass through the nickel foil have a chance to be transported by the gas and be accelerated into the rest of the IGISOL setup (see section 4.3).

8.1.2 Simulation setup

In the simulation we neglected the beam attenuation inside the target, since protons are deeply penetrative particles. That means that the probability of having a fission event is constant over the whole target volume as long as the beam is completely illuminating the target. We therefore completely neglected the primary particles and started the simulation by creating heavy ions of

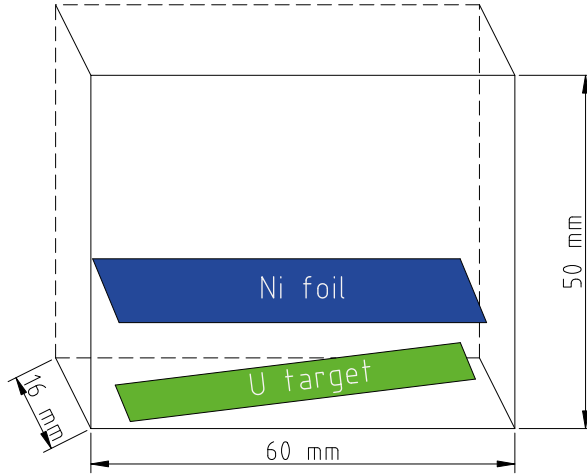


Figure 8.2. The setup for proton induced fission yield measurements. The neutrons enter from the left impinging on the tilted uranium target. Only the FPs reaching the volume above the nickel foil might get evacuated by the gas flow.

specific isotopes and energies at random positions in the target. The velocity vectors were also randomised but only in the hemisphere facing the nickel foil and the gas exit.

Fourteen isotopes were chosen over a large mass range, $A = 85\text{--}150$, and for each mass number A , the most probable atomic number Z was chosen. Each of these isotopes were simulated with five characteristic energies, based on mass specific energy distributions obtained from GEF [16] calculations. They were defined by the 20, 50 and 100 % distribution heights, and named ‘minimum’, ‘low’, ‘mean’, ‘high’ and ‘maximum’ (see fig. 8.3). For each isotope-energy combination 1×10^7 ions were simulated.

Much care was taken to use small enough steps while simulating the ion stopping. The ions lose a lot of energy over short distances in solid materials, and we could see discrete features in the distributions that disappeared if sufficiently low step lengths were used. In the end we determined that a 0.5 nm step length in the uranium target was enough (with some margin) and in the less dense gas we used a 1 μm step length.

We also detected that some of the anomalies that we had seen were due to the Geant4 process `G4hMultiplescattering` giving unphysical results. This class was therefore disabled, after a careful evaluation making sure that the stopping ranges were not affected by leaving this model out. Without these anomalies the stopping ranges of the ions more closely resembled the ones predicted by the commonly used software SRIM [83]. The discussion and

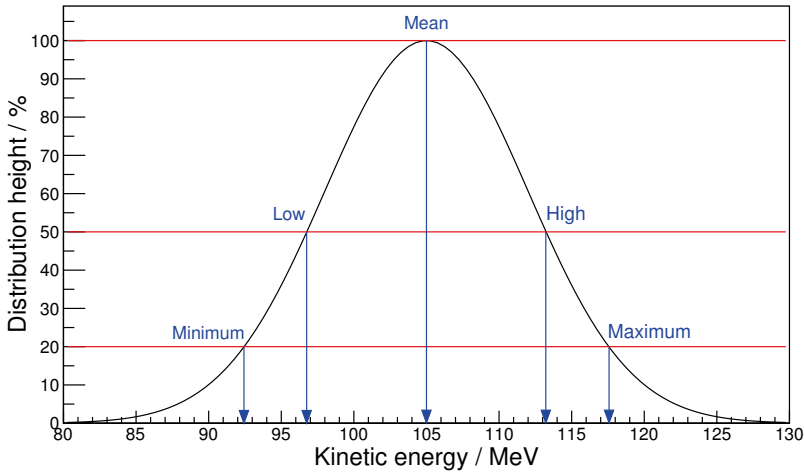


Figure 8.3. Five different energies were simulated for each chosen mass number. The energies were determined based on the energy distribution for that particular mass number. The chosen energies corresponds to 20, 50 and 100 % of the distribution height.

technical details regarding the steps lengths and `G4hMultiplescattering` were published at length in a non-peer-reviewed article online [108].

8.1.3 Main results

Absolute numbers can be tricky in simulation studies and this was no exception. Modelling of heavy ion stopping is difficult and the results may vary with the used model. We compared the amount of ions ending up in the volume behind the nickel foil estimated by both the Geant4 software and SRIM, respectively. We found that the predictions were quite different. The Geant4 simulations predicted 0.75 % while SRIM predicted 0.45 %.

However, the relative amount of stopped ions when comparing different isotopes are very weakly dependent on the exact strength of the stopping power. By scaling the stopping power by $\pm 10\%$ and comparing the number of stopped ions we saw a difference of less than 10 % between the two extremes. From this we also argue that the uncertainty in the predicted number of stopped ions are in the same order of magnitude.

The main result of this study is that the mass dependence of the stopping efficiency varied by 5 % at most (see figs. 8.4 and 8.5). When comparing yields of neighbouring ion species the differences are negligible, confirming that the IGISOL methodology is sound in that regard. We could also predict where in the volume the ions ended up (fig. 8.6), which could be interesting for optimising the chamber size and the gas flow.

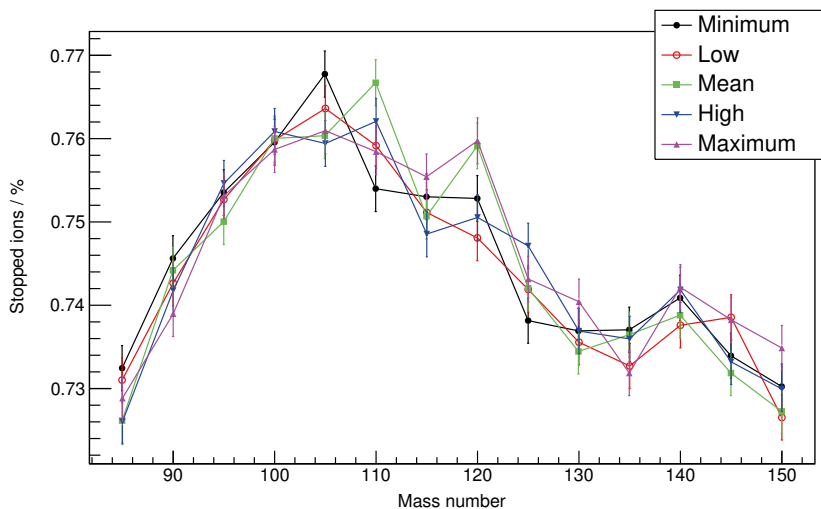


Figure 8.4. Percent of the simulated ions that stop in the area behind the nickel foil, as a function of mass number. The different curves correspond to the energies defined in fig. 8.3.

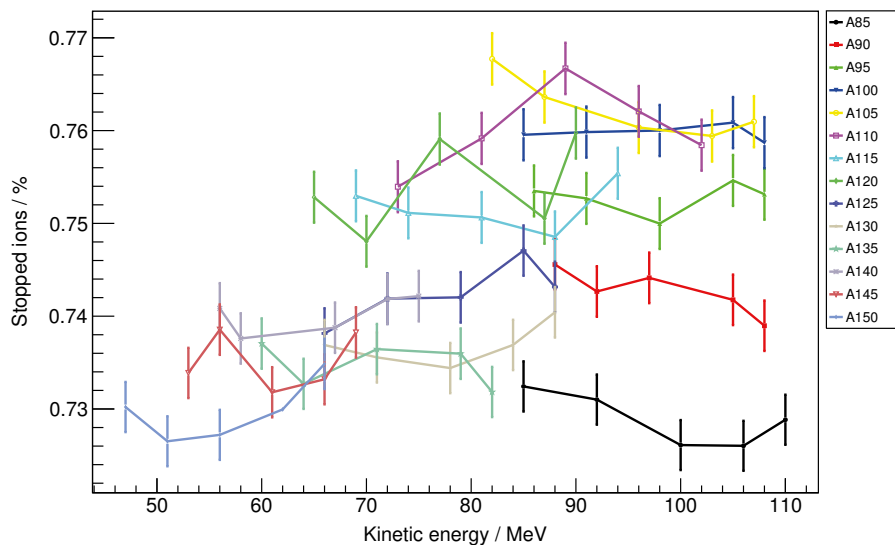


Figure 8.5. Percent of the simulated ions that stop in the area behind the nickel foil, as a function of initial kinetic energy.

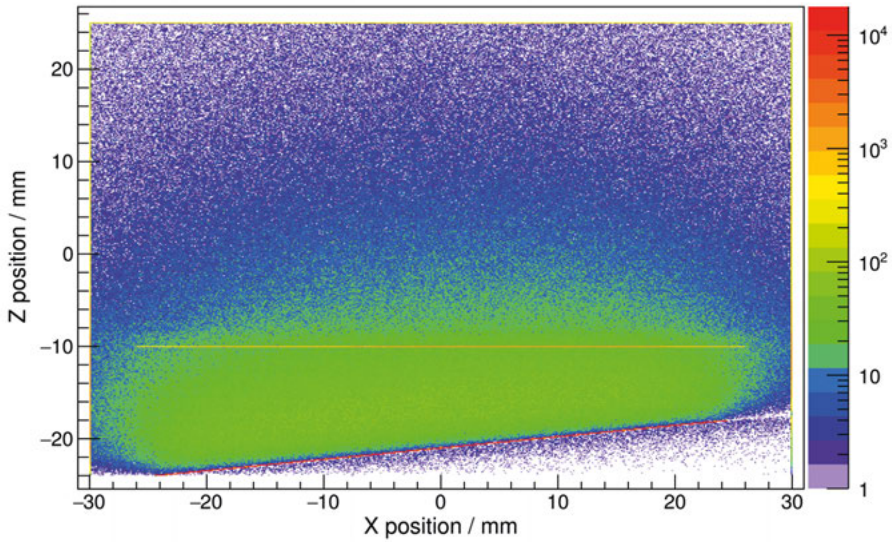


Figure 8.6. Map of where the simulated ions stops. Most stop in, or close to, the solid materials, either the target or the nickel foil.

We also investigated the target thickness. In a thick target the energy distributions of the FPs do not affect the stopping efficiency, since the small energy interval that allow a certain isotope to stop in the designated gas volume, corresponds to a certain depth in the target. A slightly higher energy will just select ions of a slightly deeper depth in the target. If the target is too thin, the stopping efficiency of light isotopes starts to drop (see fig. 8.7).

Similarly we investigated the nickel foil thickness and concluded that a too thick foil will greatly enhance the mass dependence of the stopping efficiency (see fig. 8.8).

The conclusion of this study was that there were some small mass dependence in the stopping efficiency. Much of it was counteracted by different properties of the setup, e.g., the nickel foil thickness, which counter acted the already small mass dependence.

8.2 Ion guide for neutron-induced fission

This set of simulations is a continuation of the proton-induced simulation case, but both the geometry and the methodology were changed. We now decided to take things one step further and also simulate the incoming flux, which allowed me to calculate absolute numbers of the number of stopped ions as a function of integrated primary beam current. This time the incoming flux consist of neutrons which are produced by the primary proton beam. The

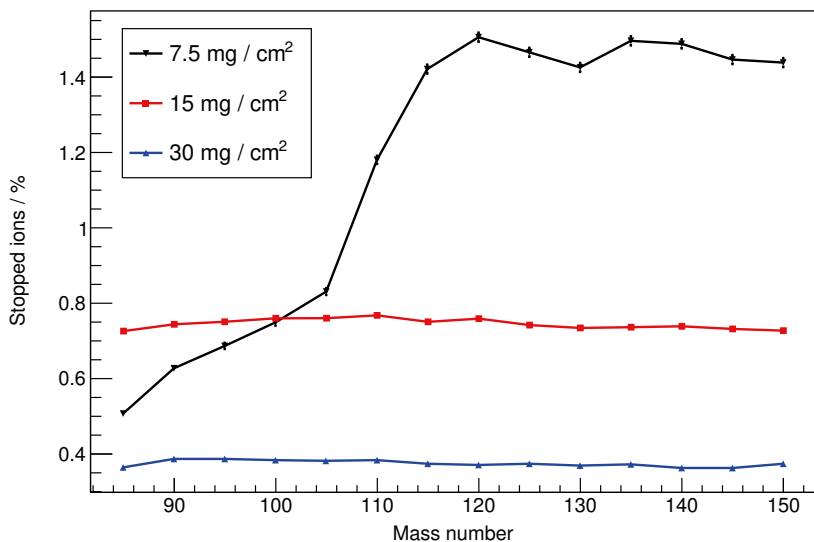


Figure 8.7. The number of stopped ions depend on the target thickness. A too thin target will often fail to degrade the light fragments' energies enough to be stopped in the evacuated gas.

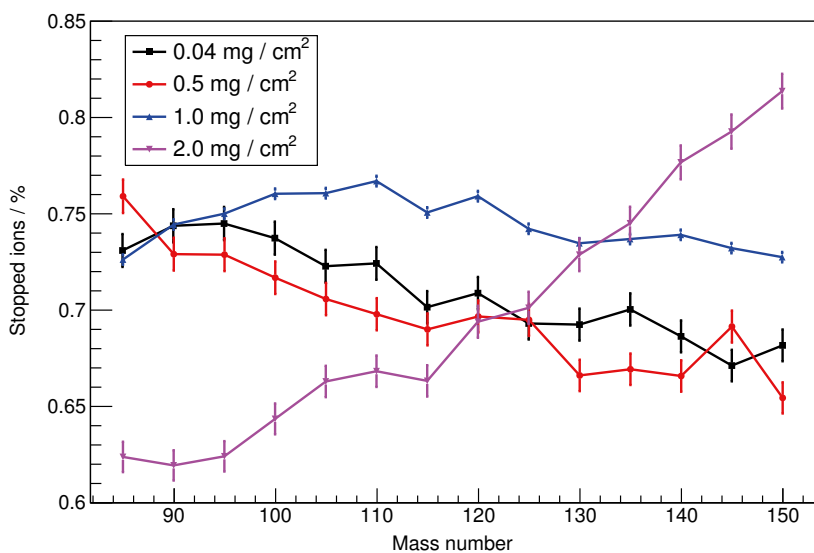


Figure 8.8. The nickel foil protects against plasma created in the helium gas by the primary proton beam. If it is too thick, a clear mass dependence develops in the ion stopping efficiency.

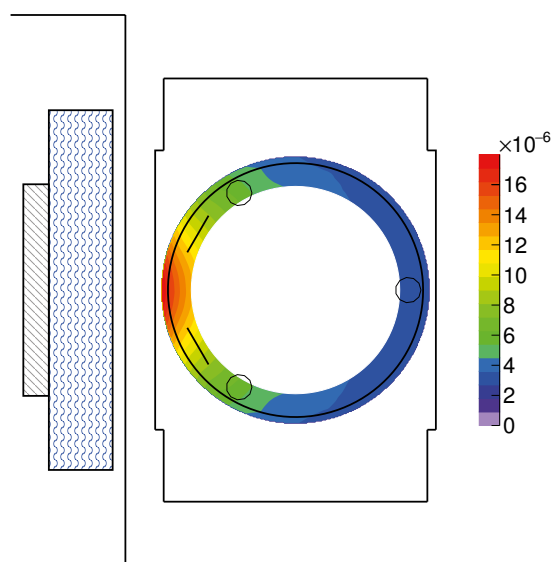


Figure 8.9. The neutron flux in $\text{n}/(\text{cm}^2 \mu\text{C s})$ calculated by MCNPX, on top of a schematic of the ion guide. The flux was only recorded in a cylindrical shell enclosing the target positions. To the left of the ion guide is the neutron source. The beryllium target (grey striped pattern) is cooled by the water (blue wave pattern).

neutron production was simulated separately by A. Solders, while my Geant4 software took care of the FP transport simulation.

In December 2016 a yield measurement was performed using this setup for neutron induced fission, which allows me to make some comparison between simulation and reality.

8.2.1 The neutron source

To produce neutrons, a 30 MeV proton beam impinge on a water-cooled beryllium target. The neutron production target is thick (5 mm) but designed to allow the primary beam to go through and deposit the last of its energy in the cooling water (pressurised to 7 bar), on the back side of the target. This reduces wear on the target since there is less hydrogen build-up in the beryllium, but also activates the cooling water, thus requiring a closed circuit. It was later decided to add another centimetre of beryllium in order to reduce the activation. Behind the cooling water, the ion guide with one or several uranium targets followed, with only a thin (3 mm) aluminium window in between, in order to make the best use of the neutron flux [46, 109].

The neutron converter has been simulated using MCNPX 2.5.0 [110] and the neutron flux was recorded in a 7 mm thick cylindrical shell, enclosing all regions where targets were positioned. The calculated neutron flux integrated over all energies is depicted in fig. 8.9 on top of a schematic of the ion guide. The simulated geometry included the ion guide but not the uranium targets inside since the attenuation of the neutron flux in the uranium targets is negligible. It can easily be shown that the attenuation can be neglected since the mass attenuation coefficient is

$$\mu_m = \sigma N_A / M_U \approx 2.5 \frac{\text{cm}^2}{\text{g}}, \quad (8.1)$$

where $\sigma \approx 1 \text{ b}$ is the cross section, N_A Avogadro's number and M_U the molar mass of natural uranium. The standard targets are 14 mg/cm^2 thick leaving us with an attenuation in the order of 1×10^{-5} .

The flux was acquired in 1 MeV bins from 1 to 30 MeV and exported to text files that were later read by the main simulation software.

8.2.2 The ion guide

The chamber where the FPs are produced and collected is called the ion guide. It is gas-filled and the main part of it is cylindrical with a length of about 70 mm and a diameter of 60 mm. As in the proton-induced case the gas is supposed to stop the ions so that they can be extracted from the ion guide by the helium gas flow. The nominal gas pressure is 200 mbar, but in the experiment conducted in December it was increased to 400 mbar. A 3D rendering of the standard reference setup [47] is depicted in fig. 8.10.

Three different versions of the setup were implemented and investigated, each depicted as cross-sectional drawings in figs. 8.11a to 8.11c. The default setup mirrors the experimental setup used during measurements at the IGISOL facility in December 2016. It features two uranium targets close to the neutron production, in order to maximise the neutron flux. These targets are $10 \text{ mm} \times 50 \text{ mm}$ with a thickness of 15 mg/cm^2 . There is also an implantation foil in the back made out of titanium.

The implantation foil makes it possible for us to compare the simulations to the experiment in December 2016 by analysis the γ -spectrum. This is however still in progress and results are pending. Nevertheless, doing so might provide further experimental verification of the simulation's validity.

Another option is to simulate six targets of the same dimension as the previous mentioned, each fixed on one of the hexagonal sides of the ion guide target holder. In this case the titanium foil is not used. The last option is to remove the target holder and replace it with two lock rings that holds a larger, $41 \text{ mm} \times 64 \text{ mm}$, and thicker, 21 mg/cm^2 , foil pressed against the cylindrical surface of the ion guide's inside, as close to the neutron source as possible. As

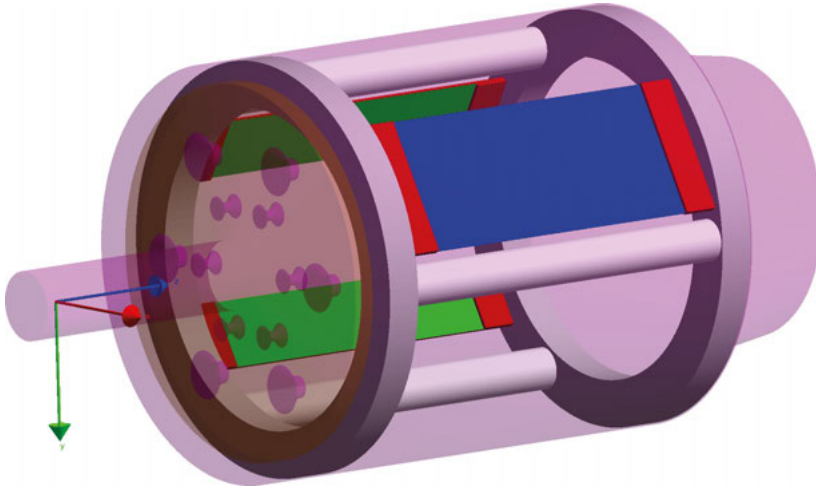


Figure 8.10. 3D rendering of one of the simulated geometries. The outer walls have been rendered transparent, and the gas inside was rendered translucent purple. Also the orange gas diffuser has been rendered translucent to improve visibility. The beam direction is perpendicular to the ion guide axis, along the x -axis (red arrow). The gas flow purging the ion guide is along the ion guide axis that coincides with the z -axis (blue arrow). The setup shown is the same that was used in the real measurements in December 2016 with two uranium targets (green) and one titanium foil in the back (blue).

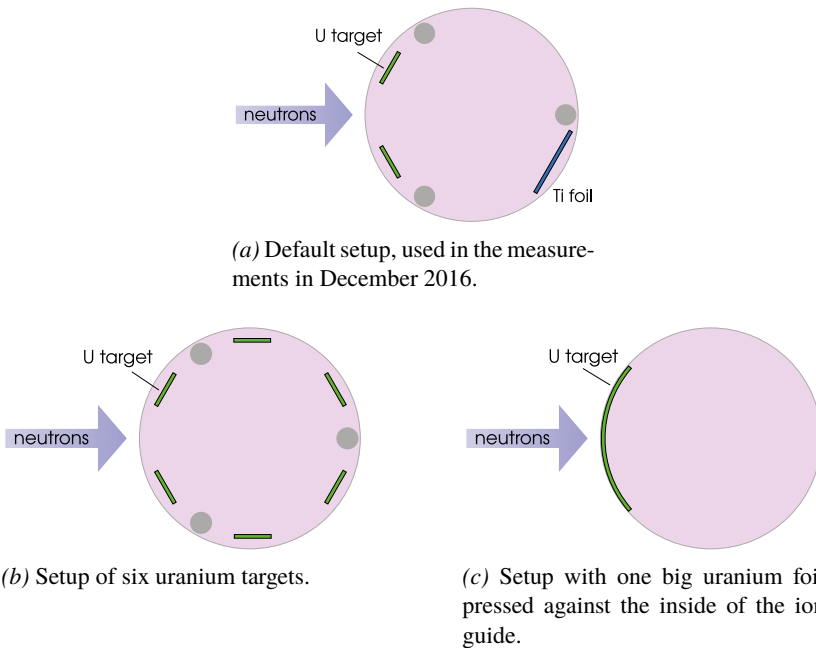


Figure 8.11. Cross sectional schematics of the target placement for the different setups. The gas flow goes out of the plane of the drawings.

the results will show, there is no benefit of the increased thickness of this target compared to the other ones, but it was what was available from the supplier.

In addition to the different geometries, the target thicknesses and the gas pressure inside the ion guide were also varied. A replacement for the standard Geant4 code that estimates the effective charge when ions are travelling through matter was also tested (see appendix A.1.3 for implementation details).

8.2.3 Ion stopping simulation

The main simulation was implemented in Geant4 [71] version 10.01-p03. The only physics relevant to include, was the one related to the slowing down of particles in matter. This was handled by the classes `G4ionIonisation` and `G4NuclearStopping`.

The primary particle in the simulation is a FP, sampled from an isotopic fission yield distribution. Its kinetic energy is sampled from an energy distribution for the corresponding isobar. Both distributions are calculated beforehand by the program GEF [16] for the $^{238}\text{U}(n,f)$ reaction at 1 MeV intervals from 0 to 30 MeV incoming neutron energies. The GEF output files were then parsed by the simulation software. Linear interpolations were made between data points when needed. The neutron energy was uniformly sampled from 0 to 30 MeV.

When both the particle species and kinetic energy were determined, the direction of the particle was sampled isotropically. The starting position, i.e. where the fission happened, is uniformly sampled within the complete target volume(s) of the simulation. One should note that only one FP is simulated per event, i.e., one fission per two Geant4 events on average. In each simulation 1×10^8 FPs were sampled and transported.

Since both the neutron energy and starting position were uniformly sampled, the results were weighted by the macroscopical cross section Σ as well as the neutron flux, ϕ , provided by the previously described MCNPX simulations (see section 8.2.1). The macroscopical cross section is given by:

$$\Sigma = \sigma \frac{N_A m_U}{M_U}, \quad (8.2)$$

where the microscopical cross section, σ , was taken from the ENDF/B-VII.1 evaluation [81], N_A stands for Avogadro's number, m_U is the total mass of target uranium and M_U is the molar mass of natural uranium. By also dividing the weighting factor, w , with the number of simulated events, N , one gets a final expression for the event weight:

$$w = \frac{2\phi\Sigma}{N}, \quad (8.3)$$

where the 2 takes into account that only one, not two, FP is simulated. Summing over all weights, after choosing appropriate units, produces the expected total

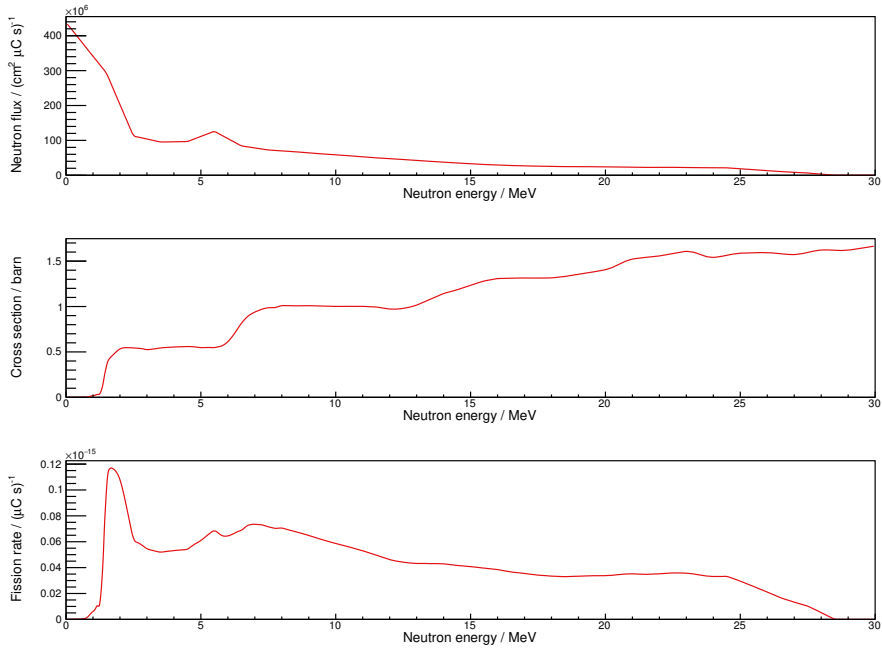


Figure 8.12. The average neutron flux, the fission cross section, and the average fission rate (the product of the two previous) as functions of the neutron energy.

number of produced ions per μC of integrated primary beam current. The average neutron flux, fission cross section and fission rate are depicted in fig. 8.12.

Since the only concern of the simulation is to determine where the ions stop, all secondary particles (mostly electrons) are immediately killed and not further simulated. The simulation results contain full information about the initial and final state of the ions.

8.2.4 Results

For easily referral I will start by defining the different setups that were simulated. The different geometries of the target(s) placement have already been described in fig. 8.11. The ‘standard’ geometry with two targets was further studied with modifications to the effective charge model, target thickness and gas pressure. From now on, I will refer to the simulations by the names provided below.

Sim I Default geometry (see fig. 8.11a) with a gas pressure of 200 mbar and the effective charge model from Geant4.

Sim II Same as **Sim I**, but with the effective charge model developed by Schiwietz and Grande [37] (see appendix A.1.3).

- Sim III** Same as **Sim I**, but with a 7.5 mg/cm^2 target thickness.
- Sim IV** Same as **Sim I**, but with a 150 mg/cm^2 target thickness.
- Sim V** Same as **Sim I**, but with a 400 mbar gas pressure.
- Sim VI** Six targets of the same type as in **Sim I** (see fig. 8.11b).
- Sim VII** A big target pressed against the ion guide wall (see fig. 8.11c).

For all the different simulations one can determine how many ions were stopped in the gas, as well as how many that escaped the target but ended up colliding into a wall, i.e. any solid material except for the targets. An ion that was not stopped in either the gas or a wall, never escaped the target. The total yield as well as the yields in the gas and walls, respectively, are collected in table 8.1. For **Sim I–Sim V**, one can also determine how many ions that were caught by the implantation foil.

8.2.4.1 Mass and effective charge dependence

Just as in the proton-induced case, the mass dependence in the stopped ion yields are small. In figs. 8.13 and 8.14 the mass and charge yields, respectively, are compared depending on where in the geometry the ions stopped.

In total, about 1.91 % of the generated ions in **Sim I** stop in the gas and have a chance of being evacuated to the IGISOL vacuum system. The light FPs have a slightly larger ratio of ions stopped in the gas, than the heavy ones, since the lower charge and higher kinetic energy allow more of them to escape the target. Naturally, there are also more light, than heavy, FPs hitting the walls since the effective thickness of the gas is not always enough to stop them. The highest ratio of ions stopped in the gas is found for the lowest mass numbers. Around $A = 80$ it reaches 2.09 %, while at $A = 160$ it is only 1.89 %. A similar pattern is found for the atomic charge distributions.

When measuring yields with the IGISOL technique, it mostly matters how large difference in this stopping efficiency one has for two neighbouring isotopes. The largest differences in the stopping ratio for two neighbouring mass

Table 8.1. *Yields of the produced and stopped ions for the different simulations, Sim I–Sim VII, given per μC of integrated primary beam current.*

Simulation	Generated	Ion yield	
		Stopped in gas	Stopped in walls
Sim I	3.104×10^4	5.934×10^2	9.897×10^3
Sim II	3.104×10^4	6.679×10^2	7.372×10^3
Sim III	1.552×10^4	3.569×10^2	9.357×10^3
Sim IV	3.104×10^5	5.981×10^2	9.984×10^3
Sim V	3.104×10^4	1.139×10^3	9.348×10^3
Sim VI	5.300×10^4	9.945×10^2	1.692×10^4
Sim VII	1.241×10^5	1.910×10^3	2.804×10^4

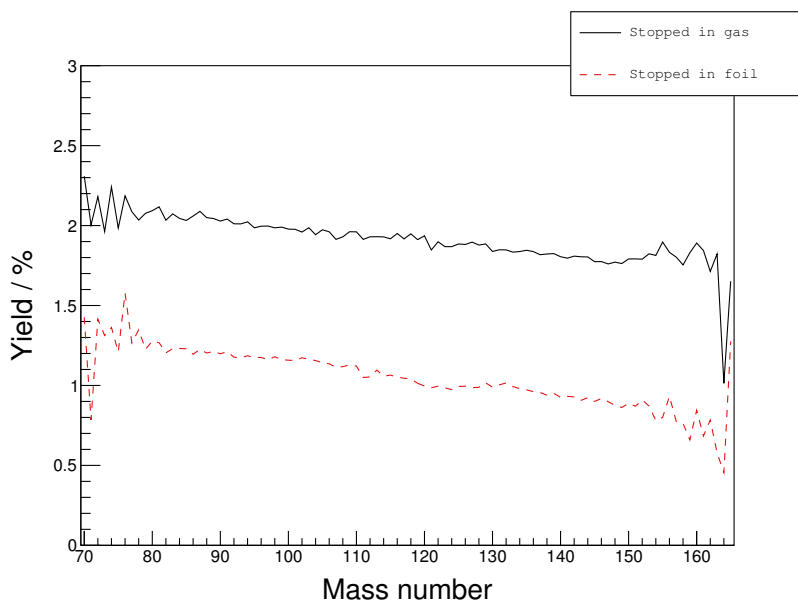


Figure 8.13. Mass yields of stopped ions from **Sim I**. The light FPs, that also have higher kinetic energies, are more likely to be stopped in the gas and the implantation foil, compared to the heavy FPs.

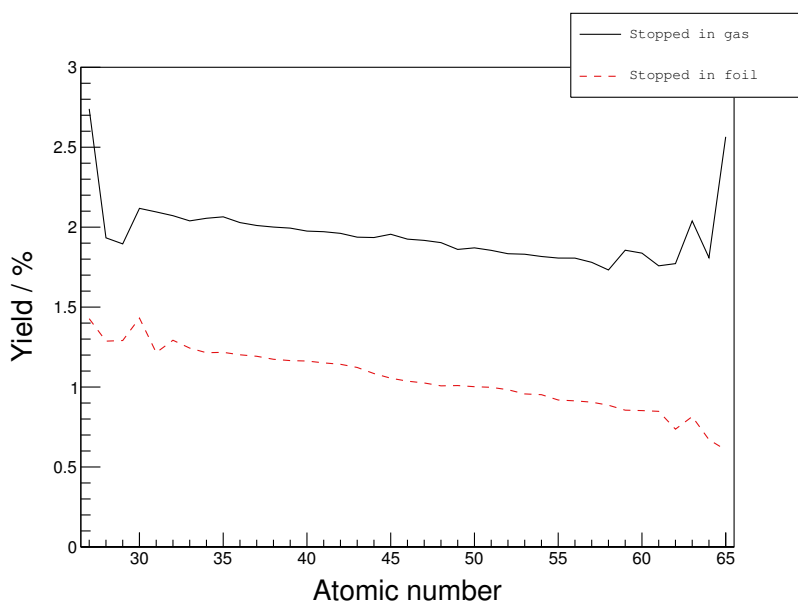


Figure 8.14. Charge yields of stopped ions from **Sim I**. The lightly elements, that also have higher kinetic energies, are more likely to be stopped in the gas and the implantation foil, compared to the FPs with high atomic numbers.

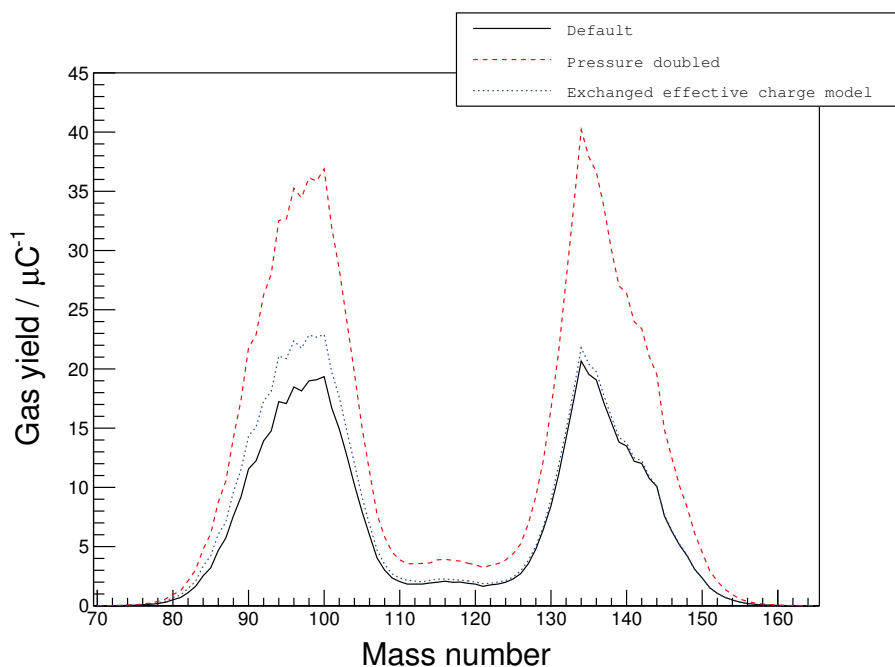


Figure 8.15. Yields of stopped ions in the gas from **Sim II** and **Sim V**. Exchanging the effective charge model mostly affect the light fragments and increases the mass dependence of the yield. The increase of yield when the pressure was doubled to 400 mbar was close to a factor of two over the whole mass region.

numbers are found for the heavy fragments, but no larger than 0.2 percentage points after disregarding statistical fluctuations.

Changing the effective charge model, as was done in **Sim II**, changes the stopping power. Overall the stopping power increased when the model from Schiwietz and Grande was used. The results from **Sim II** are similar to the ones in **Sim I**, but enlarges the differences between light and heavy FPs further (fig. 8.15). Nonetheless, examining table 8.1 reveals that even though less ions actually make it out of the target, the ratio that stop in the gas is greater due to the increased stopping power.

8.2.4.2 Target thickness and gas pressure

A thicker target will generate more FPs so it should always be at least as good as a thin one (if kept within reasonable limits). It might be a waste of precious material though, because if the FPs do not reach the outside of the target they will definitely not increase the yield of ions stopped in the gas.

In table 8.1 one can compare the results of increasing the target thickness tenfold, as was done in **Sim IV**. The number of ions in the gas are almost the same. On the other hand, one notices that the yield in the gas is almost cut in half in **Sim III**, while a similar number of ions as in **Sim I** still hit the walls.

This means that the thickness in **Sim I** is close to optimal. The yield does not increase as a thicker target is used and a thinner target will not be able to, in the same extent, degrade the energy of the most energetic ions, thereby making it possible for them to stop within the gas volume.

One way of making the ion guide facilitate a larger yield of ions stopped in the gas is to make the chamber bigger. However, there might be an easier way. One of the plots in fig. 8.15 represents the yield as the gas pressure is doubled and thereby effectively making the gas twice as thick. The numbers in table 8.1 shows that the yield in the gas is doubled, more ions are now stopped before they hit any of the walls. Furthermore, one concludes by comparing to the default case in fig. 8.15, that the increased pressure has not affected the mass dependence compared to the situation in **Sim I**. Higher pressure could be a good option for increasing the yield, as long as the differential pumping can keep a low enough pressure in the vacuum part of IGISOL. Currently, no higher pressure than 400 mbar is possible.

8.2.4.3 Target geometries

Only the setup of **Sim I** has up till today been experimentally tried. Although there were plans of realising also a target in the style of **Sim VII**. The current target holder already has space for up to six targets as in **Sim VI**. But as the numbers in table 8.1 show, the benefit of adding extra targets declines as the distance from the neutron source increases. This can also be seen by comparing fig. 8.16 to fig. 8.17, where the positions of the stopped ions in the gas are depicted. When all six targets holders are used, the relative number of events stopped in the gas originating from the middle and the back targets, are only 22 % and 19 %, respectively. This also shows the importance of centring the targets, because even though further away, the more centred back targets contributed almost as much as the middle targets.

The target in **Sim VII** has three major benefits compared to the standard setup in **Sim I**. Firstly, it has an area which is 2.6 times greater. Secondly, it is centred on the neutron beam where the flux is the highest. Lastly, it is as close as the ion guide allows to the neutron source. All of this combined, result in a 3.2 times higher yield of stopped ions in the gas for **Sim VII** compared to **Sim I**. In fig. 8.18 the spatial distribution of the stopped ions when using this bigger target is shown.

Even though there are clearly a higher concentration of stopped ions close to the targets in figs. 8.16 to 8.18, many of the ions traverses the whole chamber. In fig. 8.19 the cumulative distribution of stopped ions is plotted as a function of distance from the fission event. The distance is measured perpendicular to the target surface, which give us an estimate of how much free space is needed in front of each target to maximise the yield. Half the FPs are stopped within 14 mm of the target, while less than 80 % are stopped within 28 mm.

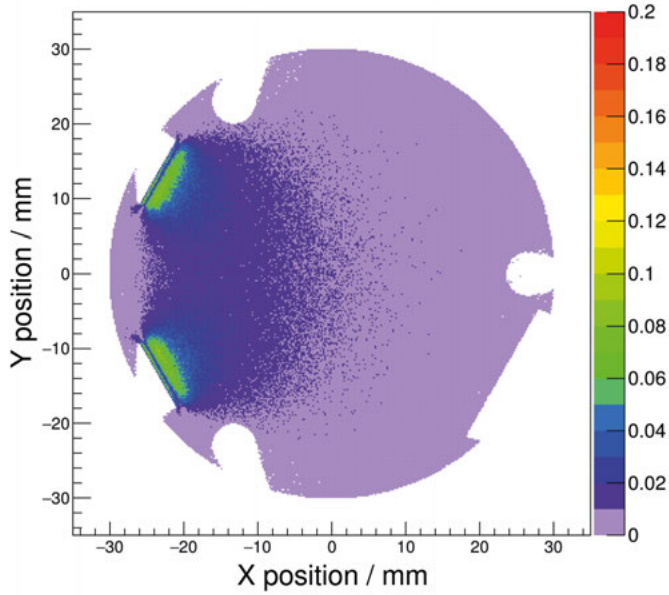


Figure 8.16. Positions of the ions stopped in the gas from **Sim I** given per μC of integrated primary beam current. Each pixel represents an $0.2\text{ mm} \times 0.2\text{ mm}$ area. Most ions are stopped close to the target they originated from.

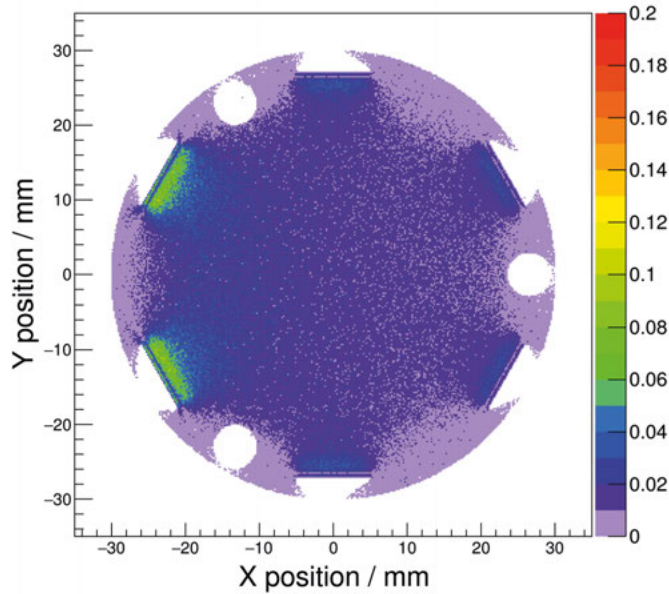


Figure 8.17. Positions of the ions stopped in the gas from **Sim VI** given per μC of integrated primary beam current. Each pixel represents an $0.2\text{ mm} \times 0.2\text{ mm}$ area. The targets in the back is clearly contributing much less than the front ones due to the reduced neutron flux.

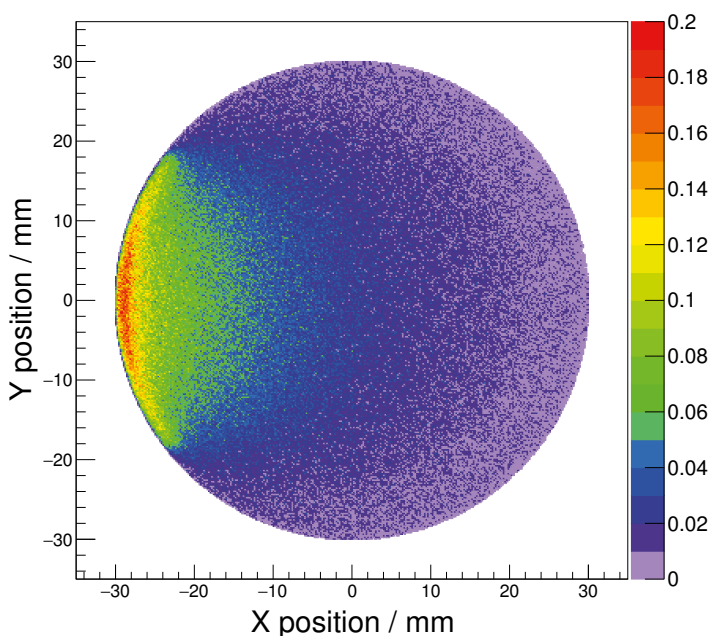


Figure 8.18. Yield of the ions stopped in the gas from **Sim VII** given per μC of integrated primary beam current. Each pixel represents an $0.2\text{ mm} \times 0.2\text{ mm}$ area. The target's size and closeness to the neutron source makes this a desirable setup.

8.2.4.4 Benchmarking against experimental values

Nobody knows exactly how many ions were stopped in the gas during the experiment in December 2016. This is because the ions are not measured until they have been extracted from the ion guide and passed through at least the mass selecting dipole magnet. Nevertheless, a rough estimate of the count rate of masses $A \approx 131$ was made.

About twelve counts per second was measured at the β -activity station downstreams of the mass selecting magnet; with a detector efficiency of about 30 % this roughly corresponds to 40 ions per second. Based on experience, the IGISOL team estimates an extraction efficiency from the ion guide of about 10 %, so one expects ~ 400 ions of this mass stopping in the gas each second. The beam current was at the moment $10\text{ }\mu\text{A}$.

The simulation of this setup predict 214 ions per second. Despite this being a much lower number, it is not as bad as it seems because of two main reasons. Firstly, the rough estimate based on the experimental values consists of several estimations with large uncertainties. Secondly, the exact positions of the uranium targets in the experimental setup were not properly documented. In lack of detailed information, I put the targets centred on the hexagonal sides of the target holder when I implemented the simulation geometry. However, some photo documentation might indicate that the targets were slightly closer

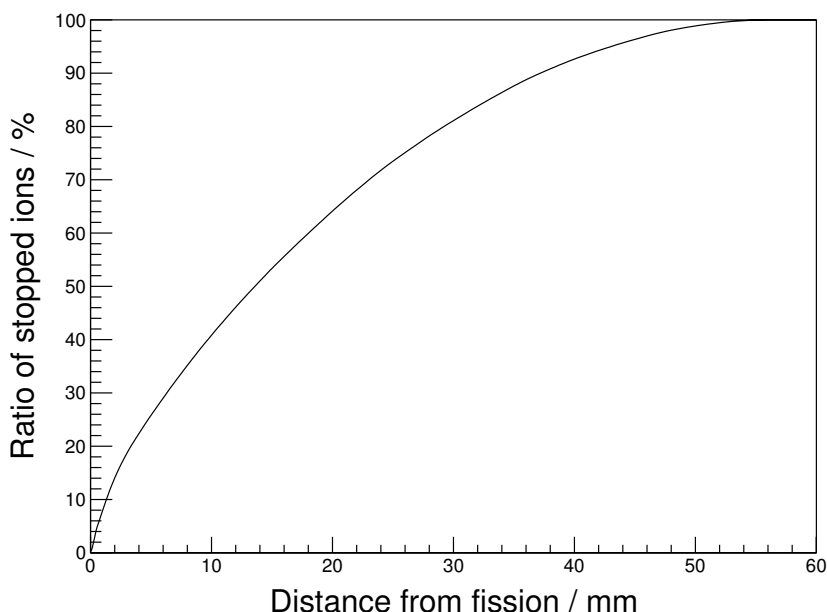


Figure 8.19. Cumulative distribution of the how far the stopped ions travelled from the fission event perpendicular to the target surface. Only FPs that escape the target and stop in the gas are taken into account.

to the beam centre. Even a small difference in distance would quickly give rise to a sizeable discrepancy since the neutron flux is much greater toward the beam centre.

Taken this into account, I conclude that the numbers are in the right order of magnitude and that more work and detailed documentation is needed from the experimental side.

8.2.5 Conclusions

Also for the neutron induced case one sees that the targets are of reasonable thickness (not surprisingly since they were almost the same thickness). Thicker targets are unnecessary and thinner ones risk introducing a mass dependent stopping efficiency, in addition to simply giving a lower yield. To increase the yield the target surface exposed to the gas must be increased, and the neutron flux through the target optimised. The setup **Sim VII** represent one way of doing this, which could be combined with a higher gas pressure to further enhance the yield of stopped ions in the gas. From fig. 8.19 one gets an idea of how much free space is needed, in front of each target. Perhaps, can the targets be placed closer to each other in a stacked formation as in Fig. 3 in Ref. [111].

Increasing the gas pressure showed no effect on the mass distribution of the stopped ions. The small dependencies on mass and atomic numbers are negligible as long as neighbouring isotopes are compared. However, if one would actually compare, e.g., a very heavy ion to a very light one, the relative difference would be no more than $\sim 20\%$. Chemical effects, e.g. different charge-state distributions after the ions are stopped for non-identical elements, might have additional effects which could not be predicted by these simulations. Comparing same-element isotopes is preferred when possible.

Since these new simulations give yield predictions for any FP on an absolute scale, they can be verified experimentally. The implantation foil present in **Sim I**, and also in the real experiment conducted in December 2016, will undergo a γ -spectroscopy analysis. This will hopefully prove that my simulation-based estimations and predictions have been sound with much less uncertainties than the rough estimate discussed in section 8.2.4.4. Such an analysis should also be able to determine which effective charge model that best reproduces the experimental results.

These simulations support the methodology employed at IGISOL, and agree with experimentally based estimates within the (admittedly large) uncertainties. The next step would be to further investigate the charge-state of the fully stopped ions end up in as well as how efficiently the gas flow can carry these ions into the vacuum part of IGISOL. This is outside the scope of this work, but would add to the knowledge of the ISOL-technique at hand. Nevertheless, the current developed tools can be used to investigate any new considered geometry, e.g., bigger chambers with larger gas volume to stop the ions in.

9. Svensk sammanfattning (Summary in Swedish)

Ja, det är här uranet förvandlas till plutonium som vi ska använda till bränsle i raket.

— Rymdkraft

Denna avhandlingen behandlar fyra olika projekt som alla handlar om att öka vår förståelse av neutron-inducerade reaktioner genom experimentell kärnfysikalisk forskning. En mycket viktig sådan reaktion är fission, dvs. kärnklyvning. Trots att man har kunnat driva kärnkraftverk säkert, i över 60 år, finns det mycket som fortfarande är okänt gällande exakt hur det går till när en tung atomkärna splittras till två mindre dotterkärnor. En mer detaljerade diskussion om fissionsprocessen ges i avsnitt 2.4. Ökad kunskap om fissionprocessen och bättre uppmätt fissiondata är betydelsefullt för både tillämpningar som kärnkraft, men också för grundforskningen.

För att neutronbaserade experiment överhuvudtaget ska kunna utföras krävs detektoruppställningar, stora forskningsanläggningar, men ofta även tillgång till tidigare uppmätt kärndata. Detektorerna som använts diskuteras i kapitel 3 och anläggningarna där dessa brukats i kapitel 4. Två av mina projekt har handlat om s.k. neutronstandardtvärsnitt som används för att mäta nya reaktionstvårsnitt relativt mot. Det är därmed av yttersta vikt att dessa standarder är mycket precist bestämda eftersom eventuella fel i standarden kommer att fortplanta sig till samtliga resultat i sådana relativa mätningar. Dessa standarder och hur de används beskrivs i avsnitt 2.1.

Mitt första projektet som beskrivs i kapitel 5 bestod i ett simuleringsarbete vars mål var att förutsäga hur vår planerade detektoruppställning skulle uppföra sig i en experimentell situation. Experimentet syftade främst till att mäta tre olika neutronstandardtvärsnitt jämt mot varandra och på så sätt minimera systematiska fel i mätningen. Reaktionerna i fråga var $H(n,n)$, $^{235}U(n,f)$ och $^{238}U(n,f)$. Själva experimenten har ännu inte utförts eftersom bygget av neutronanläggningen *Neutrons For Science* i Caen (Frankrike) [39, 40] har blivit mångårigt försenat. Dock visade simuleringarna vad för resultat vi kunde förvänta oss samt vad i utvecklingen av den experimentella uppställningen som vi borde fokusera på. Projektet och detektoruppställningen har vid det här laget utvecklats så pass att nya uppdaterade simuleringar planeras, baserade på de jag tidigare gjorde.

Kapitel 6 handlar om mitt andra projekt som också det försökte mäta neutronstandarder mot varandra. Denna gång berördes reaktionerna ${}^6\text{Li}(n,\alpha)t$ och ${}^{235}\text{U}(n,f)$ som mättes i en joniseringskammare. Till skillnad från fission är ${}^6\text{Li}(n,\alpha)t$ -reaktionen betydligt enklare eftersom endast två produkter skapas. Med hjälp av bevarandet av energi och rörelsemängd kan de två produkternas vinklar och energier beräknas analytiskt. Tre upprepade mätningar gjordes vid neutronanläggningen GELINA i Geel (Belgien) [42, 43] i samarbete med EU-laboratoriet JRC-Geel och både uppställning och metodik förbättrades för varje gång. Många problem löstes men tyvärr lyckades inte heller den sista mätningen att producera goda resultat med små osäkerheter, vilket så klart var vårt mål. Dock drogs många lärdomar av de problem som uppstod under projektets gång.

Båda ovan nämnda projekt använde sig av tvärsnittsdata för fissionsreaktioner för att deducera nya tvärsnitt för andra reaktioner, men mitt tredje projekt handlade om att faktiskt mäta fissionsdata. Även detta projekt var ett samarbete mellan Uppsala universitet och JRC-Geel. I kapitel 7 beskrivs utvecklingen av både fissionsspektrometern VERDI [90, 91] och den s.k. 2E-2v-analysmetoden. En av höjdpunkterna med denna metod är att antalet prompt emitterade neutroner kan härledas utan att själva neutronerna faktiskt mäts och utan att ta hjälp av tidigare uppmätt data. Mitt arbete har varit fokuserat på att kalibrera uppställningen och reproducera tidigare data för ${}^{252}\text{Cf}(sf)$. Användningen av kiseldetektorer skapar ett flertal komplikationer vilket kräver en icke trivial kalibreringsprocedur pga. det plasma som induceras när de tunga fissionprodukterna stoppas i detektorerna. Utvecklingsarbetet pågår fortfarande men flera framsteg har gjorts och lösningar på identifierade tillkortakommanden föreslås. En viktig insikt var att tidigare experiment av denna typ inte tagit hänsyn till en korrelation mellan den uppmätta fragmentmassan och neutronmultipliciteten. Jag utvecklade en enkel korrektionsmetod som även kan appliceras på tidigare uppmätta data från andra grupper.

Det fjärde och sista projektet behandlas i kapitel 8 och är, liksom mitt första projekt, av simuleringskaraktär. Det finländska universitetet i Jyväskylä handhar en anläggning, vid namn IGISOL [44, 45], som är till för precisa mätningar av fissionproduktsmassor och fissionsproduktsutbyte. Jag har skrivit, utfört och analyserat simuleringar i samråd med den experimentella IGISOL-gruppen både i Uppsala och Jyväskylä för att sprida ljus över hur många fissionsproduktsjoner som skapas under experimenten och hur många som förloras på vägen från produktionstället till mätstationen. Fissionsprodukterna skapas i uranfolier antingen genom direkt protonbestrålning eller genom att först skapa en neutronkälla av protonerna och sedan bestråla uranet med neutroner. Endast enstaka procent av dessa tunga joner stoppas sedan upp i buffertgasflödet som transporterar dem vidare i systemet mot någon av mätstationerna. En av frågeställningarna har varit om alla joner stoppas i gasen med samma sannolikhet oberoende av grundämne och massa. Jag kunde konstatera från simuleringarna att endast små skillnader beroende på jontyp behöver förväntas. Andra para-

metrar undersöktes också, såsom buffertgastrycket och olika sätt att placera strålmålen på. Jämförelser med experimentell data visade att simuleringarna var i rimlig överensstämmelse.

10. Acknowledgements

*A neural transceiver is required for
maximum communication, we will
work as one mind.*

— Borg collective

Science is not easy if you are all alone, but luckily I have had lots of people helping me throughout my time as a Ph.D student. I will try to list the most significant contributors, but most likely someone has undeservedly been forgotten (sorry!). I will start by thanking the Swedish Research Council, the CHANDA project, and the EUFRAT transnational access programme for their financial support, since science is so expensive.

I would like to thank all four of my official supervisors at Uppsala University for their support. As my main supervisor C. Gustavsson have given me a lot of valuable advice over the years. S. Pomp has provided me with contacts in the nuclear data community and arrangements so that I could work on interesting experiments. A. Prokofiev has long experience in the field and has an acute sense for details and tough questions. A. Al-Adili has been a great colleague and a source of incurable optimism, always happy to help, share and discuss.

Two of my projects resided at the European Commission Joint Research Centre in Geel, Belgium. It is truly a great place for science and I have learned a lot on each of my visits there. My *de facto* supervisors in Belgium, F.-J. Hambsch and S. Oberstedt have been welcoming and helpful. Together with A. Göök, they have all been valuable assets that gladly and patiently shared their experience, thoughts and expertise with me. I thank M. Vidali for his assistance in so many things, T. Gamboni for fixing my vacuum, W. Geerts for finding me tape, N. Sevenhans for letting me safely in to the experiments, and everyone else at the JRC who have been of assistance. Although not at JRC-Geel anymore, I thank R. Bevilacqua as well as M. O. Fréreau for introducing me to their previous projects.

Back in Uppsala, some people deserve special thanks, among them: E. Andersson Sundén and A. Hjalmarsson for their many ideas and the fruitful discussions I have had with them, revolving just about anything. Also thanks to the IGISOL group in Uppsala: M. Lantz, A. Mattera, V. Rakopoulos and A. Solders. They are the ones who do the hard experimental work while I just simulate it.

Many typos and errors are no longer in this thesis, whereas improvements have taken their place instead. This is thanks to the proof-reading and reviewing

of my manuscript performed by A. Al-Adili, C. Gustavsson, F.-J. Hambsch, A. Solders, S. Oberstedt, A. Prokofiev, and D. Tarrío.

Appendix A.

Code developed

*Am Heimcomputer sitz' ich hier
und programmier' die Zukunft mir.*

— Kraftwerk

In this appendix I have collected short descriptions of codes I have developed that might be of general interest. They are all available upon request.

A.1 Modifications to Geant4

A.1.1 Extended and corrected cross sections

When writing a Geant4 simulation program one can, for a certain physical process, choose which physics model one likes to use depending on the energy region. For neutron reactions, Geant4 includes a *High Precision* (HP) model which is driven by data collected from evaluations. However since data is not always available for higher energies, the model only covers the energy region 0 to 20 MeV. If one would like to cover a larger energy range, one would need to supplement the HP model with another model and 'stitch' them together at 20 MeV. Sometimes it can be difficult to make a smooth transition from one model to the other. One could also try to find a non-data driven model that works for the whole interval, but one would then need to rely on theoretical calculations or parametrisations rather than experimentally measured data.

Since the simulations described in section 5.3 modelled neutrons up to 40 MeV, I had to go for one of these options. To capture the cross section as accurate as possible I implemented data-driven fission cross sections for the whole energy range. Normally, this would be somewhat trivial to do with Geant4, since models describing the physical process are completely independent of the models describing cross sections. However, the model that was used for inelastic scattering (above 20 MeV), the *Binary Cascade* model [36, p. 450], treats the fission process on the same footing as inelastic scattering. The fission channel is included in the inelastic scattering model as if it was just another channel of inelastic scattering. In order for me to add a new fission process above 20 MeV, I had to remove the fission part from the inelastic model to avoid doubling the fission event rate. After that I added a

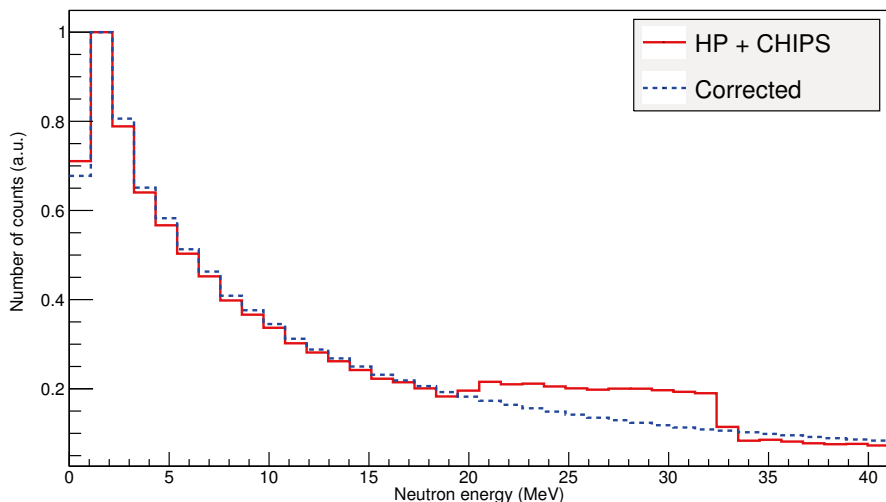


Figure A.1. The histogram shows the counts of simulated recoil protons from elastic neutron scattering on hydrogen versus incident neutron energy. The results shown by the solid curve were obtained when the simulation was using default Geant4 classes. The dashed curve shows the result after new cross sections were supplied.

new model with my own data-driven cross sections based on the IAEA neutron standards evaluations [112].

I also had to implement new cross section for elastic scattering since I discovered non-physical structures in the default cross section (CHIPS parametrisation [36, p. 388]). For elastic scattering one expects a smooth behaviour of the cross section as a function of energy [9, 113, 114], but this was not the case as showcased in fig. A.1. The change of cross section data could be done in a straight-forward way due to Geant4’s support of adding cross section independently of the physics models. In Fig. A.1 I show the difference before and after my cross-section fix. The curve obtained when the simulation was using cross sections provided by unmodified Geant4 classes (HP in the range 0 to 20 MeV and CHIPS above 20 MeV) exhibits a structure in the energy range 20 to 35 MeV. After substituting the CHIPS parametrisation with additional data from evaluations [113] the expected smooth behaviour was restored.

A.1.2 Biasing of discrete events in simulations

In order to save time while doing a simulation starting from the incoming neutron, custom code that scaled up certain cross sections and weighted the particles accordingly was implemented. Current versions of Geant4 now include this functionality through default classes, but at the time the simulation software discussed in section 5.3 was written, they did not.

This custom implementation of cross-section scaling within Geant4 simulations is similar to the one described by Mendenhall and Weller [115]. The scaling factor, the process to be biased and the geometrical regions in which the scaling occurs, are all configurable through a messenger helper class accompanying the main class.

The new class, `BiasedProcess`, inherits `G4WrapperProcess` and wraps discrete processes. It works by substituting the original process with the wrapper process. When the wrapper process is called by Geant4, it will forward the call to the original process. In the case when Geant4 asks it to calculate the interaction length, the wrapper process will use the original process to calculate the unbiased interaction length. Before returning this value to Geant4 it will divide the unbiased interaction length with a biasing factor thus scaling the cross section.

To compensate the biasing, each event is given a weight. If no biasing is done this weight will be unity. If we e.g. scale the fission cross section upwards, the weight for fission events will be lower than unity. On the other hand, every distance the particle travels without any fission occurring will increase the particle weight. After each step in a region where biasing is applied the weight is adjusted accordingly.

When the biased interaction occurs, the weight is linearly scaled by the biasing factor b . The new weight is given by

$$w_{\text{new}} = \frac{w_{\text{old}}}{b}, \quad (\text{A.1})$$

where w_{old} and w_{new} denotes the weights before and after the interaction, respectively. A particle travelling the distance Δx through a region with a biased process adjusts its weight by an exponential factor. This time the new weight is given by

$$w_{\text{new}} = w_{\text{old}} \exp\left(\frac{(b-1)\Delta x}{\ell}\right), \quad (\text{A.2})$$

where ℓ denotes the (unbiased) mean free path. Eq. A.1 and A.2 ensure that the product of the probability and the weight is kept constant, no matter what biasing factor is used.

If we assume that we use the biasing to make the occurrence of an unusual event to become more likely in the simulations, i.e. $b > 1$, Eq. A.1 would decrease the weight whenever the biased event happens, compensating the increased rate in the simulation of this kind of event. Similarly, Eq. A.2 would increase the weight if the particle just passes by and no interaction of that kind occurs.

Every particle in the simulations carries a weight but `BiasedProcess` keeps track of the accumulated weight for the whole event, i.e. everything that happen in the simulation due to one primary particle. The resulting weight of the full event is saved together with the rest of the event data. The event weight is a

measure of the likeliness of the event as a whole, taking all biased reactions into account.

All biasing options can be specified at the command prompt or in a macro at any time before the simulation starts. One specifies the biasing factor, b , and the biased particle type as well as any number of `G4VPhysicalVolume` instances where the bias should be activated. One can also choose whether only the primary particle should be biased or secondaries as well. To avoid events with very low weights ($w < 1/b$) yet another option exists to limit the biasing to never go below a certain limit.

This class was tested and used for the simulations described in section 5.3. Fission as well as elastic and inelastic scattering have been biased to get higher statistics more efficiently. The most highly biased processes in this work were using a biasing factor of 1000. However, the track of a non-reacting neutron requires little time to be calculated, compared to the case where several secondary particles are produced by reactions induced by the primary particle. Therefore, the CPU time reduction when using biasing was usually not more than an order of magnitude, compared to the non-biased case. If the unbiased reactions are more time-consuming to simulate, the potential benefits of biasing might increase.

A.1.3 New effective charge model

As was mentioned in section 3.4.2 the effective charge of an ion affect the stopping power greatly. By default Geant4 parametrises the effective charge as a function of the atomic numbers of the projectile, the atomic number of the bulk material, and the projectile velocity [36]. The exact expression is based on the work of Brandt and Kitagawa [116]. However, newer parametrisations exist and heavy ion stopping powers are still not accurately known. Schiwietz and Grande fitted expressions to available experimental data for both gaseous and solid materials, respectively [37]. While the parameters are the same, the functional form is different.

Implementing a new charge-state formula in Geant4, based on the parameter values found by Schiwietz and Grande, turned out to be not so difficult. The whole calculation is contained within the class `G4ionEffectiveCharge` but the Geant4 authors did not provide a simple way of substitute it with your own custom class. Among other things many methods in relevant classes were not declared *virtual*. In order to minimise the intrusion to the Geant4 code, I instead modified the class `G4ionEffectiveCharge` directly in the Geant4 (version 10.01.p03) source tree to include an option to use the Schiwietz and Grande parametrisation instead. The default option was still available, so the user could easily switch between the two options through a macros command to compare how the different charge models affect the simulation results. Generally, the Schiwietz and Grande parametrisation yields higher

charges and therefore shorter stopping ranges, which was observed in the IGISOL simulations reported on in chapter 8.

A.2 ROOT file I/O made simple

The ROOT Data Analysis Framework is a commonly used library within experimental nuclear physics. Among other things it specifies its own file format and data structures which are designed to store experimental, simulated or analysed data, event by event. Instead of writing almost the same code over and over again in all my different analysis projects, I decided to write a C++ class that took care of it once and for all. My class wraps the storing process and provides a simpler and more fool proof interface to the user.

Since simplicity was preferred over technical elegance, the class `RootFileManager` was designed as a singleton class, reachable from anywhere in the code through a *static* member method. I restricted it to only handle one file at a time since I never had a use for more than that. To use it in a project, the user first needs to initialise it by specifying the output file and what kind of data will be stored in the file for each event. A handle for each data slot is returned and will be the key to store the correct data in the correct slot. This is quite literally so, because the handle is internally used as the key in a binary tree to find the correct storage. The following code would create a new event tree and preparing it to store two variables for each event, one 64-bit integer named *A* and one low precision floating point value named *B*, respectively.

Example code

```
RootFileManager* rfm = RootFileManager::Instance();
rfm->OpenFile("output.root");
handle my_tree = rfm->NewTree("MyEvents");
handle my_a = rfm->NewInt64(my_tree,"A");
handle my_b = rfm->NewFloat32(my_tree,"B");
```

Note that ROOT calls its event data structure a 'tree', but it is not a binary tree as one might suspect. It is possible to work with any number of trees in parallel. Later on when our example program, e.g., has acquired one event. The important values *a* and *b* are saved by calling the different `Fill` methods of `RootFileManager` followed by a call to `CloseEntry()`:

Example code

```
rfm->FillInt(my_tree,a);
rfm->FillFloat(my_tree,b);
rfm->CloseEntry();
```

Nothing is actually written to the output file until the last call, but rather kept in buffers. Calling `CloseEntry(my_tree)` will store the current content of

the buffers corresponding to the particular event tree that is specified through the supplied handle *my_tree*. When all events has been processed the file is closed by a call to `CloseFile()`, but that can also be left to be handled by the destructor if it also the end of the program.

The primitive data types that can be saved are integers and floating point values, of either 32 bits or 64 bits. One can also specify that one likes to store an arbitrary long vector of these primitive types for each event. In addition one can also save strings, graphs and arrays of objects as long as they inherit from the Root main class `TObject`. It is also possible to store any `TObject` descendant directly, outside the event structure, but possibly in a folder hierarchy.

The versatility and ease of use proved the initial effort to write the class worth it, it has been used in every single project presented in this thesis (and a few others).

A.3 Acquisition software for a SPdevices digitiser

A few years back our laboratory was equipped with a new SPdevices digitiser (model ADQ412). Since we lacked a suitable easy to use acquisition program, especially any that ran on Linux systems, I wrote a new one from scratch.

The acquisition program runs from a command line interface either in interactive or batch mode. It was written with minimalism in mind and has no dependencies except for the C++11 standard library and the provided API from SPdevices. All important configuration options can be set in a simple text file supplied at the command line. The user can choose the output file(s) and how large they should be, as well as if the program should terminate after a certain number of events. It can also be run in a 'waiting' mode where it acquires a number of events and then wait for the user to make adjustments on the experimental setup before collecting the next set of events.

The device itself is connected with a USB cable to a normal PC, it features four 12-bit precision channels and a sample rate of 1 GHz. By using only two of the channels in a so called interleaving mode, the sample rate can be doubled. Each event will be collected as the detector voltage level crosses a preset threshold. Which of the channels that will be stored to disk, as well as which can trigger acquisition, are configurable. The total size of the trace as well as the number of samples before the trigger, are also chosen before the acquisition starts. A few more options, like configurable DC-offsets for each channel, is also available.

The output format is a binary file with a fixed sized header containing information about the specific acquisition. The header mostly contains the configuration parameters given to the digitiser, as well as the acquisition date and total time of the acquisition. After the header, all event traces for all active channels are stored subsequently. Each with a timestamp indicating exactly when the event occurred.

The program has proven useful since it has been used by several groups and is now at version 6. After me being the only developer for a long time, it is now continuously developed by several people. It runs on Linux and most likely also on Windows (but this has not been tested). It only supports the ADQ412 model, but adaptations to other SPdevices digitisers should be easy.

Appendix B.

Selected publications

Time moves in one direction, memory another. We are that strange species that constructs artifacts intended to counter the natural flow of forgetting.

— William Gibson

Published full length papers

I **Two level scheme solvers for nuclear spectroscopy**

K. Jansson, D. DiJulio, J. Cederkäll, Nucl. Instrum. Meth. A 654 (2011) 496–501, doi:10.1016/j.nima.2011.07.021

My contribution: Designed, implemented and analysed the algorithms, wrote the paper, based on my master's thesis.

II **Designing an upgrade of the Medley setup for light-ion production and fission cross-section measurements**

K. Jansson, C. Gustavsson, A. Al-Adili, A. Hjalmarsson, E. Andersson-Sundén, A. V. Prokofiev, D. Tarrío, S. Pomp, Nucl. Instrum. Meth. A, 794 (2015) 141–150, doi:10.1016/j.nima.2015.05.001

My contribution: Wrote the software, performed the analysis, wrote the paper.

III **Simulations of the fission-product stopping efficiency in IGISOL**

A. Al-Adili, K. Jansson, M. Lantz, A. Solders, D. Gorelov, C. Gustavsson, A. Mattera, I. Moore, A. V. Prokofiev, V. Rakopoulos, H. Penttilä, D. Tarrío, S. Wiberg, M. Österlund, S. Pomp, EPJ A 51 5 (2015) 59, doi:10.1140/epja/i2015-15059-2

My contribution: Wrote the simulation software, participated in the analysis and paper writing.

IV **Estimates of the production rates of exotic nuclei from the ion-guide for neutron induced fission at IGISOL**

K. Jansson, A. Al-Adili, N. Nilsson, M. Norlin, A. Solders, Submitted to EPJ A (2017), doi: N/A

My contribution: Wrote the main simulation software, performed the analysis, wrote the paper.

V **Defective fission correlation data from the 2E-2v method**

K. Jansson, A. Al-Adili, E. Andersson Sundén, A. Göök, S. Oberstedt, S. Pomp, Submitted to Phys. Rev. C (2017), doi: N/A

My contribution: Wrote all software, performed the analysis, wrote the paper.

Published conference proceedings

VI **Measuring Light-ion Production and Fission Cross Sections Normalised to H(n,p) Scattering at the Upcoming NFS Facility**

K. Jansson, C. Gustavsson, S. Pomp, A. V. Prokofiev, G. Scian, D. Tarrío, Nuclear Data Sheets 119 (2014) 395–397, doi:10.1016/j.nds.2014.08.110

My contribution: Performed the simulations and the analysis, wrote the paper.

VII **Light-ion Production from O, Si, Fe and Bi Induced by 175 MeV Quasi-monoenergetic Neutrons**

R. Bevilacqua, S. Pomp, K. Jansson, C. Gustavsson, M. Österlund, V. Simutkin, M. Hayashi, S. Hirayama, Y. Naitou, Y. Watanabe, A. Hjalmarsson, A. Prokofiev, U. Tippawan, F.-R. Lecolley, N. Marie, S. Leray, J.-C. David, S. Mashnik, Nuclear Data Sheets 119 (2014) 190–193, doi:10.1016/j.nds.2014.08.053

My contribution: Produced integrated cross sections.

VIII **Measurement of the ${}^6\text{Li}(n,\alpha)$ neutron standard cross-section at the GELINA facility**

K. Jansson, A. Al-Adili, R. Bevilacqua, C. Gustavsson, F.-J. Hambsch, S. Pomp, M. Vidali, EPJ Web Conf. 122 (2016) 08006, doi:10.1051/epjconf/201612208006

My contribution: Analysed the data, wrote the paper.

- IX Analysis of prompt fission neutrons in $^{235}\text{U}(\text{n}_{\text{th}},\text{f})$ and fission fragment distributions for the thermal neutron induced fission of ^{234}U**
A. Al-Adili, D. Tarrío, F.-J. Hambsch, A. Göök, K. Jansson, A. Solders, V. Rakopoulos, C. Gustafsson, M. Lantz, A. Mattera, S. Oberstedt, A.V. Prokofiev, M. Vidali, M. Österlund, S. Pomp, EPJ Web Conf. 122 (2016) 01007, doi:10.1051/epjconf/201612201007
My contribution: Participated in the $^{235}\text{U}(\text{n}_{\text{th}},\text{f})$ experiment, assisted the analysis.
- X Measurement of the $^6\text{Li}(\text{n},\alpha)\text{t}$ neutron standard cross-section at the GELINA facility**
K. Jansson, A. Al-Adili, R. Bevilacqua, C. Gustavsson, F.-J. Hambsch, S. Pomp, M. Vidali, EPJ Web Conf. 146 (2017) 11047, doi:10.1051/epjconf/201714611047
My contribution: Analysed the data, wrote the paper.
- XI The new double energy-velocity spectrometer VERDI**
K. Jansson, M. O. Fréreau, A. Al-Adili, A. Göök, C. Gustavsson, F.-J. Hambsch, S. Oberstedt, S. Pomp, EPJ Web Conf. 146 (2017) 04016, doi:10.1051/epjconf/201714604016
My contribution: Analysed the data, wrote the paper together with M. O. Fréreau.
- XII Simulations of the stopping efficiencies of fission ion guides**
A. Solders, A. Al-Adili, D. Gorelov, K. Jansson, A. Jokinen, V. Kolhinen, M. Lantz, A. Mattera, I. Moore, N. Nilsson, M. Norlin, H. Penttilä, S. Pomp, A. V. Prokofiev, V. Rakopoulos, S. Rinta-Antila, V. Simutkin, and the IGISOL group, EPJ Web Conf. 146 (2017) 03025, doi:10.1051/epjconf/201714603025
My contribution: Wrote the simulation software, co-supervised the student project performing the analysis.
- XIII Neutron-multiplicity experiments for enhanced fission modelling**
A. Al-Adili, D. Tarrío, F.-J. Hambsch, A. Göök, K. Jansson, A. Solders, V. Rakopoulos, C. Gustavsson, M. Lantz, A. Mattera, S. Oberstedt, A. V. Prokofiev, E. Andersson Sundén, M. Vidali, M. Österlund, S. Pomp, EPJ Web Conf. 146 (2017) 04056, doi:10.1051/epjconf/201714604056
My contribution: Participated in the experiment, assisted the analysis.

References

- [1] O. Hahn and F. Strassmann, *Naturwissenschaften* **27**, 11 (1939) 10.1007/BF01488241.
- [2] L. Meitner and O. R. Frisch, *Nature* **143** (1939) 10.1038/143239a0.
- [3] W. Moomaw et al., *Annex II: Methodology. In IPCC Special Report on Renewable Energy Sources and Climate Change Mitigation*, edited by O. Edenhofer et al. (Cambridge University Press, 2011), http://www.ipcc-wg3.de/report/IPCC_SRREN_Annex_II.pdf.
- [4] IPCC, *Climate Change 2014: Mitigation of Climate Change. Contribution of Working Group III to the Fifth Assessment Report of the Intergovernmental Panel on Climate Change*, edited by O. Edenhofer et al. (Cambridge University Press, 2014), https://www.ipcc.ch/pdf/assessment-report/ar5/wg3/ipcc_wg3_ar5_full.pdf.
- [5] K. Jansson, *Improving the Neutron Cross-section Standards $^{238}\text{U}(n,f)$ and $^6\text{Li}(n,\alpha)$* , Licentiate thesis, (Uppsala, 2015), <http://uu.diva-portal.org/smash/get/diva2:821395/FULLTEXT01.pdf>.
- [6] M. Sarsour et al., *Phys. Rev. Lett.* **94**, 082303 (2005) 10.1103/PhysRevLett.94.082303.
- [7] A. D. Carlson, *Metrologia* **48**, S328 (2011) 10.1088/0026-1394/48/6/S09.
- [8] *STANDARDS Data development project*, Accessed: 2017-06-01, <https://www-nds.iaea.org/standards>.
- [9] V. G. J. Stoks et al., *Phys. Rev. C* **48**, 792 (1993) 10.1103/PhysRevC.48.792.
- [10] H. Conde, ed., *Nuclear Data Standards for Nuclear Measurements 1991 NEANDC/INDC Nuclear Standards File*, 1992, <https://www.oecd-nea.org/science/docs/1991/neandc1991-311-u.pdf>.
- [11] O. Wasson and R. Schrack, *Nucl. Instrum. Meth. A* **282**, 194 (1989) 10.1016/0168-9002(89)90140-X.
- [12] W. Pauli, *Zeitschrift für Physik* **31**, 765 (1925) 10.1007/BF02980631.
- [13] R. Krücken, *Contemp. Phys.* **52**, 101 (2011) 10.1080/00107514.2010.509993.
- [14] J. P. Schiffer et al., *Phys. Rev. Lett.* **92**, 162501 (2004) 10.1103/PhysRevLett.92.162501.

- [15] K.-H. Schmidt et al., Nucl. Phys. A **665**, 221 (2000) 10.1016/S0375-9474(99)00384-X.
- [16] K.-H. Schmidt et al., Nucl. Data Sheets **131**, Special Issue on Nuclear Reaction Data, 107 (2016) 10.1016/j.nds.2015.12.009.
- [17] V. Strutinsky, Nucl. Phys. A **95**, 420 (1967) 10.1016/0375-9474(67)90510-6.
- [18] P. Möller et al., Phys. Rev. C **79**, 064304 (2009) 10.1103/PhysRevC.79.064304.
- [19] U. Brosa et al., Phys. Rep. **197**, 167 (1990) 10.1016/0370-1573(90)90114-H.
- [20] J. Randrup and P. Möller, Phys. Rev. Lett. **106**, 132503 (2011) 10.1103/PhysRevLett.106.132503.
- [21] N. Metropolis et al., J. Chem. Phys. **21**, 1087 (1953) 10.1063/1.1699114.
- [22] N. Bohr, Phys. Rev. **58**, 864 (1940) 10.1103/PhysRev.58.864.
- [23] A. Stolarz et al., Nucl. Instrum. Meth. A **613**, 351 (2010) 10.1016/j.nima.2009.09.074.
- [24] L. Zhang et al., Nucl. Instrum. Meth. B **267**, 3480 (2009) 10.1016/j.nimb.2009.08.005.
- [25] R. Bevilacqua et al., Nucl. Instrum. Meth. A **770**, 64 (2015) 10.1016/j.nima.2014.10.003.
- [26] W. Shockley, J. Appl. Phys. **9**, 635 (1938) 10.1063/1.1710367.
- [27] A. Al-Adili et al., Nucl. Instrum. Meth. A **624**, 684 (2010) 10.1016/j.nima.2010.09.126.
- [28] A. Göök et al., Nucl. Instrum. Meth. A **664**, 289 (2012) 10.1016/j.nima.2011.10.052.
- [29] G. Hempel et al., Nucl. Instrum. Meth. A **131**, 445 (1975) 10.1016/0029-554X(75)90432-2.
- [30] H. Hui et al., Nucl. Instrum. Meth. A **481**, 160 (2002) 10.1016/S0168-9002(01)01333-X.
- [31] D. Tarrío et al., Nucl. Instrum. Meth. A **743**, 79 (2014) 10.1016/j.nima.2013.12.056.
- [32] T. Gys, Nucl. Instrum. Meth. A **787**, New Developments in Photodetection NDIP14, 254 (2015) 10.1016/j.nima.2014.12.044.
- [33] Q. Zhang et al., Rev. Sci. Instrum. **81**, 073112 (2010) 10.1063/1.3463690.
- [34] G. F. Knoll, *Radiation detection and measurement*, 4th (John Wiley & Sons Inc., 2010), 830 pp., ISBN: 0470131489.

- [35] G. Lutz, *Semiconductor radiation detectors* (Springer-Verlag Berlin Heidelberg, 2001), 10.1007/978-3-540-71679-2.
- [36] *Physics reference manual*, v. 9.6.0, Geant4 collaboration (2012), <http://geant4.web.cern.ch/geant4/UserDocumentation/UsersGuides/PhysicsReferenceManual/BackupVersions/V9.6/fo/PhysicsReferenceManual.pdf>.
- [37] G. Schiwietz and P. Grande, Nucl. Instrum. Meth. B **175**, 125 (2001) 10.1016/S0168-583X(00)00583-8.
- [38] H. W. Schmitt et al., Phys. Rev. **137**, B837 (1965) 10.1103/PhysRev.137.B837.
- [39] Ledoux, X. et al., EPJ Web Conf. **146**, 03003 (2017) 10.1051/epjconf/201714603003.
- [40] X. Ledoux et al., *Technical proposal for the spiral 2 instrumentation*, 2008, pro.ganil-spiral2.eu/spiral2/instrumentation/nfs/working-documents/nfs-technical-report.
- [41] M. Lewitowicz, Nucl. Phys. A **805**, INPC 2007 Proceedings of the 23rd International Nuclear Physics Conference, 519c (2008) 10.1016/j.nuclphysa.2008.02.290.
- [42] Institute for Reference Materials and Measurements (Geel), Unit Standards for Nuclear Safety, Security and Safeguards, *EUFRAT NUCLEAR FACILITIES AT JRC-IRMM*, Accessed: 2017-07-27, <https://ec.europa.eu/jrc/sites/default/files/eufrat-facilities.pdf>.
- [43] European Commission, Joint Research Centre, *Linear electron accelerator facility*, Accessed: 2017-07-27, <https://ec.europa.eu/jrc/en/research-facility/linear-electron-accelerator-facility>.
- [44] Penttilä, H. et al., EPJ A **52**, 104 (2016) 10.1140/epja/i2016-16104-4.
- [45] J. Äystö et al., Hyperfine Interactions **223**, 1 (2014) 10.1007/s10751-013-0872-z.
- [46] A. Mattera et al., EPJ A **53**, 173 (2017) 10.1140/epja/i2017-12362-x.
- [47] A. Mattera et al., ‘Production of Sn and Sb isotopes in high-energy neutron induced fission of nat U’, Submitted to EPJ A, 2017.
- [48] V. Kolhinen et al., Nucl. Instrum. Meth. A **528**, 776 (2004) 10.1016/j.nima.2004.05.029.
- [49] U. Tippawan et al., Phys. Rev. C **79**, 064611 (2009) 10.1103/PhysRevC.79.064611.
- [50] R. Bevilacqua et al., Nucl. Instrum. Meth. A **646**, 100 (2011) 10.1016/j.nima.2011.04.036.
- [51] S. Pomp et al., EPJ Web Conf. **8**, 07013 (2010) 10.1051/epjconf/20100807013.

- [52] K. Jansson et al., Nucl. Data Sheets **119**, 395 (2014) 10.1016/j.nds.2014.08.110.
- [53] K. Jansson et al., Nucl. Instrum. Meth. A **794**, 141 (2015) 10.1016/j.nima.2015.05.001.
- [54] I. Slypen et al., Radiat. Prot. Dosim. **70**, 21 (1997) 10.1093/oxfordjournals.rpd.a031945.
- [55] S. Benck et al., Phys. Med. Biol. **43**, 3427 (1998) 10.1088/0031-9155/43/12/003.
- [56] S. Benck et al., Nucl. Sci. Eng. **141**, 55 (2002) 10.13182/NSE02-A2266.
- [57] I. Slypen et al., J. Phys. G: Nucl. Part. Phys. **30**, 45 (2004) 10.1088/0954-3899/30/2/005.
- [58] JEDEC Solid State Technology Association, JEDEC Standard, (2006).
- [59] D. Jones and A. Wambersie, Nucl. Instrum. Meth. A **580**, Proceedings of the 10th International Symposium on Radiation Physics ISRP 10, 522 (2007) 10.1016/j.nima.2007.05.220.
- [60] M. Gilbert et al., J. Nucl. Mater. **442**, S755 (2013) 10.1016/j.jnucmat.2013.03.085.
- [61] P. Beck, Radiat. Prot. Dosim. **136**, 244 (2009) 10.1093/rpd/ncp158.
- [62] C. Zeitlin et al., Science **340**, 1080 (2013) 10.1126/science.1235989.
- [63] P. J. Griffin et al., IEEE Trans. Nucl. Sci. **59**, 1167 (2012) 10.1109/TNS.2012.2193900.
- [64] P. Lisowski et al., Proceedings of the Specialists' Meeting on Neutron Cross Section Standards for the Energy Range Above 20 MeV (Uppsala, Sweden) (1991).
- [65] O. Shcherbakov et al., J. Nucl. Sci. Technol. **39**, 230 (2002) 10.1080/00223131.2002.10875081.
- [66] C. Paradela et al., Phys. Rev. C **91**, 024602 (2015) 10.1103/PhysRevC.91.024602.
- [67] R. Nolte et al., Nucl. Sci. Eng. **156**, 197 (2007) 10.13182/NSE06-14.
- [68] Tarrío, Diego et al., EPJ Web Conf. **146**, 03026 (2017) 10.1051/epjconf/201714603026.
- [69] M. Hayashi et al., EDP Sciences, 1091 (2007) 10.1051/ndata:07747.
- [70] D. Tarrío, 'Neutron-induced fission fragment angular distribution at CERN n_TOF: The Th-232 case', PhD thesis (University of Santiago de Compostela, 2012), <https://cds.cern.ch/record/1474269>.
- [71] S. Agostinelli et al., Nucl. Instrum. Meth. A **506**, 250 (2003) 10.1016/S0168-9002(03)01368-8.

- [72] Geant4 collaboration, *Reference Physics Lists*, Accessed: 2017-06-01, http://geant4.cern.ch/support/proc_mod_catalog/physics_lists/referencePL.shtml.
- [73] A. Breskin and N. Zwing, Nucl. Instrum. Meth. **144**, 609 (1977) 10.1016/0029-554X(77)90034-9.
- [74] L. Audouin et al., EDP Sciences, 421 (2008) 10.1051/ndata:07675.
- [75] R. Bevilacqua et al., Nucl. Data Sheets **119**, 104 (2014) 10.1016/j.nds.2014.08.029.
- [76] K. Jansson et al., EPJ Web Conf. **122**, 08006 (2016) 10.1051/epjconf/201612208006.
- [77] Jansson, Kaj et al., EPJ Web Conf. **146**, 11047 (2017) 10.1051/epjconf/201714611047.
- [78] D. Tilley et al., Nucl. Phys. A **708**, 3 (2002) 10.1016/S0375-9474(02)00597-3.
- [79] G. Zhang et al., Nucl. Instrum. Meth. A **566**, 615 (2006) 10.1016/j.nima.2006.06.064.
- [80] M. Devlin et al., AIP Conf. Proc. **1090**, 215 (2009) 10.1063/1.3087015.
- [81] M. Chadwick et al., Nucl. Data Sheets **112**, Special Issue on ENDF/B-VII.1 Library, 2887 (2011) 10.1016/j.nds.2011.11.002.
- [82] R. Bencardino et al., Nucl. Sci. Eng. **177**, 68 (2014) 10.13182/NSE13-25.
- [83] J. F. Ziegler et al., Nucl. Instrum. Meth. B **268**, 19th International Conference on Ion Beam Analysis, 1818 (2010) 10.1016/j.nimb.2010.02.091.
- [84] J. H. Hubbell and S. M. Seltzer, *Tables of X-Ray Mass Attenuation Coefficients and Mass Energy-Absorption Coefficients (version 1.4)*, tech. rep. NISTIR 5632, Accessed: 2017-05-19 (National Institute of Standards and Technology, Gaithersburg, MD, 2004), physics.nist.gov/xaamdi.
- [85] F.-J. Hambsch and I. Ruskov, Nucl. Sci. Eng. **156**, 103 (2007).
- [86] T. Nagy et al., Nucl. Instrum. Meth. **8**, 327 (1960) 10.1016/S0029-554X(60)80030-4.
- [87] A. Andronic et al., Nucl. Instrum. Meth. A **523**, 302 (2004) 10.1016/j.nima.2003.11.426.
- [88] H. Bai et al., Nucl. Instrum. Meth. A **840**, 36 (2016) 10.1016/j.nima.2016.09.049.
- [89] H.-H. Knitter et al., Nuclear Data for Science and Technology: Proceedings of the International Conference Antwerp 6–10 September 1982, 451 (1983) 10.1007/978-94-009-7099-1_97.

- [90] M. Frégeau et al., Nucl. Instrum. Meth. A **817**, 35 (2016) 10.1016/j.nima.2016.02.011.
- [91] Jansson, Kaj et al., EPJ Web Conf. **146**, 04016 (2017) 10.1051/epjconf/201714604016.
- [92] R. Müller et al., Phys. Rev. C **29**, 885 (1984) 10.1103/PhysRevC.29.885.
- [93] K. Nishio et al., J. Nucl. Sci. Technol. **32**, 404 (1995) 10.1080/18811248.1995.9731725.
- [94] G. Audi et al., Chinese Phys. C **36**, 1287, 1287 (2012) 10.1088/1674-1137/36/12/002.
- [95] M. Wang et al., Chinese Phys. C **36**, 1603, 1603 (2012) 10.1088/1674-1137/36/12/003.
- [96] W. Bohne et al., Nucl. Instrum. Meth. A **240**, 145 (1985) 10.1016/0168-9002(85)90398-5.
- [97] R. Yanez, *Range – the -dE/dx and range C/C++ library*, version 0.1.5, <http://www.calel.org/range.html>.
- [98] A. Göök et al., Phys. Rev. C **90**, 064611 (2014) 10.1103/PhysRevC.90.064611.
- [99] J. Velkovska and R. McGrath, Nucl. Instrum. Meth. A **430**, 507 (1999) 10.1016/S0168-9002(99)00225-9.
- [100] K.-T. Brinkmann et al., Nucl. Instrum. Meth. A **276**, 557 (1989) 10.1016/0168-9002(89)90583-4.
- [101] K. Meierbachtol et al., Nucl. Instrum. Meth. A **788**, 59 (2015) 10.1016/j.nima.2015.02.032.
- [102] D. Doré et al., Nucl. Data Sheets **119**, 346 (2014) 10.1016/j.nds.2014.08.095.
- [103] J. Matarranz et al., Physics Procedia **47**, Scientific Workshop on Nuclear Fission Dynamics and the Emission of Prompt Neutrons and Gamma Rays, Biarritz, France, 28-30 November 2012, 76 (2013) 10.1016/j.phpro.2013.06.012.
- [104] A. Solders et al., Nuclear Data Sheets **119**, 338 (2014) 10.1016/j.nds.2014.08.093.
- [105] G. Lhersonneau et al., EPJ A **9**, 385 (2000) 10.1007/s100500070023.
- [106] J. Van Schelt et al., Phys. Rev. Lett. **111**, 061102 (2013) 10.1103/PhysRevLett.111.061102.
- [107] A. Al-Adili et al., EPJ A **51**, 59 (2015) 10.1140/epja/i2015-15059-2.
- [108] A. Al-Adili et al., (2014), arXiv:1409.0714 [nucl-ex].

- [109] D. Gorelov et al., Nucl. Instrum. Meth. B **376**, 46 (2016) 10.1016/j.nimb.2016.02.049.
- [110] G. W. McKinney et al., Proceedings of the MC2005 Conference, Chattanooga, Tennessee, April 17-21, 2005, LA-UR-04-8695 (2004).
- [111] P. Constantin et al., Nucl. Instrum. Meth. B **397**, 1 (2017) 10.1016/j.nimb.2017.02.032.
- [112] A. Carlson et al., Nucl. Data Sheets **110**, Special Issue on Nuclear Reaction Data, 3215 (2009) 10.1016/j.nds.2009.11.001.
- [113] A. Santamarina et al., *The JEFF-3.1.1 Nuclear Data Library*, tech. rep. 22 (Nuclear Energy Agency, 2009).
- [114] Theoretical High Energy Physics Group of the Radboud University Nijmegen, *NN-Online*, Accessed: 2017-08-14, <http://nn-online.org>.
- [115] M. Mendenhall and R. Weller, Nucl. Instrum. Meth. A **667**, 38 (2012) 10.1016/j.nima.2011.11.084.
- [116] W. Brandt and M. Kitagawa, Phys. Rev. B **25**, 5631 (1982) 10.1103/PhysRevB.25.5631.

Acta Universitatis Upsaliensis

Uppsala Dissertations from the Faculty of Science

Editor: The Dean of the Faculty of Science

1–11: 1970–1975

12. *Lars Thofelt*: Studies on leaf temperature recorded by direct measurement and by thermography. 1975.
13. *Monica Henricsson*: Nutritional studies on *Chara globularis* Thuill., *Chara zeylanica* Willd., and *Chara haitensis* Turpin. 1976.
14. *Göran Kloow*: Studies on Regenerated Cellulose by the Fluorescence Depolarization Technique. 1976.
15. *Carl-Magnus Backman*: A High Pressure Study of the Photolytic Decomposition of Azoethane and Propionyl Peroxide. 1976.
16. *Lennart Källströmer*: The significance of biotin and certain monosaccharides for the growth of *Aspergillus niger* on rhamnose medium at elevated temperature. 1977.
17. *Staffan Renlund*: Identification of Oxytocin and Vasopressin in the Bovine Adenohypophysis. 1978.
18. *Bengt Finnström*: Effects of pH, Ionic Strength and Light Intensity on the Flash Photolysis of L-tryptophan. 1978.
19. *Thomas C. Amur*: Diffusion in Dilute Solutions: An Experimental Study with Special Reference to the Effect of Size and Shape of Solute and Solvent Molecules. 1978.
20. *Lars Tegnér*: A Flash Photolysis Study of the Thermal Cis-Trans Isomerization of Some Aromatic Schiff Bases in Solution. 1979.
21. *Stig Tormod*: A High-Speed Stopped Flow Laser Light Scattering Apparatus and its Application in a Study of Conformational Changes in Bovine Serum Albumin. 1985.
22. *Björn Varnestig*: Coulomb Excitation of Rotational Nuclei. 1987.
23. *Frans Lettenström*: A study of nuclear effects in deep inelastic muon scattering. 1988.
24. *Göran Ericsson*: Production of Heavy Hypernuclei in Antiproton Annihilation. Study of their decay in the fission channel. 1988.
25. *Fang Peng*: The Geopotential: Modelling Techniques and Physical Implications with Case Studies in the South and East China Sea and Fennoscandia. 1989.
26. *Md. Anowar Hossain*: Seismic Refraction Studies in the Baltic Shield along the Fennolora Profile. 1989.
27. *Lars Erik Svensson*: Coulomb Excitation of Vibrational Nuclei. 1989.
28. *Bengt Carlsson*: Digital differentiating filters and model based fault detection. 1989.
29. *Alexander Edgar Kavka*: Coulomb Excitation. Analytical Methods and Experimental Results on even Selenium Nuclei. 1989.
30. *Christopher Juhlin*: Seismic Attenuation, Shear Wave Anisotropy and Some Aspects of Fracturing in the Crystalline Rock of the Siljan Ring Area, Central Sweden. 1990.

31. *Torbjörn Wigren*: Recursive Identification Based on the Nonlinear Wiener Model. 1990.
32. *Kjell Janson*: Experimental investigations of the proton and deuteron structure functions. 1991.
33. *Suzanne W. Harris*: Positive Muons in Crystalline and Amorphous Solids. 1991.
34. *Jan Blomgren*: Experimental Studies of Giant Resonances in Medium-Weight Spherical Nuclei. 1991.
35. *Jonas Lindgren*: Waveform Inversion of Seismic Reflection Data through Local Optimisation Methods. 1992.
36. *Liqi Fang*: Dynamic Light Scattering from Polymer Gels and Semidilute Solutions. 1992.
37. *Raymond Munier*: Segmentation, Fragmentation and Jostling of the Baltic Shield with Time. 1993.

Prior to January 1994, the series was called *Uppsala Dissertations from the Faculty of Science*.

Acta Universitatis Upsaliensis

Uppsala Dissertations from the Faculty of Science and Technology

Editor: The Dean of the Faculty of Science

- 1–14: 1994–1997. 15–21: 1998–1999. 22–35: 2000–2001. 36–51: 2002–2003.
52. *Erik Larsson*: Identification of Stochastic Continuous-time Systems. Algorithms, Irregular Sampling and Cramér-Rao Bounds. 2004.
53. *Per Åhgren*: On System Identification and Acoustic Echo Cancellation. 2004.
54. *Felix Wehrmann*: On Modelling Nonlinear Variation in Discrete Appearances of Objects. 2004.
55. *Peter S. Hammerstein*: Stochastic Resonance and Noise-Assisted Signal Transfer. On Coupling-Effects of Stochastic Resonators and Spectral Optimization of Fluctuations in Random Network Switches. 2004.
56. *Esteban Damián Avendaño Soto*: Electrochromism in Nickel-based Oxides. Coloration Mechanisms and Optimization of Sputter-deposited Thin Films. 2004.
57. *Jenny Öhman Persson*: The Obvious & The Essential. Interpreting Software Development & Organizational Change. 2004.
58. *Chariklia Rouki*: Experimental Studies of the Synthesis and the Survival Probability of Transactinides. 2004.
59. *Emad Abd-Elrady*: Nonlinear Approaches to Periodic Signal Modeling. 2005.
60. *Marcus Nilsson*: Regular Model Checking. 2005.
61. *Pritha Mahata*: Model Checking Parameterized Timed Systems. 2005.
62. *Anders Berglund*: Learning computer systems in a distributed project course: The what, why, how and where. 2005.
63. *Barbara Piechocinska*: Physics from Wholeness. Dynamical Totality as a Conceptual Foundation for Physical Theories. 2005.
64. *Pär Samuelsson*: Control of Nitrogen Removal in Activated Sludge Processes. 2005.

65. *Mats Ekman*: Modeling and Control of Bilinear Systems. Application to the Activated Sludge Process. 2005.
66. *Milena Ivanova*: Scalable Scientific Stream Query Processing. 2005.
67. *Zoran Radovic*: Software Techniques for Distributed Shared Memory. 2005.
68. *Richard Abrahamsson*: Estimation Problems in Array Signal Processing, System Identification, and Radar Imagery. 2006.
69. *Fredrik Robelius*: Giant Oil Fields – The Highway to Oil. Giant Oil Fields and their Importance for Future Oil Production. 2007.
70. *Anna Davour*: Search for low mass WIMPs with the AMANDA neutrino telescope. 2007.
71. *Magnus Ågren*: Set Constraints for Local Search. 2007.
72. *Ahmed Rezine*: Parameterized Systems: Generalizing and Simplifying Automatic Verification. 2008.
73. *Linda Brus*: Nonlinear Identification and Control with Solar Energy Applications. 2008.
74. *Peter Nauchlér*: Estimation and Control of Resonant Systems with Stochastic Disturbances. 2008.
75. *Johan Petrini*: Querying RDF Schema Views of Relational Databases. 2008.
76. *Noomene Ben Henda*: Infinite-state Stochastic and Parameterized Systems. 2008.
77. *Samson Keleta*: Double Pion Production in $dd \rightarrow \alpha\pi\pi$ Reaction. 2008.
78. *Mei Hong*: Analysis of Some Methods for Identifying Dynamic Errors-invariables Systems. 2008.
79. *Robin Strand*: Distance Functions and Image Processing on Point-Lattices With Focus on the 3D Face-and Body-centered Cubic Grids. 2008.
80. *Ruslan Fomkin*: Optimization and Execution of Complex Scientific Queries. 2009.
81. *John Airey*: Science, Language and Literacy. Case Studies of Learning in Swedish University Physics. 2009.
82. *Arvid Pohl*: Search for Subrelativistic Particles with the AMANDA Neutrino Telescope. 2009.
83. *Anna Danielsson*: Doing Physics – Doing Gender. An Exploration of Physics Students' Identity Constitution in the Context of Laboratory Work. 2009.
84. *Karin Schöning*: Meson Production in pd Collisions. 2009.
85. *Henrik Petrén*: η Meson Production in Proton-Proton Collisions at Excess Energies of 40 and 72 MeV. 2009.
86. *Jan Henry Nyström*: Analysing Fault Tolerance for ERLANG Applications. 2009.
87. *John Håkansson*: Design and Verification of Component Based Real-Time Systems. 2009.
88. *Sophie Grape*: Studies of PWO Crystals and Simulations of the $\bar{p}p \rightarrow \bar{\Lambda}\Lambda, \bar{\Lambda}\Sigma^0$ Reactions for the PANDA Experiment. 2009.
90. *Agnes Rensfelt*: Viscoelastic Materials. Identification and Experiment Design. 2010.
91. *Erik Gudmundson*: Signal Processing for Spectroscopic Applications. 2010.
92. *Björn Halvarsson*: Interaction Analysis in Multivariable Control Systems. Applications to Bioreactors for Nitrogen Removal. 2010.
93. *Jesper Bengtson*: Formalising process calculi. 2010.
94. *Magnus Johansson*: Psi-calculi: a Framework for Mobile Process Calculi. Cook your own correct process calculus – just add data and logic. 2010.
95. *Karin Rathsman*: Modeling of Electron Cooling. Theory, Data and Applications. 2010.

96. *Liselott Dominicus van den Bussche*. Getting the Picture of University Physics. 2010.
97. *Olle Engdegård*. A Search for Dark Matter in the Sun with AMANDA and IceCube. 2011.
98. *Matthias Hudl*. Magnetic materials with tunable thermal, electrical, and dynamic properties. An experimental study of magnetocaloric, multiferroic, and spin-glass materials. 2012.
99. *Marcio Costa*. First-principles Studies of Local Structure Effects in Magnetic Materials. 2012.
100. *Patrik Adlarson*. Studies of the Decay $\eta \rightarrow \pi^+ \pi^- \pi^0$ with WASA-at-COSY. 2012.
101. *Erik Thomé*. Multi-Strange and Charmed Antihyperon-Hyperon Physics for PANDA. 2012.
102. *Anette Löfström*. Implementing a Vision. Studying Leaders' Strategic Use of an Intranet while Exploring Ethnography within HCI. 2014.
103. *Martin Stigge*. Real-Time Workload Models: Expressiveness vs. Analysis Efficiency. 2014.
104. *Linda Åmand*. Ammonium Feedback Control in Wastewater Treatment Plants. 2014.
105. *Mikael Laaksoharju*. Designing for Autonomy. 2014.
106. *Soma Tayamon*. Nonlinear System Identification and Control Applied to Selective Catalytic Reduction Systems. 2014.
107. *Adrian Bahne*. Multichannel Audio Signal Processing. Room Correction and Sound Perception. 2014.
108. *Mojtaba Soltanian*. Signal Design for Active Sensing and Communications. 2014.
109. *Håkan Selg*. Researching the Use of the Internet — A Beginner's Guide. 2014.
110. *Andrzej Pysznik*. Development and Applications of Tracking of Pellet Streams. 2014.
111. *Olov Rosén*. Parallel Stochastic Estimation on Multicore Platforms. 2015.
112. *Yajun Wei*. Ferromagnetic Resonance as a Probe of Magnetization Dynamics. A Study of FeCo Thin Films and Trilayers. 2015.
113. *Marcus Björk*. Contributions to Signal Processing for MRI. 2015.
114. *Alexander Madsen*. Hunting the Charged Higgs Boson with Lepton Signatures in the ATLAS Experiment. 2015.
115. *Daniel Jansson*. Identification Techniques for Mathematical Modeling of the Human Smooth Pursuit System. 2015.
116. *Henric Taavola*. Dark Matter in the Galactic Halo. A Search Using Neutrino Induced Cascades in the DeepCore Extension of IceCube. 2015.
117. *Rickard Ström*. Exploring the Universe Using Neutrinos. A Search for Point Sources in the Southern Hemisphere Using the IceCube Neutrino Observatory. 2015.
118. *Li Caldeira Balkeståhl*. Measurement of the Dalitz Plot Distribution for $\eta \rightarrow \pi^+ \pi^- \pi^0$ with KLOE. 2015.
119. *Johannes Nygren*. Input-Output Stability Analysis of Networked Control Systems. 2016.
120. *Joseph Scott*. Other Things Besides Number. Abstraction, Constraint Propagation, and String Variable Types. 2016.
121. *Andrej Andrejev*. Semantic Web Queries over Scientific Data. 2016.

122. *Johan Blom*. Model-Based Protocol Testing in an ERLANG Environment. 2016.
123. *Liang Dai*. Identification using Convexification and Recursion. 2016.
124. *Adriaan Larmuseau*. Protecting Functional Programs From Low-Level Attackers. 2016.
125. *Lena Heijenskjöld*. Hadronic Decays of the ω Meson. 2016.
126. *Delphine Misao Lebrun*. Photonic crystals and photocatalysis. Study of titania inverse opals. 2016.
127. *Per Mattsson*. Modeling and identification of nonlinear and impulsive systems. 2016.
128. *Lars Melander*. Integrating Visual Data Flow Programming with Data Stream Management. 2016.
129. *Kristofer Severinsson*. Samarbete = Samverkan? En fallstudie av AIMday vid Uppsala universitet. 2016.
130. *Nina Fowler*. Walking the Plank of the Entrepreneurial University. The little spin-out that could? 2017.
131. *Kaj Jansson*. Measurements of Neutron-induced Nuclear Reactions for More Precise Standard Cross Sections and Correlated Fission Properties. 2017.

